Proposal for experiments at SIS18 during FAIR Phase-0

The HADES Collaboration

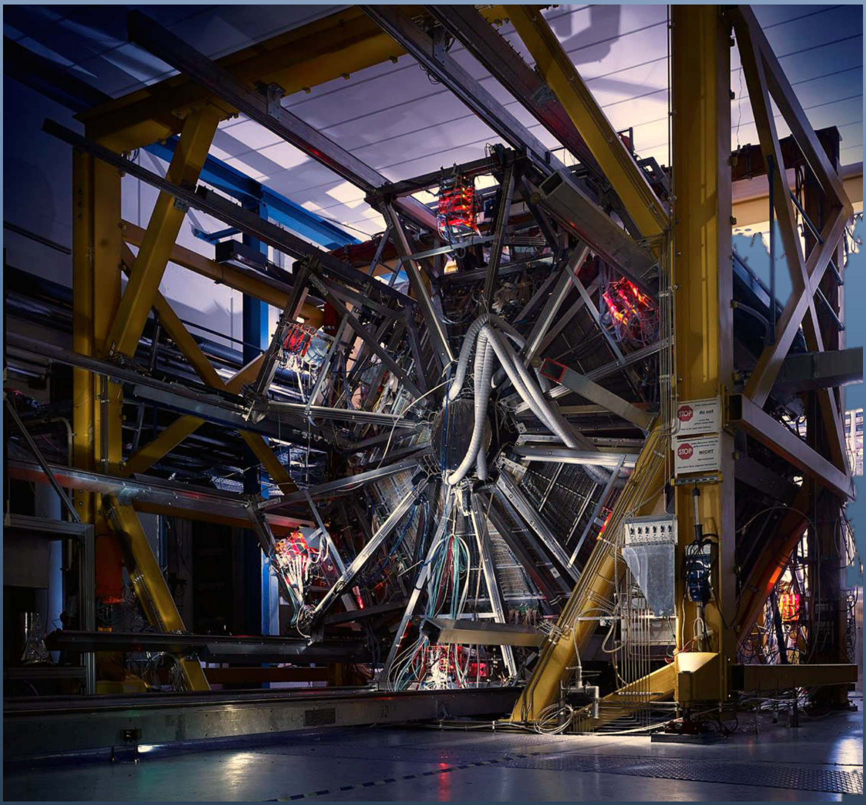

Properties of hadron resonances and baryon rich matter

Proposal for experiments at SIS18 during FAIR Phase-0

as of June 15, 2017

Executive summary

HADES is operated with beams from SIS18 and investigates the microscopic properties of resonance matter formed in heavy-ion collision in the 1–2 A GeV energy regime. Important topics of the research program are the mechanisms of strangeness production, the emissivity of resonance matter and the role of baryonic resonances herein. The latter topic is also addressed through investigations of exclusive channels in proton and pion beam induced reactions, both for hadronic and semi-leptonic final states. **Major achievements** of the HADES research **are summarized in Chapter 1**.

Chapter 2 describes the status of the spectrometer with emphasis on the new detector systems which will be available for experiments during FAIR Phase-0. HADES is prepared to perform experiments addressing both nuclear/quark matter and hadron physics aspects. The upgrade of the RICH UV detector is based on instrumentation developed for the CBM experiment that will intermediately be operated in the HADES RICH as CBM FAIR Phase-0 activity. Likewise, the forward tracker is based on PANDA technology and is hence also a FAIR Phase-0 activity of the PANDA collaboration.

In Chapter 3 we present the strategy of our physics program for the entire FAIR Phase-0 *based on new, full-scale Monte-Carlo simulations* using the new upgraded setup. We have chosen to do so to give the reader the chance to appreciate our proposal in the context of the HADES research program, which will naturally connect to the upcoming experiment programs addressed by CBM and PANDA. We will also present a short outlook on the role of HADES as a complementary experimental setup for addressing physics outlined in the CBM physics book.

The experiment proposals for the period 2018–2019 **are presented in Chapter 4**. We stay brief in this chapter and refer to the more detailed information presented elsewhere in this document. Yet, we aim at providing all information necessary to fully understand the scope of the proposal and motivate, in particular, the beam time request. We have chosen two experimental runs such that there is more flexibility in scheduling the beam time. The *pion proposal* needs maximum intensity primary beam in SIS18 and high level performance of the accelerator, while the *ion proposal* has more relaxed requirements and would qualify also for periods of limited performance of the accelerator complex.

Contents

Chapter 1

Recent HADES results

Contents

1.1 Properties and structure of resonance matter

QCD describes nucleons as colorless states of three nearly massless quarks confined to a small volume due to the strong force. The coupling of the quarks to the non-trivial QCD vacuum leads to a depletion of the vacuum action in the center and the formation of a meson cloud surrounding this cavity. Strongly interacting matter at moderate temperatures and densities can be described using Chiral Perturbation Theory (CPT) and assuming an ensemble of nucleon cores embedded in a cloud of virtual pions. Short range interactions are encoded in contact interactions of the nucleon cores and the depletion of the chiral condensate is expected to reach more than 50% at two times ρ_0 and a temperature of 50 MeV [1].

In a collision of heavy ions at energies around $1\,A$ GeV, strongly interacting matter is substantially compressed and collective kinetic energy is dissipated into intrinsic degrees of freedom. As a result, nucleons are excited to baryonic resonances and in the final state of the reaction mesonic states are observed with increasing abundances as the center-of-mass energy of the collision rises. A scientific challenge is to understand the microscopic properties of the matter formed in such collisions. It is conjectured that hadron properties are substantially modified, ultimately the states losing their hadronic character and forming exotic phases of strongly interacting matter.

Figure 1.1 [2] shows a calculation of the expectation value of the chiral condensate (orange gradient) for QCD matter in a diagram of temperature vs. baryochemical potential (μ_B) using a Polyakov-Quark-Meson Model [3]. It is presented together with so-called freeze-out points determined from particle abundances measured in heavy-ion collisions with the help of statistical hadronization models (SHM) and extracted from various experiments. They reach temperatures around 160 MeV at vanishing μ_B (LHC- and top RHIC energies) and extend down to around 50 MeV at high μ_B for collision systems at SIS18 energies. As the chiral condensate seems to drop rapidly beyond these freeze-out points, it is assumed

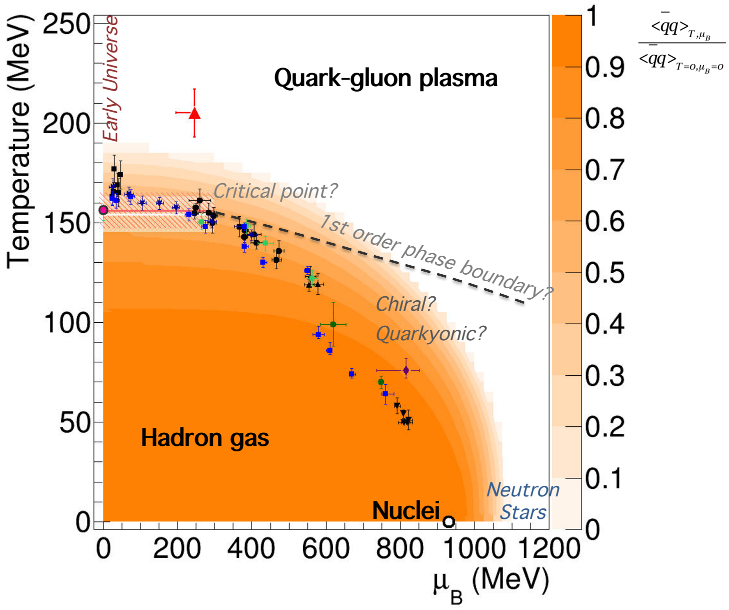

Figure 1.1: Sketch of the phase diagram of QCD matter [2] including freeze-out data points in T and μ_B describing the final state hadron abundances in a statistical hadronization model (blue squares and pink circle from [4, 5], light green squares from [6], black solid symbols from [7], dark blue stars from [8], green circles [9], lila diamond [10], as well as Lattice QCD results from [11] (white curve) and [12] (red curve)). The red triangle is extracted from the measured invariant-mass slope of dimuons in the mass range $1.2 < M_{\mu\mu} < 2\ \text{GeV}/c^2$ in the dimuon measurement in In+In collisions at $\sqrt{s_{NN}} = 17.2$ GeV [13]. The expectation value of the chiral condensate relative to the vacuum is depicted as shaded orange region [3].

that the nuclear fireball spends most of its time in a phase with a substantially reduced chiral condensate.

As a matter of fact, the direct observation of strong medium modifications is demanding. HADES pursues a strategy which relies on systematic measurements of strangeness production and electron pair (e^+e^-) emission. Hadrons carrying strangeness are specifically interesting as their production threshold is mostly below the energy available in a single (free) N+N collision at SIS18 beam energies. Rather, their production requires a certain degree of collectivity like multi-particle (or -step) processes or deep off-shell production. Electron pair emission, on the other hand, is a penetrating probe and is very sensitive to the in-medium ρ spectral function [14]. Experiments with heavy ions are complemented with measurements of meson production off nuclei and in elementary collisions using proton and pion beams. The latter are crucial to establish significant reference spectra in comparison to which true medium effects can be demonstrated. Furthermore, they provide an important insight into the role played by the baryon resonances in meson production and allow for first direct studies of their dielectron decays. The latter are also important for the understanding of Vector Meson Dominance in baryonic sector. This ansatz plays a prominent role in the calculations of the in-medium spectral function and needs experimental verification.

Among the most important results obtained by HADES in its first measurement campaign (2002 – 2008) are:

- Excess radiation of virtual photons in the invariant-mass range from 0.2 to 0.7 GeV/c^2 for the collision system Ar+KCl at 1.76 A GeV. This radiation can be understood as being due to a regeneration of baryonic resonances in the fireball [15].
- Observation of virtual photon radiation off the internal charged pion line in n+p collisions below the η meson production threshold. This process explains the strong difference in virtual photon production between p+p and n+p reactions and its observation solved the long-standing DLS puzzle [16, 17, 18].
- The first measurement of Δ Dalitz decay branching ratio and its dependence on the dielectron invariant mass in the exclusive process $pp \to ppe^+e^-$ [18].
- Indication of a nearly complete disappearance of the omega signal (and appearance of a dielectron excess relative to the p+p reference [19] below the vector meson pole) in proton-induced reactions on Nb for virtual photon momenta below 0.8 GeV/c [20].
- Searching for a narrow resonance in dielectron spectra measured in the reactions p+p and p+Nb at 3.5 GeV, as well as Ar+KCl at 1.76 A GeV we have established an upper limit at 90% CL on the mixing $\varepsilon^2 = \alpha^{'}/\alpha$ of a hypothetical dark photon U in the mass range $\mathrm{M}_U = 0.02 - 0.6$ GeV/c^2 [21].
- Measurement of the spectral shape of the $\Lambda(1405)$ resonance from p+p collisions at 3.5 GeV and indication of a shift of its pole mass of 20 MeV/c^2 with respect to the listed pole mass. This effect is interpreted as the indication of the molecular nature of the $\Lambda(1405)$ composed of a baryon-meson system [22, 23].
- Evidence of the repulsive interaction of K^0_S within cold nuclear matter measured in proton-induced reactions and extracted from the comparison of the meson spectra with models precisely calibrated to p+p reactions [24].
- ϕ meson production, which is compatible with the SHM assumption [25, 26], as source of K^-.
- Unexpectedly large yields above SHM expectation for Ξ^- in Ar+KCl (1.76 A GeV) and p+Nb (3.5 GeV) reactions [27, 28].

All of the observations in heavy-ion collisions are in accordance with a picture describing the fireball as a resonance gas with strong in-medium effects. The observed hadron multiplicities resemble thermalization although the flow pattern of *e.g.* protons does not. To further scrutinize these observations, HADES focuses next on a heavy collision system at maximum SIS18 energy and on reactions with hadronic beams (pions and protons) on proton and nuclear targets.

1.1.1 Emissivity of matter

It has been established that baryon-driven medium effects influence significantly the ρ meson in-medium spectral function and are considered key for the description of low-mass dilepton spectra measured at SPS [13, 29], at top RHIC [30, 31], and RHIC Beam Energy Scan energies [32, 33]. The successful ρ mass broadening scenario implies a strong coupling of the ρ meson to baryons [14, 34, 35, 36, 37]. Quantitative descriptions of heavy-ion collisions at bombarding energies of a few GeV per nucleon indicate that, due to the nucleon stopping,

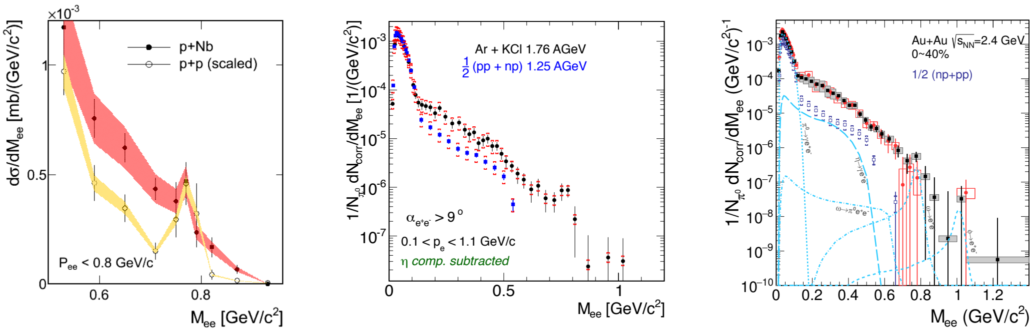

Figure 1.2: HADES di-electron spectra. Left: Comparison of the invariant mass distribution of e^+e^-– pairs with $p_{ee} < 0.8$ GeV/c in p+p (open circles) and p+Nb (full circles) collisions at the same kinetic beam energy of 3.5 GeV. Middle: Comparison of the reference spectrum from properly scaled N+N collisions with the reconstructed e^+e^- mass distribution in Ar+KCl (the expected contribution from the η-Dalitz decay has been subtracted). Right: Invariant mass distribution of electron pairs (e^+e^-) emitted in the 40% most central Au+Au collisions. Black and red squares refer to *Backtracking* (BT) and *Ring Finding* (RF) strategy for dielectron reconstruction, respectively. The blue squares show the reference spectrum measured in elementary N+N collisions. The dashed curves represent contributions originating from long-lived mesons, *i.e.* π^0, η, ω and ϕ.

the dominant medium radiation is presumably driven by baryonic excitations (resonances) in the system and therefore baryon-driven medium effects are expected to be maximal.

A strong momentum dependence of the ρ meson spectral function already at normal nuclear matter density $\rho = \rho_0$ has been predicted [38, 39]. For the first time dielectrons in the relevant momentum range $p_{ee} < 0.8$ GeV/c have been measured by HADES in p+Nb reactions at a kinetic beam energy of 3.5 GeV [20]. The p+p reactions at the same beam energy have been measured and serve as a necessary reference for the study of in-medium modifications of vector mesons [19, 40]. Fig. 1.2 (left panel) shows an excess yield of electron pairs with momenta $p_{ee} < 0.8$ GeV/c below the omega pole mass when comparing the spectral distribution of the e^+e^- invariant masses reconstructed in p+Nb collisions to pairs produced in elementary p+p reactions. Complementary to the results obtained by the NA60 collaboration [41], HADES sees rather a melting than a shift of the ρ meson. These trends hint at strong coupling of the ρ meson to baryonic resonances and absorption of the ω meson, both being manifestations of in-medium modifications of vector mesons.

An important prerequisite to identify true in-medium radiation of dense matter is the detailed knowledge of the complex superposition of baryonic and long-living mesonic contributions to the rate at various stages of the collision. In this context, we compare e^+e^- production rates measured in C+C, Ar+KCl and Au+Au collisions with the properly scaled production rates from N+N collisions. A reference spectrum has been generated by computing the isospin-averaged emission probability per produced neutral pion from separately measured p+p and quasi-free n+p collisions [16]. A radiation component beyond that of binary nucleon collisions is not yet observed in this light collision system, like C+C. In contrast, a direct comparison of the N+N reference spectrum with the invariant-mass distribution measured in Ar+KCl collisions at 1.76 A GeV and in Au+Au collisions at 1.23 A GeV shows a pronounced radiation excess between the π^0 Dalitz and the vector meson regions [15] (see Fig. 1.2, middle and right panels).

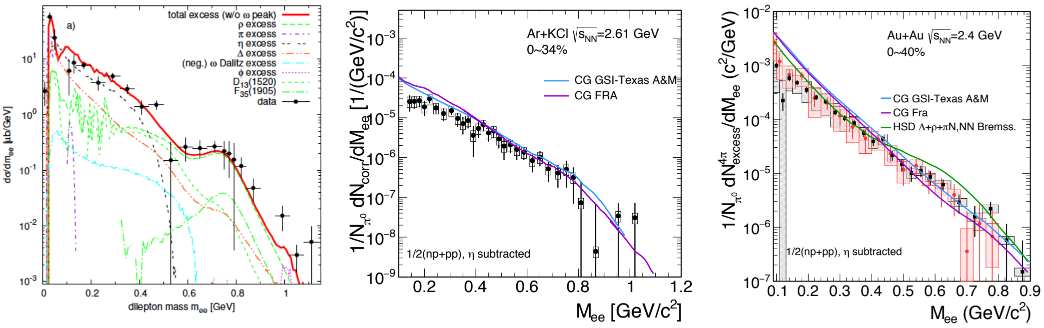

Figure 1.3: Left: Excess e^+e^- yield measured in p+Nb 3.5 GeV ($p_{ee} < 0.8$ GeV/c) compared to GiBUU transport model calculations [42]. Middle: Dilepton excess radiation observed in the 34% most central Ar+KCl collisions. Contributions from first chance N+N collisions and late η-Dalitz decays have been subtracted from the data. The yield is normalized to the number of produced π^0 (to remove trivial $\langle A_{part} \rangle$ dependences). The blue [43] and pink [44] curves show the results of two versions of coarse grained UrQMD calculations using different concepts for obtaining the thermal parameters. Right: same for Au+Au collisions at 1.23 A GeV. The green curve represents HSD transport model calculations [45].

In order to better quantify the excess radiation, we first subtract the cocktail of contributions from long-lived sources that have been obtained in the following way: (i) π^0 and η meson multiplicities have been taken from a measurement discussed in [46, 47]; (ii) the ω yield has been fixed such as to get, after subtraction, a smooth underlying continuum; the ρ contribution is not subtracted. The dilepton excess radiation resulting from this analysis procedure is presented in Fig. 1.3. The spectrum drops off nearly exponentially beyond e^+e^- due to the π^0-Dalitz decays and supports the assumption that the emission stems from a thermalized system. The long-lived vector mesons ω and ϕ are not visible above the continuum radiation. This thermal dielectron radiation enables us to access the fireball lifetime through the dilepton yield and the temperatures of the fireball through the slope of the invariant-mass spectrum in the low invariant-mass window M_{ee} = 0.3 - 0.7 GeV/c^2 [33, 48, 49].

In Ref. [50], a combined analysis of finite-temperature QCD [51] and Weinberg [52] sum rules has been carried out to test the in-medium ρ spectral function [53] that describes dilepton spectra with respect to chiral symmetry restoration. A microscopic investigation of the in-medium $\rho - a_1$ system has recently been conducted within the Massive-Yang Mills framework [54]. The extension of this analysis to finite baryon densities remains a formidable task and experimental data are of great importance to validate the model calculations. In order to access experimentally the $\rho - a_1$ chiral mixing one has to monitor the behaviour of e^+e^- spectra beyond M_{ee} of 1 GeV/c^2 in elementary and heavy-ion collisions. Up to now, due to the limited statistics, accessing this mass range with HADES was not possible. Future HADES campaigns will allow to perform this unique measurement.

1.1.2 Strangeness production and propagation

Various aspects of strangeness production at SIS energies have been investigated by the FOPI and KaoS experiments and recently also by HADES. In contrast to strange particle production in elementary N+N collisions, in heavy-ion reactions additional multi-step

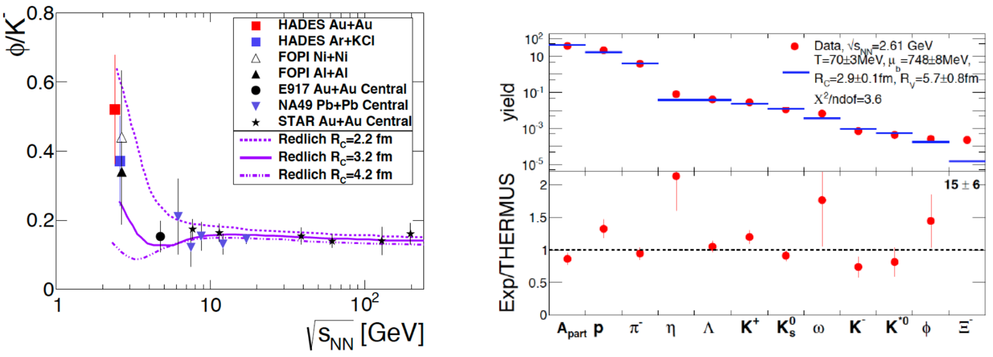

Figure 1.4: Left: The ϕ/K^- ratio shows a flat trend at high energies and a sharp rise towards lower energies, which can be explained within the statistical model framework using a proper strangeness correlation radius R_c (for details see [26]). Right: Yields (filled red circles) of hadrons in Ar+KCl reactions at 1.76 A GeV and the corresponding THERMUS fit values (blue bars). The lower plot shows the ratio of the experimental value and the THERMUS value. For the Ξ^- the value of the ratio is quoted instead of being displayed as a point.

processes as well as strangeness-exchange reactions like $\pi\Lambda \rightarrow NK^-$ do occur. Hence any detailed understanding of strangeness production and propagation in heavy-ion reactions requires information on all production channels of all particles with open or hidden strangeness.

Only recent data from HADES come close to fulfill this requirement for heavy collision systems like Au+Au. For the first time, a nearly complete set of strange hadrons (ϕ, K^+, K^-, K^0_s) has been reconstructed at such low beam energies ($\sqrt{s_{NN}} = 2.4$ GeV). A striking result shown in the left panel of the Fig. 1.4 is the large ϕ meson abundance which accounts for about 25% of the total K^- production [26]. The previously observed difference in slope of K^+ and K^- transverse spectra disappears if the K^- spectra are corrected for the ϕ decay contribution. As a consequence, the common interpretation of the differences in slopes as a sign for sequential freeze-out of charged kaons is obsolete. This example nicely underlines the importance of measuring an (almost) complete set of hadron yields carrying strangeness before concluding about the propagation of strangeness inside the medium.

The reconstruction of the Ξ^- hyperon in Ar+KCl reactions at 1.76 A GeV [27] marks one of the highlights in relativistic heavy-ion physics in the recent years as the yield shows an strong enhancement over statistical model calculations [55] (see Fig. 1.4, right panel). In case of the collected Ar+KCl data sample at 1.76 A GeV, one may calculate the probability for the production of two $s\bar{s}$ pairs in one collision. Assuming that both pairs are independently created, their production probability $P_{2s\bar{s}}$ is given as the square of the single-pair production probability $P_{s\bar{s}}$. Keeping associated production in mind, $P_{s\bar{s}}$ can be estimated as the combined multiplicity of all particles that carry a strange quark, respectively the combined multiplicity of all anti-strange particles, *i.e.* $K^+ + K^0 + \phi$, yielding $P_{s\bar{s}} \simeq 0.05$ and hence $P_{2s\bar{s}} \simeq 0.0025$. Considering that the observed Ξ^- yield is in fact an order of magnitude smaller, we conclude that in 10% of these events both s quarks end up together in a Ξ^-, which is well above expectations from statistical models.

Recent data of HADES revealed that the excess of the Ξ^- over several state-of-the-art models shows up also in p+Nb reactions at $\sqrt{s_{NN}}= 3.2$ GeV [28]. The extracted experimental signal in the invariant-mass spectrum is displayed on the left side of Fig. 1.5.

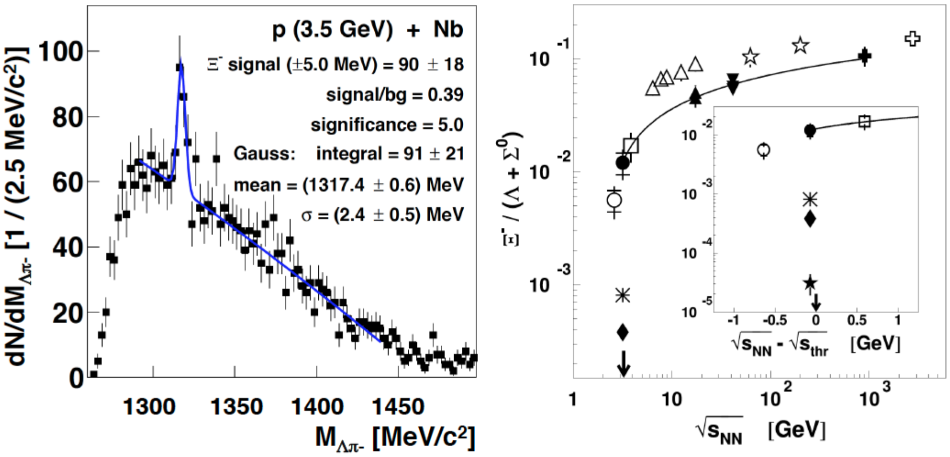

Figure 1.5: Left: Invariant mass spectrum of Λ hyperons and negative pions obtained in p+Nb collisions at $\sqrt{s_{NN}}$= 3.2 GeV. A clear peak corresponding to the Ξ^- signal is visible. Right: Excitation function of the Ξ^-/Λ ratio for various colliding systems. The open symbols correspond to heavy-ion data, the filled symbols represent data from p+A collisions. The black line corresponds to a simple parameterization fitted to the p+A data, see text for details. The inset shows a zoom to the area of the HADES p+Nb data point and the comparison with three different models. The upper star symbol corresponds to the yield obtained from a THERMUS (v2.3) fit to p+Nb data. The lower star symbol corresponds to the yield obtained via the UrQMD (v3.4) transport code and the intermediate point to a GiBUU transport calculation.

In addition, the energy excitation function of the Ξ^-/Λ ratio for various colliding systems is displayed on the right side of Fig. 1.5. While the open symbols correspond to heavy-ion data, the filled symbols represent proton induced collisions on nuclei. The black line corresponds to a simple parameterization fitted to the proton induced data of the form

$$F(\sqrt{s_{NN}}) = C \times \left(1 - \left[\frac{D}{\sqrt{s_{NN}}}\right]^G\right)^H . \qquad (1.1)$$

The inset shows a zoom to the area of the HADES p+Nb data point and the comparison to three different models. The upper star symbol corresponds to the yield obtained from a THERMUS (v2.3) fit to p+Nb data similar to the one discussed in this work. While the lower star symbol corresponds to the yield obtained via the UrQMD (v3.4) transport code, the intermediate point results from a GiBUU transport calculation.

A possible explanation of this observation, suggesting production from high mass (>2 GeV/c^2) baryonic resonances with significant branching ratios for the Ξ^- decay, has been proposed in [56]. However, to finally conclude on the existence of such decays, dedicated measurements with p+p or π^-+p experiments are required.

1.1.3 Thermal particle production

In the last 30 years statistical hadronization models have been established as a successful tool to fit particle yields or yield ratios from relativistic and ultra-relativistic heavy-ion collisions with only a few parameters [57, 58, 59]. The extracted freeze-out parameters show a striking regularity, lining up on a curve in the temperature-baryochemical potential plane that connects smoothly data from the GeV to the TeV regime [7]. These findings have been widely interpreted as a hint that (local) chemical equilibrium is achieved in such collisions.

When fitting the hadron yields reconstructed from Ar+KCl collisions with the THERMUS code [60] (see Fig. 1.4, right panel), we find the following values for the chemical freeze-out parameters $T_{chem} = (70 \pm 3)$ MeV, $\mu_b = (748 \pm 8)$ MeV, the strangeness correlation radius results as $R_c = (2.9 \pm 0.1)$ fm and the radius of the fireball $R = (5.7 \pm 0.8)$ fm with a χ^2/d.o.f.[1] of 3.6 [9]. A detailed comparison of the data with the statistical model fit is shown in the upper part of Fig. 1.4 (right panel), while the lower part depicts the ratio of data to the THERMUS value. The extracted temperatures and baryochemical potentials (Fig. 1.1, green circles) are found to be in agreement with the universal freeze-out curve. An understanding of the apparent equilibration in phase space calls for further investigations.

1.1.4 Correlations and fluctuations

The strong rise towards lower collision energies of the fourth moment of the event-by-event (e-by-e) net-baryon multiplicity distribution observed by the STAR collaboration [61] has recently attracted a lot of attention. In view of theoretical studies of critical phenomena in the QCD matter phase diagram, this finding could signal the existence of a critical end point. To further scrutinize this interpretation, an extension of the respective excitation function to even lower collision energies is of importance. We have therefore started to investigate fluctuation observables using the data from our high-statistics measurement of Au+Au collisions at 1.23 A GeV. Making use of a realistic GEANT3-based detector response simulation we have studied in detail various systematic effects that influence the higher moments of the reconstructed proton distributions in HADES. In particular, corrections for the finite acceptance, as well as for the detection and reconstruction efficiencies – including e-by-e changes of the latter – have been investigated with simulations and data. Hereby the approaches proposed by Koch and co-authors [62, 63, 64] have been validated. Furthermore, the effects of volume fluctuations [65, 66, 67] due to the finite resolution of our centrality selections, based on the HADES Forward Wall charge sum, has been studied. At SIS18 beam energies the fraction of protons bound in light fragments (d, t, He) is large and the question to what extent these influence the role of protons as proxy for baryon number fluctuations remains to be clarified. We have already begun to investigate the contribution of the – next to the protons – dominant deuterons to the fluctuation signal.

Flow observables play a very important role in field of heavy-ion physics, since they allow to gather information on the equation-of-state (EOS) of dense nuclear matter and also provide a means to extract medium properties such as the ratio of shear viscosity and entropy density η/s. Figure 1.6 shows a summary of η/s values extracted from existing measurements and model calculations. While η/s is around the theoretical lower boundary at high energies (RHIC and LHC) a strong rise towards lower energies is expected. However, current analyses do not yet result in a consistent picture and more precise data, especially on higher-order flow coefficients, in the HADES energy region (indicated by the gray band) will help to narrow down the properties of the hadronic medium produced here.

With the high statistics of seven billion Au+Au collisions at 1.23 A GeV recorded in 2012 the investigation of higher-order flow harmonics is now possible and under current investigation. Multi-particle azimuthal correlation techniques can in addition be utilized to

---

[1] Defined as the number of particle yields included in the fit minus the number of free parameters.

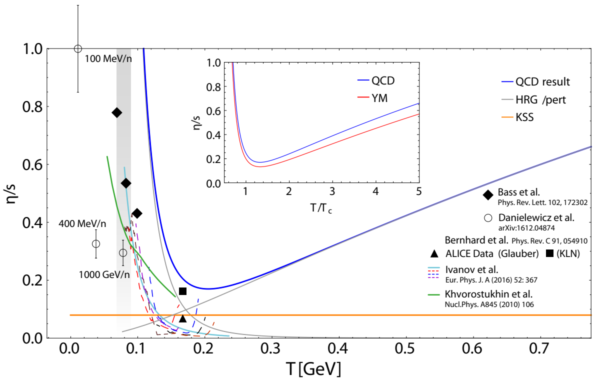

Figure 1.6: The ratio of shear viscosity and entropy density η/s as a function of the freeze-out temperature T, compiled from several model calculations and data analyses. The gray band indicates the region to which HADES measurements will contribute.

disentangle the contribution from collective and non-flow processes involved in the dynamical evolution of heavy-ion reactions. At low energies v_1 and v_2, related to directed and elliptic flow, have been measured for pions, charged kaons, protons, neutrons and fragments at the BEVALAC and SIS18, but so far higher-order harmonics have not been studied.

Figure 1.7 summarizes preliminary results on directed (v_1) and elliptic (v_2) flow of protons, extracted over a large region of phase space using the standard event plane method [68]. The data have been corrected for the event plane resolution [69, 70]. In addition, an efficiency correction due to the differential detector occupancy has been applied track-by-track as a function of the polar angle, the relative angle to the event plane and the track multiplicity in a given sector. A good forward backward symmetry is seen with respect to mid-rapidity, as expected due to the symmetry of the collisions system. Remaining

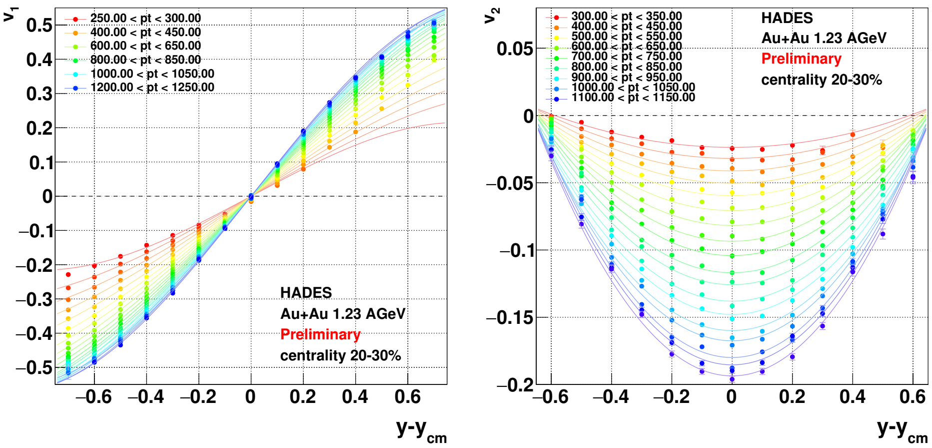

Figure 1.7: Preliminary data on directed flow (v_1, left panel) and elliptic flow (v_2, right panel) of protons measured by HADES in semi-central ($20-30$ %) Au+Au collisions at 1.23 A GeV [68]. The data are presented as a function of the center-of-mass rapidity in transverse momentum intervals of 50 MeV/c (lines are to guide the eye).

discrepancies are well within the systematic error, which has been estimated by embedding simulated protons in to real and UrQMD background events. The precision of the v_1 and v_2 data demonstrated that also the measurement of higher-order flow harmonics is feasible in this low energy regime. This will allow to extend the existing data into so far unexplored regions and will provide new insights into the properties of strongly interacting matter at extreme densities, as *e.g.* its viscosity and provide thus an important reference to measurements at higher energies.

1.2 Establishing reference spectra and resonance properties

Studying reactions with proton and pion beams on proton (LH_2) target is an important element of the HADES program. Besides measurements of production cross sections, which provide essential reference for heavy-ion collisions, also the elementary reaction mechanism was studied. In particular the role of baryonic resonances was investigated in both strangeness and dielectron production. In the latter case, an important milestone was the understanding of the elementary processes of baryon radiative Dalitz decays and nucleon-nucleon bremsstrahlung.

1.2.1 Nucleon-nucleon interactions

At SIS18 energies baryonic sources play an important role in dielectron production. The most prominent example is the $\Delta(1232)$ which is the dominant source of dielectron pairs below the η meson production threshold ($E_{beam} = 1.27$ GeV). It contributes both via the decay into $\pi^0 N \to e^+e^-\gamma N$ and via the direct $\Delta(1232) \to Ne^+e^-$ Dalitz-decay. These contributions describe the inclusive data in p+p reactions, but are not sufficient to explain the dielectron yield measured in n+p collisions at the same kinetic beam energy, even when the non-resonant nucleon-nucleon bremsstrahlung is coherently added [16]. Two explanations were proposed to account for this effect, both related to the charged pion exchange contribution, which does not contribute in the case of the exclusive $pp \to ppe^+e^-$ reaction: (i) emission from the internal meson exchange line including the respective electromagnetic pion form factor [71] (ii) final state interaction of two Δ isobars $\Delta\Delta \to \rho NN \to e^+e^-NN$ excited on the two nucleon lines [72].

To verify these two scenarios and to study the $\Delta(1232) \to Ne^+e^-$ decay in detail, HADES has performed a comprehensive analysis of the exclusive ppe^+e^- and npe^+e^- final states [17, 18]. The branching ratio of the $\Delta(1232) \to Ne^+e^-$ decay branching ratio $BR = 4.19 \pm 0.62(syst.) \pm 0.34(stat.) \cdot 10^{-5}$ has been extracted for the first time from the p+p data. Furthermore, for the first time it has been demonstrated that the differential decay rate analyzed in function of the invariant mass shows sensitivity to the magnetic electromagnetic transition form factor (etFF) (G_M). A slight increase of the measured rate to the one expected for a point-like Δ towards higher invariant masses has been obtained (see Fig. 1.8, left panel). Such behavior was predicted by the covariant quark spectator models of Iachello [73, 74, 75] (black dashed curve) and Ramahlo-Peña [76] (blue curve). It can be interpreted as an effect of a pion cloud which surrounds the hadron core and is probed by a virtual photon at relatively small q^2 (see red dashed line).

Fig. 1.8 (right panel) shows the ratio of cross sections for the dielectron production in $p + n \to pne^+e^-$ to the one in $p + p \to ppe^+e^-$ as a function of the invariant mass in comparison to the two models of Shyam/Mosel [71] and Bashkanov/Clement [72]. A better agreement with the first model assuming emission from the meson line can be seen.

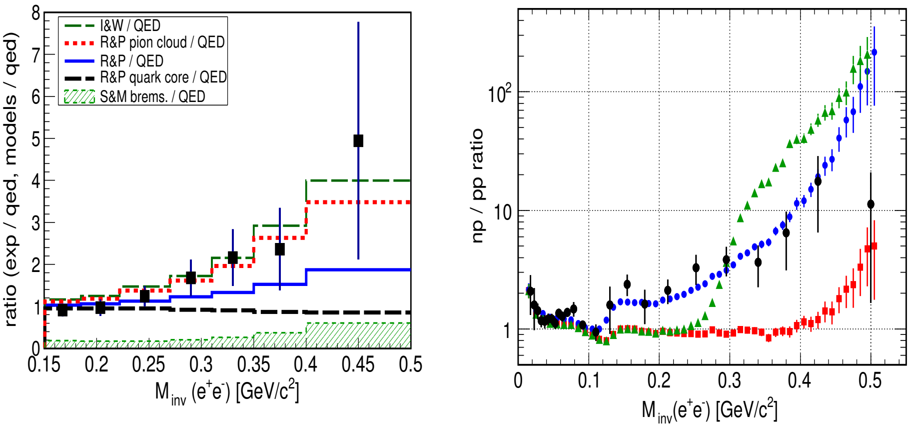

Figure 1.8: Left: Ratio of the differential decay rate of the $\Delta(1232) \rightarrow Ne^+e^-$ decay to the one expected for a point-like particle ("QED") compared to the models of [73] (IW), [76] (RP) and its two components: quark core and pion cloud. Right: Ratio of the cross sections for the exclusive dielectron production in p+p and n+p collisions at 1.25 GeV compared to models of Shyam/Mosel (blue circles) [71] and Bashkanov/Clement (green triangles) [72]. Red squares display ratio of Δ contributions in both reactions.

This conclusion seems also to be confirmed by a measurement of the polarization of the virtual photon by means of electron angular distributions in the photon rest frame (so called helicity frame). The measurement shows a change in the electron anisotropy from the $1+cos^2\theta$ expected for the $\Delta(1232)$ decay to a more isotropic distribution expected for the ρ contribution (for more details see [17]).

At higher beam energies Dalitz decays of the η, higher mass baryon resonances and two-body decays of the ω mesons contribute to the invariant mass above the π^0 mass [16, 40, 77]. The description of the Dalitz decays of higher mass baryon resonances is subject to uncertainty due to the lack of experimental information on the branching ratios and the q^2 dependence of the involved etFF. Various calculations describe such decays as a two-step process with the resonance production and its subsequent decay into ρN, followed by the meson two-body e^+e^- decay. Such a picture is equivalent to strict Vector Dominance Model (VDM), where the resonance-meson coupling is saturated by ρ.

Fig. 1.9 (left panel) presents the dielectron invariant-mass distribution from a measurement of inclusive e^+e^- production in p+p collisions at 3.5 GeV by HADES [40] in comparison to a hadronic cocktail calculated by GiBUU [76]. As one can see at $M_{ee} > 0.5$ GeV$/c^2$ the yield is completely determined by the contribution of baryonic resonances and the two-body decays of ω. The contributions of the baryonic Dalitz decays are shown separately for the $N^*(I=1/2)$ and $\Delta^*(I=3/2)$ (denoted as VDM). The production rates of these resonances were fixed from fits to available data of meson production in pion and proton collisions (for details see [78] and references therein). In particular, they describe, with some modifications, also exclusive one pion and dielectron production measured by HADES at the same energy [19]. The right panel of Fig. 1.9 shows the respective e^+e^- invariant mass distribution but for the exclusive ppe^+e^- final state. The solid line was obtained with the original parametrization of the resonance production used in GiBUU while the dotted line uses a fit to the one-pion production measured by HADES and reduced branching ratios for the $R \rightarrow \rho N$ decay (for details see [19]). In the calculation of the inclusive production, the etFF of $\Delta \rightarrow N\gamma^*$ from the covariant quark model of Ramahlo-Peña have also been

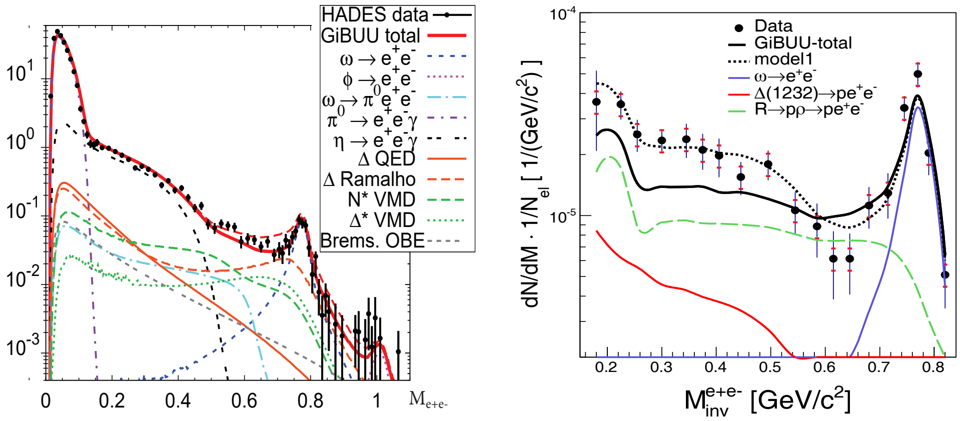

Figure 1.9: Left: Invariant mass distribution for inclusive e^+e^- production measured in p+p collisions at 3.5 GeV by HADES [40] in comparison to the hadronic cocktail calculated by GiBUU with and without $\Delta \to N\gamma^*$ etFF from [76]. Contributions of higher mass resonances are depicted separately. Right: Exclusive ppe^+e^- final state compared to the original predictions of GiBUU (solid curve) and the modified production resonance cross sections inferred from the analysis the one pion production (dashed curve), see for more details [19].

tested. Because of the higher beam energy a prominent enhancement at the vector meson pole is visible (orange dashed line). The inclusion of the form factor seems, however, to deteriorate the agreement with data. It remains however questionable if it is justified to apply it for Δ masses far-away from the resonance pole.

Note that thanks to the exclusive reconstruction of ppe^+e^-, the η Dalitz contribution, dominant in the inclusive spectrum, is completely removed and the invariant mass spectrum is dominated by the contributions from baryonic decays. The good agreement with the experimental data indicates the validity of VDM for baryon decays. However, a complete separation of the contributions of individual N^* and Δ^* resonances was not possible, which motivated also the experiments with pion beams discussed in the next section.

1.2.2 Pion-nucleon interactions

A first experiment with the GSI pion beam was realized in 2014 with two weeks of beam on target in total. A first run was dedicated to strangeness production off cold matter in pion-induced reactions on light (^{12}C) and heavy (^{184}W) nuclei at a beam momentum of 1.7 GeV/c. The goal of the second run was to measure 2 π- and dilepton production in π^-p reactions around the pole of the $N(1520)$ resonance using both polyethylene and carbon targets. Data at four different pion beam momenta (0.656, 0.69, 0.748 and 0.8 GeV/c) were collected, with the largest statistics obtained for 0.69 GeV/c momentum, sufficient for dielectron production studies.

The obtained two-pion $\pi^+\pi^-n$ and $\pi^-\pi^0p$ data samples have been included in the multichannel Partial Wave Analysis (PWA) of Bonn-Gatchina together with other world data on single and double pion production in photon, pion and electron induced reactions. One should emphasize that the HADES data is the only sample with charged double pion channels and hence is sensitive to the ρ production. Other world data on these channels are available only in form of total cross sections and can not be used for a state-of-the-art PWA. On the other hand, high quality data obtained with the Stanford Crystal Ball experiment for

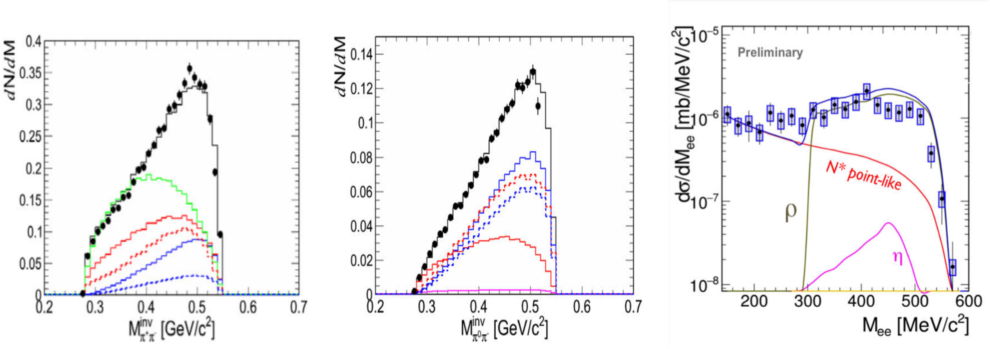

Figure 1.10: Invariant-mass distribution of $\pi^+\pi^-$ (left) and $\pi^-\pi^0$ (middle) pairs in comparison to a PWA analysis with the final states σN (green), $\Delta\pi$ (red), and ρN (blue). The contribution to the latter originating from $D_{13}(1520)$ is shown by the blue dashed line together with the total two-pion contribution (red dashed curve). Right: electron-positron pairs after selection of events corresponding to the free or quasi-free reaction (dots). Data are compared to simulations for emission by point-like baryonic sources (red curve) and by off-shell ρ mesons (brown curve) extracted from PWA (shown on the plots in the left panel). The contribution of the η meson Dalitz decay is indicated in magenta.

the two neutral pion production measured at similar energies are very valuable to constrain two-pion production in the $I = 0$ channel. Combining all these channels, the extraction of the various final $2\pi N$ ($\Delta\pi, \sigma N$ [2], ρN) and the initial resonance states became possible. Fig 1.10 shows the di-pion invariant-mass distributions (left and middle panels) together with the PWA decomposition into the above-mentioned final states measured with $\pi^- p$ reactions at $p = 690$ MeV$/c$. The background from pion reactions on carbon has been subtracted using π^-+^{12}C data normalized to the same luminosity determined by the known target thickness and beam intensity measured by in-beam counters. A direct comparison of the contribution of the $\rho^{-,0}N$ final state to the total contribution of the dominant $D_{13}(1520)$ resonances allowed also for the precise extraction of the respective branching ratio (BR=$12 \pm 2\%$).

The obtained mass distribution of the ρ meson in the $\pi^+\pi^-$ final state has been converted into a contribution to the e^+e^- invariant mass distribution using the Vector Dominance Model (VDM) assumption and it is shown in Fig. 1.10. Adding to this ρ contribution a cocktail of the Dalitz-decays expected from point-like baryon resonances, the observed exclusive e^+e^-n dilepton production can be described quite nicely. This demonstrates the consistency between the dilepton and double pion production channels and suggests that the involved time-like baryonic electromagnetic transitions can be described by VDM. The ρN couplings of the $D_{13}(1520)$ and the validity of the VDM in baryonic decays are of importance for calculations of the in-medium spectral function of the ρ and as such impact also the emissivity of strongly interacting matter.

1.2.3 Hyperon-nucleon interactions

The study of the hyperon-nucleon and hyperon-nucleon-nucleon interaction has become more and more crucial in recent years due to its connection to the modelling of astrophysical objects like neutron stars. It appears that in the inner core of a compact star the existence

---

[2] σ means a channel with $I = 0$

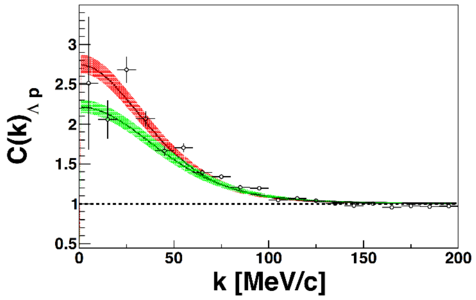

Figure 1.11: Comparison of the experimental Λ-p correlation function (open circles with error bars) to the LO (green band) and NLO (red band) scattering parameter set. The error bands in the theory curves correspond to the errors of the Λ-p source size determination.

of hyperons is possible since their creation is often energetically favored in comparison with a purely nucleonic matter composition. However, in models, the appearance of these additional degrees of freedom generally implies a softening of the nuclear equation of state incompatible with the recent observation of neutron stars with two solar masses. This leads to the so-called 'hyperon puzzle'. Many attempts were made to solve this puzzle, *e.g.* by introducing three-body forces leading to an additional repulsion that counterbalances the large gravitational pressure and finally allows for larger star masses [79]. Another possibility is offered by calculations using a chiral effective field theory approach (χEFT). The results [80] with leading order (LO) and next-to-leading order (NLO) demonstrate an attractive interaction for low hyperon momenta ($p < 600\,\mathrm{MeV}/c$) but for higher momenta NLO results show a repulsive interaction.

To contribute to this question with HADES data we use the femtoscopy technique to study the scattering lengths and effective ranges for hyperon-nucleon pairs produced in p+A collisions [81] (an alternative to scattering experiments). Femtoscopy is based on the investigation of the correlation function of a particle pair at low relative momentum. The large statistics collected for p+Nb at 3.5 GeV allow us to investigate the Λ-p interaction strength by comparing the experimentally obtained correlation function to a model containing results of scattering parameters calculated in the χEFT framework at LO and NLO. The Λ-p correlation function is shown in Fig. 1.11 in comparison to calculations with LO and NLO results (both versions are plotted separately). The statistical error of data is presently still too large to derive conclusions but the sensitivity of the method is demonstrated.

CHAPTER 2

Experimental Setup at SIS18

Contents

2.1 Detector Performance

HADES is a unique apparatus installed at the heavy-ion synchrotron SIS18 at GSI Darmstadt. It has a large acceptance for charged particles and is optimized to identify very rare electrons and positrons in a huge hadronic environment, which exceeds the electron signal by many orders of magnitude in multiplicity. The HADES spectrometer (see Fig. 2.1) consists of six identical sectors covering the full azimuth and polar angles from 18° to 85° measured relative to the beam direction.

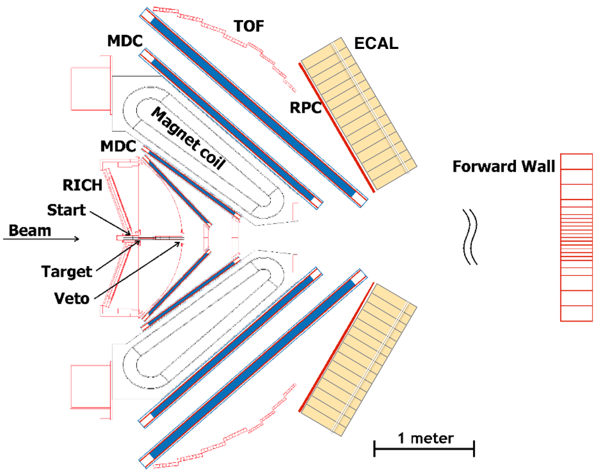

Figure 2.1: Schematic side view of the HADES detector showing its compact design. The detectors are symmetrically arranged in the azimuthal angle around the beam axis. The distance to the target of the forward wall is typically 6 m.

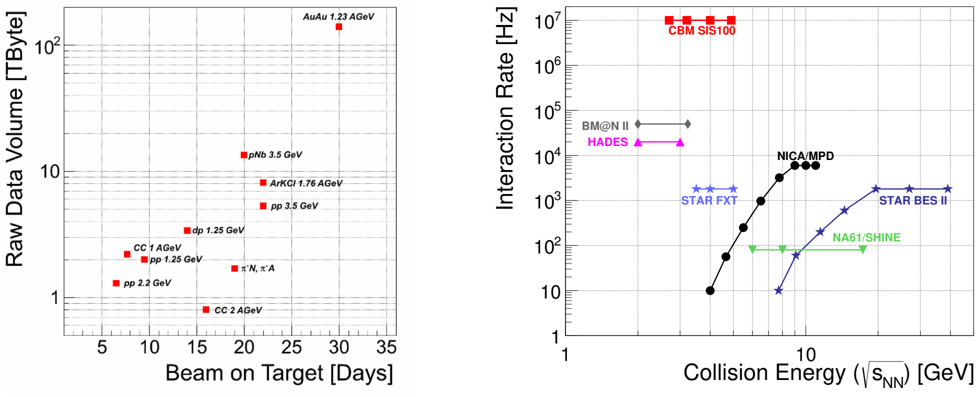

Figure 2.2: Left: Total amount of collected raw data in previous HADES runs. Right: Interaction rates achieved by existing and planned heavy-ion experiments exploring the high μ_B region of the QCD phase diagram as a function of center-of-mass energy [82]. High-rate experiments are also proposed at J-PARC [83] and at the SPS [84], but are still in a conceptual stage.

Each sector of the spectrometer contains a Ring-Imaging Cherenkov Detector (RICH) operating in a magnetic field-free region, two drift chambers (MDCs) in front of the magnetic field, and two outer MDCs behind the magnetic field, time-of-flight detectors based on scintillator rods (ToF) for $\theta > 45°$ and time-of-flight detector based on resistive plates (RPC) for $\theta < 45°$ combined with an electromagnetic calorimeter (ECAL) that replaces the pre-shower detector in previous campaigns. Momentum measurement of charged particles is achieved by tracking the particles in front off and behind the toroidal field generated by six superconducting coils arranged symmetrically around the beam axis. A powerful and flexible trigger system selects events with defined multiplicity or topological pattern of charged hits in the TOF detectors. With these design features, HADES can take data with high quality and statistical significance.

2.1.1 Rate capability

As of now, HADES has measured rare and penetrating probes in p+p, n+p, C+C, p+Nb, Ar+KCl and Au+Au as well as in a test run π^-+PE, π^-+C, and π^-+A collisions. The raw data volumes collected are shown as function of run duration (in days) in the left panel of Fig. 2.2. Until 2010, due to the limited granularity of the inner time-of-flight system, measurements were restricted to medium-size collision systems. The combined measurement of dielectrons and strangeness in Ar+KCl collisions has provided intriguing results and asked for heavier collision systems at this energy and higher statistics. A major improvement of the spectrometer in terms of granularity and particle identification capability was achieved with the new RPC time-of-flight detectors. The data acquisition was fully replaced introducing a modular system integrating trigger distribution, data transfer and a slow control data traffic into a single optical link. With this detector upgrade the Au+Au beam time took place in April 2012. A gold beam of up to 2×10^6 ions per second was incident on a 15-fold segmented gold target. Within the 557 hours of beam on target a total of 7.3×10^9 events with a total data volume of 140 Tbyte were collected. This was, compared to the data volumes recorded in the previous beam times, an enormous gain of statistics.

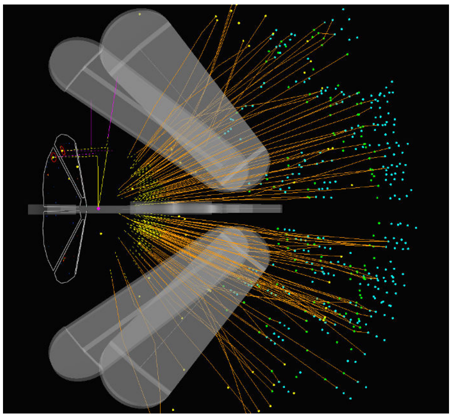

Figure 2.3: Event display of a Au+Au collision at 1.23 A GeV. Orange lines: reconstructed tracks, blue and cyan points: reconstructed hits in the ToF and RPC/Pre-Shower detectors, red circles: reconstructed RICH rings. The magnet coils surrounding the beam axis are shown in gray color.

The rate capabilities of the HADES DAQ system depend on the particle multiplicity of the collisions under investigation. The current rate capabilities of HADES are presented in Fig. 2.2 (right panel) together with existing and planned heavy-ion experiments exploring the high μ_B region of the QCD phase diagram. In the Au+Au run the DAQ system was operated at peak rates of 14 kHz, although limited to 8 kHz for most of the experiment due to rate limitations imposed by the detectors themselves. Based on our experience, for lighter collision systems like Ag+Ag we expect to achieve rates of about 10 kHz and for elementary reactions up to 20 kHz. One central limiting factor, especially in the case of elementary collisions, is the current front-end electronics of the MDC. Their replacement by state-of-the-art modules, as discussed in section 2.2.5, will enable us to increase this speed to about 80 kHz without changes to the current read-out procedures.

Once the MDC electronics is replaced, we will be able to change the current trigger-busy-release system architecture to a more performing scheme. Then, part of the system can be operated in a free-running mode without having to transport busy information from the very front-end to the central control system. The transport latencies can therefore be reduced and the trigger rate can be increased to an estimated 200 kHz for light collision systems (low-multiplicity events).

2.1.2 Event Reconstruction

Up to 140 charged particles are detected in the acceptance for central Au+Au collisions. An example of an event display of a recorded Au+Au collision at 1.23 A GeV is shown in Fig. 2.3. For the track reconstruction this situation is challenging since in the inner MDCs the track density can reach up to 0.75 tracks/cm. Compared to the drift cell size of 5×5 mm^2 this results in a double-hit probability of $\sim$ 30% at low polar angles. Due to the length of the drift cells long range correlations between distant particle tracks are introduced in the track reconstruction leading to a high number of combinations and fake tracks. Nevertheless, an efficient and accurate event reconstruction is achieved with a new approach for tracking in the high track density environment. For hadronic particle tracks with a momentum larger than 400 MeV/c a reconstruction efficiency of larger than 80% has been achieved.

For the anticipated measurement of Ag+Ag collisions at 1.65 A GeV the maximum track densities are by $\sim$ 30% lower compared to the discussed Au+Au collisions (as shown in Fig. 2.4) leading to a by $\sim$ 8% improved efficiency (see Fig. 2.5). Due to the new MAPMT based RICH photon detector the reconstruction efficiency for electrons and positrons is improved by more than a factor 3.

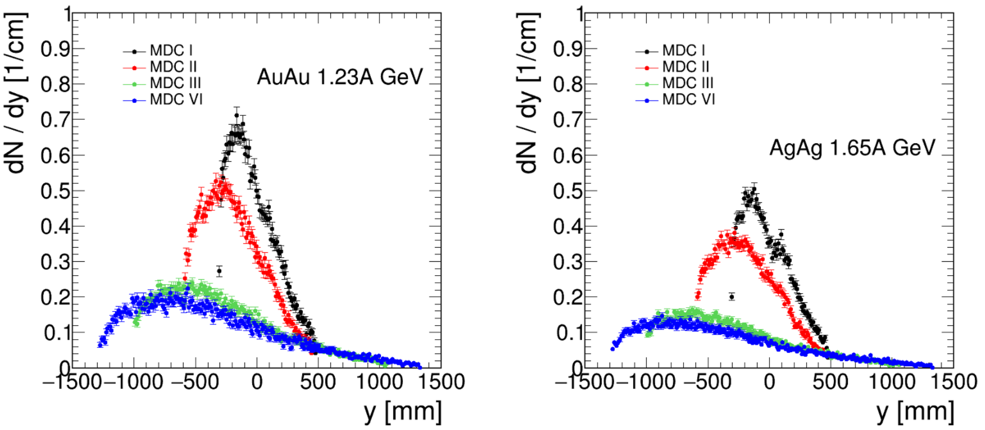

Figure 2.4: Simulated differential track density as function of detector y coordinate. Left: Au+Au at 1.23 A GeV. Middle: Ag+Ag at 1.65 A GeV. Right: Track reconstruction efficiency of Au+Au collision at 1.23 A GeV (open symbols) and Ag+Ag collision at 1.65 A GeV (solid symbols).

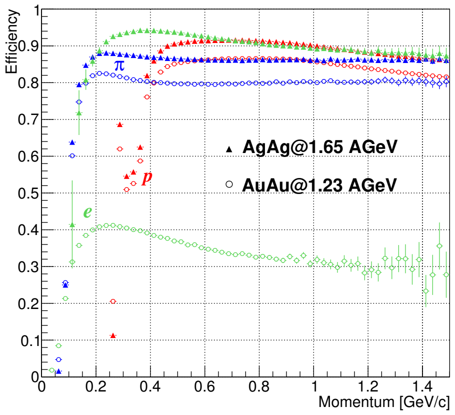

Figure 2.5: Track reconstruction efficiency of Au+Au collision at 1.23 A GeV (open symbols) and Ag+Ag collision at 1.65 A GeV (solid symbols). Red symbols: reconstruction efficiency of protons, blue symbols: of charged pions, green symbols: of electrons and positrons.

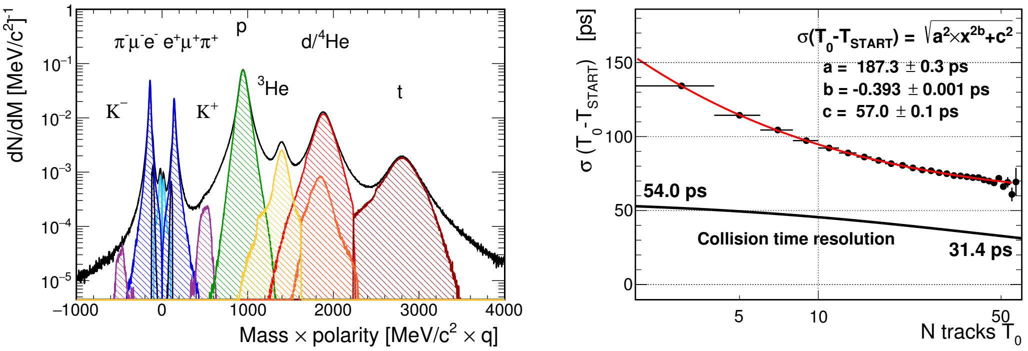

Figure 2.6: PID in Au+Au collisions at 1.23 A GeV. Left: Mass spectrum of all reconstructed tracks (black curve) and identified particles (shaded areas). Right: Collision time accuracy.

2.1.3 Particle Identification

The time-of-flight technique plays a central role in particle identification in HADES. The time-zero measurement is performed by a segmented diamond detector (START), placed in front of the target, and two fast "STOP" detectors *i.e.* ToF and RPC, placed behind the magnet and the tracking detectors, with 150 ps and 70 ps time resolution respectively. The velocity of the particle is calculated from the time difference between the STOP and START signals divided by the track length measured from the collision vertex to the time-of-flight walls. Although the resolution of the diamond detector is already of the order of 60 ps, the collision time determination can be improved further if tracking information is included.

This technique, called T_0 reconstruction, uses the most probable mass hypothesis for every track that has high reconstruction quality to calculate the residual between the time-of-flight from the reconstructed momentum and the measured time. The hypothesis for T_0 is then derived event-by-event from the weighted average of all calculated residuals. To quantify this procedure, a dedicated Monte-Carlo simulation with detailed detector response functions and including effects like multiple scattering and energy loss was used.

The measured performance in Au+Au is shown in Figure 2.6, where the black curve depicts the accuracy of the time-zero determination when calculating the weighted average of T_0 and START time. For the most peripheral collisions 54 ps and for most central collisions 31.4 ps are achieved. Particle identification is further improved by the measurement of the specific energy loss in the tracking detectors. Figure 2.6 shows the reconstructed mass spectrum and the identified particles by shaded areas. More than 90% of all reconstructed tracks are identified. The rest are random combinations of traces matched to time-of-flight detectors. For lighter systems like Ag+Ag the expected identification performance is similar to that achieved for Au+Au.

2.2 Status of the upgrade projects

During its first experiment campaign (2002 – 2008), HADES was operating with a 18-fold segmented inner time-of-flight detector system. During a shutdown period of SIS18, the HADES collaboration replaced this system by an RPC system with more than 1000 individual cells. Also the innermost layer of drift chambers was replaced. Still, with the start of FAIR Phase-0, most of the detector systems will have reached an age of 15 years. For reasons of better photon detection efficiency, the UV detector of the RICH will be replaced by MAPMTs, and the Pre-Shower detector (polar angle coverage from 18 to 45 degree) will be taken out and an electromagnetic calorimeter (ECAL) will be put in place. Moreover, the success of the experimental program addressing elementary reactions calls for an instrumentation of the acceptance region between polar angles of 0.5 to 6.5 degree in order to enlarge the phase space coverage. Most of these upgrade projects, profit by close synergies with instrumentation projects of FAIR (PANDA and CBM).

2.2.1 The Electromagnetic Calorimeter

The addition of an electromagnetic calorimeter (ECAL) to HADES will allow to study via photon measurements new reaction channels involving *e.g.* the production of neutral mesons, neutral $\Lambda(1405)$ or $\Sigma(1385)$ resonances in elementary and heavy-ion reactions. An additional advantage of such a device is the resulting improvement of the electron-to-pion separation at large momenta. The detector is based on 978 lead glass modules recycled from the OPAL experiment. It is divided into 6 sectors, and it will cover forward angles of $16° < \theta < 45°$ and almost the full azimuthal angle. Front and side views of the ECAL

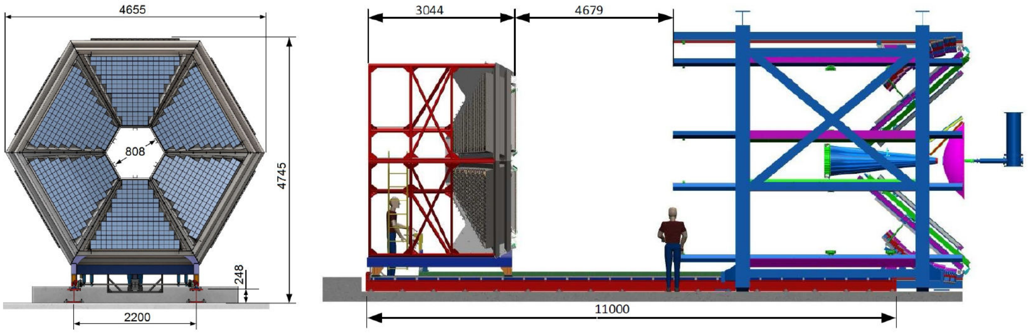

Figure 2.7: Calorimeter layout - front view (left) and side view in pulled out state, current HADES setup being on the right (right). Dimensions are in millimeters.

detector can be seen in Fig. 2.7. Single components of one ECAL detector module can be seen in Fig. 2.8, left panel. The TDR has been approved in 2014 by the FAIR ECE. The project is carried out by groups from Rez, Krakow, Moscow, Bratislava, Frankfurt, Darmstadt, Munich and GSI.

The development of the detector was supported by two gamma beam tests at MAMI Mainz and one beam test at the T10 beam line at CERN. The relative energy resolution measured at MAMI Mainz for two photomultiplier types can be seen in Fig. 2.8 right, together with a 1" photomultiplier (finally discarded as not suitable for the ECAL readout).

The readout of the detector is based on PaDiWa AMPS boards (charge to width measurement) developed especially for the calorimeter and connected to a TRB3 setup [85]. A dedicated optical monitoring system has been developed for the ECAL. It is based on a laser LED and a microlens array with optical fibers which allows to send the same amount of light into each single ECAL module. These light pulses invoke the same signal on the output as measured for real particles.

All R&D is now completed and large scale assembly of the modules started in 2016. In the current funding concept, photomultiplier of two different types are installed. The tight budget forces the HADES collaboration to partly reuse 1.5" EMI 9903KB photomultipliers

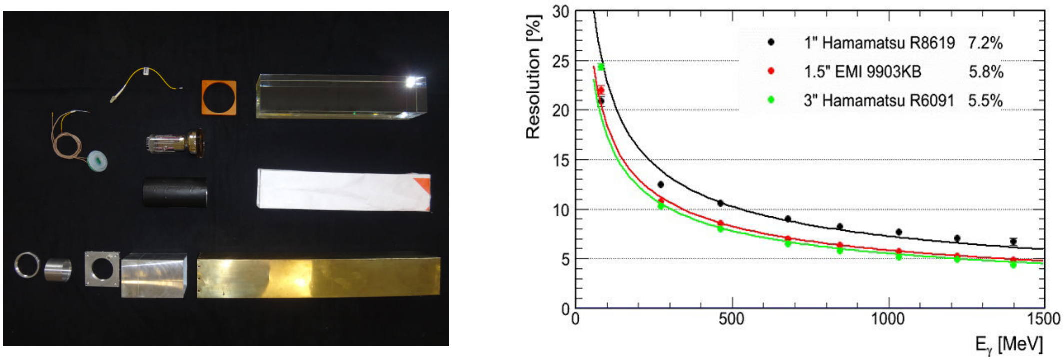

Figure 2.8: Left: Construction parts of one module of the ECAL detector. Right: Energy resolution of photomultipliers tested for the ECAL detector (numbers behind the names indicate the resolution for 1 GeV photons).

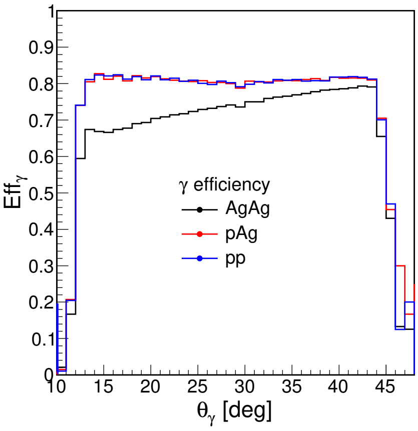

Figure 2.9: Single photon efficiency as a function of polar angle for three collision systems: Ag+Ag (black curve), p+Ag (red curve) and p+p (blue curve).

recovered from the MIRAC (WA98) detector, for the rest new 3" Hamamatsu photomultipliers R6091 are purchased. The optical monitoring system for all 6 sectors was ordered and will be delivered at the end of August 2017. The support frame for the ECAL is currently being manufactured and will be installed in the HADES cave also in August 2017. After that it will be filled with modules and electronics (with possibly not all 6 sectors ready in 2018 due to limited funds) to be operable for the planned experiments at SIS18.

A full GEANT3 simulation of the ECAL detector and all other detectors of the HADES setup was performed. Figure 2.9 shows the single photon efficiency as a function of polar angle. In case of Ag+Ag collisions we do observe an angle dependence due to the high hadron multiplicity at low angles, which is not observed in proton induced reaction, where the particle multiplicity per event is smaller. On average the photon efficiency for Ag+Ag is 71% and for proton induced reactions is 78%.

2.2.2 RICH Photon Detector

The MWPC based gaseous RICH VUV photon detector with its CsI photon converter is currently being replaced by an arrangement of multi-anode photo multiplier tubes (MAPMTs, Hamamatsu H12700C) with blue-enhanced high quantum efficiency photo cathodes. The detector modules composed of 6 MAPMTs and integrated together with all required readout electronics on a backplane are developed together with CBM and will also be used as UV photon detectors in the CBM RICH. The pixel size (5.8×5.8 mm^2) of these devices perfectly matches the pad geometry of the old MWPC detector and guarantees reasonable position resolution of single photon hits and efficient ring image recognition. The MAPMTs are arranged on two aluminum carrier frames such as to fit as close as possible to the focal surface of the RICH mirror. Altogether 432 MAPMTs (27.6k readout channels in total) arranged on 72 super-modules with 3×2 individual MAPMTs each will be mounted inside the existing gas tight detector chamber and flushed with nitrogen. A schematic view of the new RICH configuration and the design of the new photon detector device is depicted in Fig. 2.10.

The newly developed readout front-end (DiRich) comprises pulse amplification, discrimination, time-to-digital conversion and time-over-threshold measurement for single photon signals from each individual MAPMT pixel. Twelve densely packed DiRich cards serve six MAPMTs and are arranged on a super-module backplane together with a power- and combiner card providing connection to the TRBnet of the HADES data acquisition system.

A partially equipped backplane is shown in the left panel of Fig. 2.11. Presently ongoing laser measurements with MAPMTs and final DiRICH prototypes show the expected performance with respect to single photo electron detection efficiency and rate capability, as demonstrated in the right panel of Figure 2.11.

The high quantum and single photo electron detection efficiency, low cross talk probability, and a new versatile ring finder algorithm lead to an expected superb single e^+/e^- identification efficiency across the whole detector area, in spite of the very short radiator length at small polar angles. In particular, the ring finder allows to efficiently discriminate overlapping rings even for very close e^+e^--pairs with opening angles down to $\delta\Omega \simeq 3^\circ$. Corresponding results are shown in Fig. 2.12 for simulations with conservative detector parameters and promise a significant reduction of misidentified combinatorial e^+e^--pair background also in heavy-ion reactions.

All MAPMTs are in house, individually tested, qualified and ready for installation into the prepared detector frame. After successful completion of an upcoming test campaign in the HADES cave with a 24 MAPMT prototype system, the mass production of the readout cards will start. With the detector fully instrumented, thorough high rate readout tests are scheduled for late 2017 followed by integration into the RICH in the beginning of 2018.

Figure 2.10: Left: Exploded view of the new RICH device after exchange of the gas-filled MWPC photon detector. Right: Front view of the new UV photon detector (active diameter d = 130 cm) with the arrangement of 64-anode photo multiplier tubes.

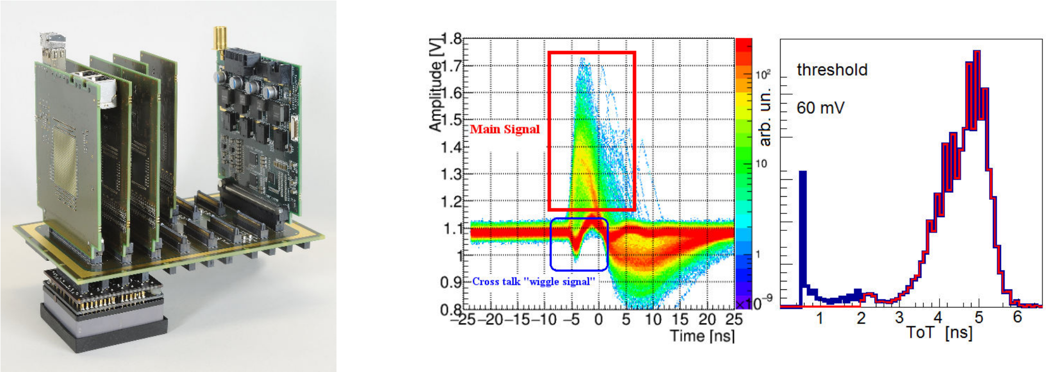

Figure 2.11: Left: Super-module backplane for 3 × 2 MAPMTs partially equipped with DiRICH front end cards, combiner, power board, and one MAPMT. Right: Single photon response of the DiRICH amplifier stage with time-over-threshold (ToT) distribution.

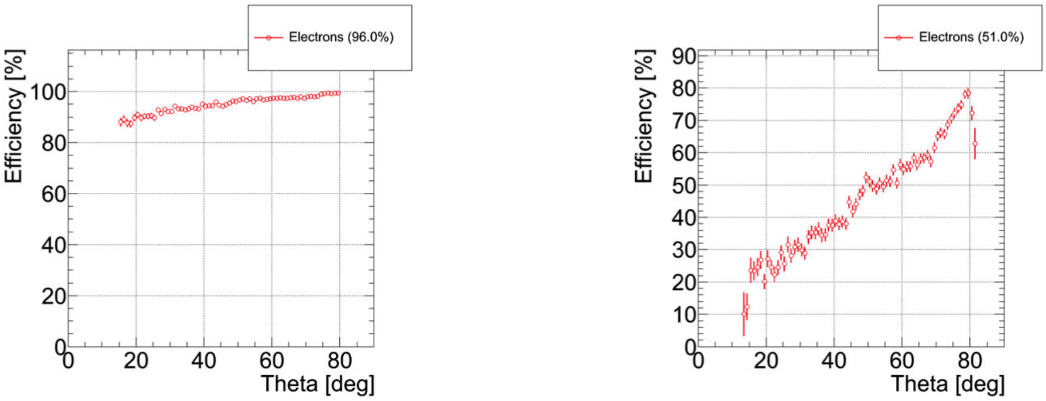

Figure 2.12: Left: Polar angle distribution of the expected single electron resp. positron detection efficiency. Right: Same, but for the recognition efficiency of double rings from close di-electron pairs with opening angles of $\delta\Omega \simeq 3^\circ$.

2.2.3 Forward Detector System

To extend the acceptance of the HADES Spectrometer towards lower polar angles, 0.5° – 6.5°, a dedicated Forward Detector is being constructed. This detection system consists of two tracking stations placed 3.1 and 4.6 m downstream of the target and is based on straw tubes. It is followed by a high precision time-of-flight wall based on RPC technology and a high granularity scintillator based hodoscope. As this detector will operate in a field-free region the particle identification has to be performed based on $\mathrm{d}E/\mathrm{d}x$ and time-of-flight measurements. Additionally, the straw tube tracking stations will be used for reconstruction of off-vertex decays.

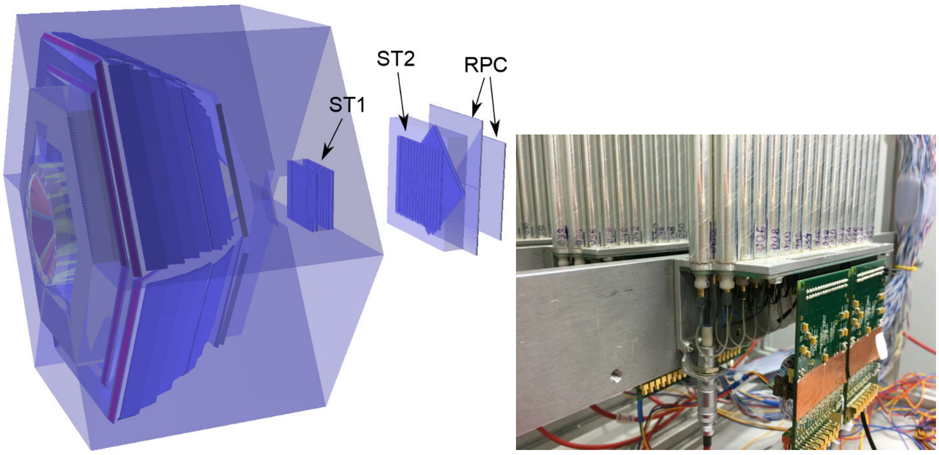

Figure 2.13: Left: A display of HADES with the Forward Tracking Detectors. Right: Straw detectors under the test in the detector laboratory in Krakow.

The Forward Tracking Detectors consist of two stations, each composed of 8 layers of self-supporting straw tubes with 10 mm diameter (see Fig. 2.13). The layers are built from vertical straws rotated by $0, 90, 0, 90$ and $0, 90, -45, 45$ degree around the beam axis. The position resolution of the detector amounts to around 150μm which, for the given detector geometry, provides track reconstruction with angular resolution of $\sigma_\theta = 0.5$ mrad for 2 GeV protons. The Straw Trackers are currently assembled by the Krakow and FZ Juelich teams, based on developments for the PANDA Forward Tracker. LIP Coimbra is producing the Forward RPC.

The increase of acceptance will play a significant role in studies of $N(\pi) + N$ and $p + A$ reactions where this detector is essential for exclusive channel and PWA analyses of hyperon production and decays like for example $\Lambda \to p\pi^-, \Lambda^*(\Sigma^*) \to \Lambda e^+ e^-$ (hyperon transition form-factors) and $\Xi^- \to \Lambda\pi^-$.

For heavy-ion reactions the Forward Detector will consist only of an highly granular plastic scintillator (the other two components will be removed). The detector will be focused on reaction plane reconstruction and precise centrality measurements.

2.2.4 Start Detector Upgrade

For experiments with HADES, a radiation hard and fast beam detector is required. The detector is placed directly in the beam either close in front of the target (START) and in some configurations also at the exit of the RICH detector (VETO). To properly handle the rates the detector has to be segmented (see Fig. 2.14) and radiation hard. The time

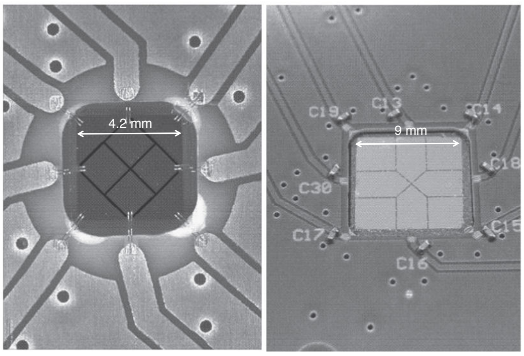

Figure 2.14: Enlarged photograph of the segmentation of the metal surface of the scCVD diamond T0 detector with size of 4.2 mm × 4.2 mm (left) and the reference pcCVD diamond detector with a size of 9 mm × 9 mm (right). Both diamonds were mounted on PCB plates and the readout electrodes were bonded to the PCB traces.

resolution of the START should be as good (time-zero measurement with $\sigma_{t0} < 50\,\mathrm{ps}$) that the time-of-flight measurement is not deteriorated by it. While this is mandatory for proton- and pion-beam induced reactions, in case of heavy-ion collisions the time-zero determination is augmented by taking the average of a properly corrected stop measurements of all charged particles in the acceptance. These requirements can in general be fulfilled by utilizing single-crystal Chemical Vapor Deposition (scCVD) diamond based detectors. High counting rate capability of the diamond detector (up to 10^7 ions/s/mm^2) has been shown in the Au+Au run. The measured radiation damage to the diamond material by Au ions has been quantified and it has been shown that for a degraded detector the energy resolution measurement capability reduces significantly whereas timing properties are worsened only slightly [86]. A similar concept for T0 measurement will be used during the Ag+Ag run.

The detection of minimum-ionizing particles, however, remains challenging since one has to deal with very small amounts of induced charge carriers while the expected high rates require special emphasis on the read-out electronics. A read-out concept for diamond detectors for minimum ionising particles will be based on the already well established TRB3 (Trigger and readout board - version 3) platform, developed at GSI. The board provides 260 high precision (RMS < 12 ps) multi-hit FPGA-TDCs and serves as a flexible data acquisition system (DAQ). The available comprehensive software package allows on-line monitoring capabilities including basic analysis. A large variety of front-end electronics is available in order to extend its functionality.

2.2.5 MDC FEE Upgrade

The $\simeq$ 27.000 sensing wires of the drift chambers are currently read-out by means of dedicated front-end electronics, mounted on the frames of the detectors. The analog section is based on the ASD-8 ASIC, featuring amplification, shaping and discrimination with a common threshold of 8 channels with a typical integration time of 7-8 ns. A semi-customized ASIC for time digitization provides both, drift time and valuable time-over-threshold information. Built around the year 2000, the system meanwhile suffers from an increasing number of dead channels and the data transfer bandwidth turned out to be a limiting factor of the DAQ. Moreover, in high-rate applications it is recommended to employ multi-hit capability of the read-out to avoid efficiency losses due to occupied channels fired by random coincidences (notably δ-electrons). Also, a higher detection sensitivity is desirable to increase the stability of the detector under high load by lowering the gas gain. Besides that, the HADES tracking algorithms would accept slightly worse spatial resolution while profiting from an improved noise immunity.

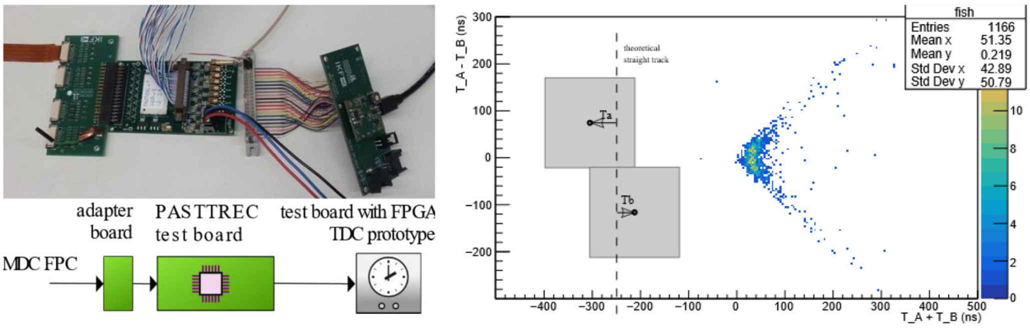

Figure 2.15: Left: PASTTREC read-out line, here equipped with a stand-alone FPGA-based prototype TDC. Right: Correlating two adjacent drift cells A and B by plotting the drift time difference of cosmic tracks with perpendicular impact against the corresponding sum. This representation is used to assess the resolution of the drift time measurement.

Pursued by groups from Frankfurt and GSI, state-of-the-art solutions based on available ASICs (the ASD-8 is no longer on the market) and time digitization realized in FPGAs are being studied in order to replace the old FEE in the near future. A promising replacement read-out chip candidate is the PASTTREC ASIC [87], developed at Jagiellonian University, Krakow, for reading-out straw tubes *e.g.* of the PANDA experiment and future forward tracking in HADES. This chip is currently at the focus of our investigations. It is supplemented by a high precision FPGA-based TDC, implemented on a TRB3 board [88]. In parallel, a cost-efficient and lightweight but coarse binned (500 ps) FPGA-based prototype TDC was successfully tested which is foreseen to replace the currently used dedicated TDC ASICs. To arrive at conclusive performance results, the tests are being conducted under realistic conditions in direct comparison to the present ASIC. To do so, a spare drift chamber is employed and both signal-to-noise and dE/dx as well as time resolution is systematically characterized with radioactive sources and cosmic rays. A test beam time is planned to take place soon.

Figure 2.15, left side, depicts the PASTTREC read-out line, which is attached by means of a dedicated flex cable to the detector. One key issue is the compatibility of the present flex-based signal routing and the PASTTREC ASIC, mounted on a customized board, which significantly affects the noise immunity together with determining the optimum parameter settings of the PASTTREC chip. Due to the arrangement of two stereo angle layers it is possible to assess the time (and spatial) resolution by correlating adjacent drift cells. Plotting the difference against the sum of both drift time signals, see Fig. 2.15, right side, for perpendicular tracks of cosmic muons, and triggered by an external scintillator, allows to access the drift time resolution by projecting a selected data sample on the axis representing the drift time sum. This study, together with future beam tests, will help to answer the other key question on the possibility of assigning an ASIC optimized for straw tube signals which deliver more charge (operation at 2 bar and longer track path in a straw tube cell) to read out the mini (cell) drift chambers of HADES. The final decision on the replacement of the existing electronics is foreseen in the second half of 2017. The new MDC read-out is scheduled to be available for the year 2020.

Chapter 3

The physics program for FAIR Phase-0

Contents

The goal we pursue with the HADES physics program is to explore the microscopic structure of dense baryonic matter. In particular, we would like to understand to what extent hadrons change their properties once they are exposed to a hadronic environment and when they ultimately lose their hadronic character. An important part of this program is to carefully define the reference against which modifications of the hadrons are measured.

As main probes we use virtual photons detected via dielectrons, which directly couple to the electromagnetic current of hadrons, and the production of strange hadrons. The HADES collaboration would therefore like to use the opportunities of FAIR Phase-0 to address in particular the following physics topics outlined in section 3.1. In the subsequent sections, we briefly describe physics runs we would like to conduct in the coming years. Two of them, we propose for the period 2018–2019 and they are presented in more detail in chapter 4.

3.1 Key physics cases

3.1.1 Emissivity of baryonic matter around the vector meson mass region

To advance our understanding of the emissivity of strongly interacting matter, beyond having established the excess radiation in the low-mass region at the "low-energy frontier" as reported in chapter 1, a clear identification of the narrow vector mesons ω and ϕ in the dielectron invariant-mass distribution is essential. By comparing the ϕ multiplicity in the e^+e^- and K^+K^- decay channels, we can directly address the question whether narrow ϕ states exist before the system freezes out. With the set of measurements anticipated for Phase-0, we can study this question both in A+A (*cf.* s. 3.3) and p+A (*cf.* s. 3.5) collisions, *i.e.* in hot and dense as well as in cold QCD matter. In a similar way we can study the ω multiplicity in the e^+e^- decay channel. An interesting questions is whether the ω multiplicity would also be in line with assuming formation at chemical freeze-out according to statistical weights (*cf.* s. 1.1.3). This observation would provide an alternative approach to search for in-medium decays of narrow vector meson states. Indeed, the direct search for modifications of the line shape is extremely hungry in statistics and likely not possible with the harvest of the proposed here collision system and run time.

While collecting the statistics necessary to accomplish this task, we will also have access to the continuum radiation around $M_{ee} \simeq 1\,\mathrm{GeV}/c^2$. This mass region is of particular interest since besides the in-medium ρ spectral function also multi-pion processes start to contribute, like $\pi + \rho \to a_1$, driving chiral $(V - A)$ mixing. The latter processes, however, are not expected to be important in p+p collisions. Hence, the comparison to this reference will provide complementary information for understanding the emissivity of QCD matter. Moreover, the double-differential investigation of the continuum radiation, *i.e.* inspecting the transverse mass distribution for bins of growing invariant mass $(\mathrm{d}^2N/\mathrm{d}m_t/\mathrm{d}M_{ee})$, will eventually allow to distinguish different emissions times for the various sources.

3.1.2 Search for in-medium modification of the light vector mesons by inspecting their line shape

Strong medium modifications are expected due to the coupling of (vector) mesons. These couplings have resonant character and hence are only strong if the relative momenta between these mesons and the (baryonic) medium are not too high. In a measurement of proton-induced ω production off nuclei (*cf.* s. 1.1.1) we found a strong disappearance effect when selecting e^+e^- pairs with moderate laboratory momentum ($p < 800$ MeV). Yet, the acquired statistics was by far not enough to address modifications of the line shape. In the case of proton-induced reactions the omegas are produced with substantial recoil in the laboratory and a cut on small momenta results in a drastic reduction of the total phase space. In a pion-induced reaction, this situation is by far more favorable (in fact this physics case was the driving force behind realizing a secondary pion beam at SIS18). Now, with the expected accelerator performance such an experiment is not only possible but very promising. We therefore aim for a long run using a medium-heavy target to optimize the volume *vs.* conversion in the target effect. The optimal choice for us is silver since this nucleus fits into the systematics of our proposed measurements.

3.1.3 Multi-strange baryon production

The comprehensive study of strange-hadron production by HADES including the most recent data in Au+Au at 1.23 A GeV unraveled unexpected features so far not consistently described by models based on microscopic transport theory. Most notable are the high yields of (hidden-strange) ϕ mesons and double-strange Ξ hyperons (*cf.* s. 1.1.2). These findings can potentially put into question former results based on comparisons of data to such transport models eventually biased by wrong assumptions. Yet, the situation is still not fully conclusive. To scrutinize further our understanding of strangeness production in heavy-ion reactions in the few- A GeV energy regime, error bars have to be substantially reduced, in particular for inclusive K^-, ϕ and Ξ spectra. The collision system Ag+Ag is best suited since it provides a maximum A_{part} around 200 while the beam energy can be raised by almost 0.5 A GeV w.r.t our previous Au+Au run, which will substantially increase the overall strangeness ($s\bar{s}$) production.

Attempts to better describe strangeness production with transport models include conjectures about unknown decay branches of heavy baryonic (non-strange) resonances into final states with open strangeness. Hence, the above measurements need to be accompanied by reference measurements using exclusive final states (*cf.* s. 3.1.3) and inclusive production off cold nuclear matter (*cf.* s. 3.1.4). A simultaneous description of strangeness production by microscopic transport off cold matter and in hot and dense matter can provide strong evidence for the validity of the models used.

3.1.4 Electromagnetic structure of excited Baryons and Hyperons

Our recent studies of the baryon resonances in the exclusive channel $\pi^- p \rightarrow e^+ e^- n$ revealed patterns of far off-shell ρ propagation in their electromagnetic decay into dielectrons. This raises the question to what extent the baryon's meson cloud is instrumental in transferring excitation energy into a virtual photon. Indeed, not too much is known about electromagnetic transition form factors (or the electromagnetic transition structure function) of baryons in the (soft) time-like region. In particular the role played by vector mesons in these transitions is of major importance. With our pion beam program outlined in section 3.2.1 we have unique opportunities to substantially contribute to this urgent problem.

A better understanding of the coupling of baryonic resonances to intermediary ρ mesons is also mandatory to validate emissivity calculations for hadron-resonance matter. Dense baryonic matter can also be viewed as a giant cloud of virtual mesons surrounding baryonic cores while carrying a substantial fraction of the energy density of the state. Such studies can therefore pave the way for searching new states of matter with the upcoming Compressed Baryonic Matter program at FAIR's SIS100.

3.1.5 Two-body particle correlations

Among all so far measured resonances the $\Lambda(1405)$ is the only one unanimously considered to be at least partially a molecular meson-baryon state. Measurements of $\Lambda(1405)$ in pion-induced reactions will provide important information to constrain the model calculations and to unravel the nature of $\Lambda(1405)$.

The planned experiments will also allow to perform other types of measurements requiring high statistics like the study of short-range NN correlations (SRC), two-particle correlation studies aiming at the determination of *e.g.* the $\Lambda - p$ scattering parameters and phase shifts. SRC provide direct insight into the short-range part of the nucleon-nucleon interaction while hyperon-nucleon correlations will give valuable information on the equation-of-state of neutron stars assuming the presence of strange hadrons in the core of these dense objects. In particular, thanks to the ECAL, also the $\Sigma^0 - p$ and $\Xi^0 - p$ correlation can be addressed in future measurements for the first time.

3.2 Pion beam experiments

The pion beam at GSI is a unique tool to understand the role of baryonic resonances in the production of meson and dielectrons in vacuum and in-medium. While pion-nucleon reactions provide information on the electromagnetic and hadronic couplings of the baryonic resonances, which are related to their intrinsic structure in terms of quark core and meson cloud, measurements in pion-nucleus reactions allow for the study of modifications of vector meson properties in cold nuclear matter. HADES is at the moment the only facility world-wide which combines a pion beam with dielectron spectrometry, an excellent particle identification and good secondary vertex reconstruction capabilities. In this sense, it acts as a precursor for existing and future meson beam facilities for baryon spectroscopy. The measurements we propose on baryonic resonances and cold hadronic matter will take advantage of foreseen improvements of the beam extraction and increase of the space charge limit in SIS18. In addition, with the ECAL, the capacity of HADES to provide high precision data for PWA of baryonic resonances with masses up to 2 GeV/c^2 will be extended to exit channels containing neutral mesons and photons. For example, measurements of the η, ω and $\Lambda(1405)$ via the $\Sigma^0\pi^0$ decay will become possible, which is important in view of the still controversial nature of the $\Lambda(1405)$.

3.2.1 Electromagnetic structure of baryonic resonances

While a lot of data exist for electromagnetic baryon transitions in the space-like region, where transition form factors or helicity amplitudes have been measured for many baryonic resonances, the time-like region is almost unexplored. As mentioned in section 1.2.1, the HADES collaboration has recently published the very first extraction of the $\Delta(1232)$ Dalitz decay ($\Delta \rightarrow Ne^+e^-$) branching ratio [18]. In addition, the first pion beam experiment in 2014 explored the electromagnetic structure of baryon transitions in the N(1520) region with significant preliminary results. However, this information is very scarce. We propose to continue these studies by investigating electromagnetic transition form factors of baryonic resonances in the third ($\sqrt{s} \sim 1.7$ GeV) and fourth resonance ($\sqrt{s} \sim 1.9$ GeV) regions. These data will be complemented by measurements of the hadronic channels necessary to control resonance excitation. The latter will be obtained by an energy scan in five equidistant energy steps of 30 MeV centered around the point where a high statistics dielectron measurement will be performed (as details are given in section 3.2.2). For the dielectron final state the events of all runs are summed while for the hadronic final states the individual information will substantially improve the partial wave analysis. The integral statistics collected should be sufficient to extract triple-differential dielectron distributions like the angular distributions of electrons in the virtual photon rest (helicity) frame for selected invariant mass and virtual photon emission angle bins. This will allow to extract spin density matrix elements as a function of the production angle and the virtual photon mass [89]. Since these elements are very sensitive to the resonance spin and mass dependence of the involved electromagnetic transition form factors (etFF), they constitute important observables which can be measured with sufficient precision in the planned experiments.

To start this program, which is complemented by the investigation of hadronic final states (*cf.* s. 3.2.2), we propose to use a beam of negative pions on polyethylene (PE) and carbon target, as in the first successful commissioning experiment (2014). The choice of PE target is dictated by the larger density (factor 2) of protons (4×10^{23} /cm^2) as compared to the one available in a LH_2 target and the absence of background originating from interactions with the target vessel. The latter is unavoidable due to the pion beam diameter (FWHM $\sim 1.5-2$ cm) which exceeds the diameter of the target. The background from interactions on carbon in the PE target can be very well controlled and subtracted as demonstrated in the first experiment [90]. Furthermore, for the very time demanding measurement of the $\pi^- p \to n e^+ e^-$ final state, additional statistics can be gathered from quasi-free πp reactions on the carbon nucleus, which can be selected via a cut on the e^+e^- missing mass centered around the neutron peak (for further details see [91]). Last but not least, additional measurements on the carbon target, necessary for the background subtraction, are interesting on their own as discussed in section 3.2.4.

We will choose for the next experiment a central cm energy ($\sqrt{s}$ =1.74 GeV) in the third resonance region 20 MeV above the threshold for ω production in π^-+p production where $\rho-\omega$ interference in the e^+e^- final state is expected. At this energy we propose to perform high statistics measurements of dielectron production. The expected count rate for this channel in quasi-free πp reactions on carbon nuclei in the PE target is given in Table 3.1 for the dielectron invariant mass $M_{ee} > 150$ MeV/c^2, where signal is not contaminated by π^0 Dalitz decays, separately noted in brackets. In this energy range, the dilepton production can be studied in a large invariant mass range (up to 800 MeV/c^2), which will allow to study the transition between "point-like" electromagnetic couplings governed by the real photon-couplings to "VDM-like" couplings governed by the vector-meson couplings. Several baryonic resonances will contribute (Δ(1620), Δ(1700), N(1650), N(1675), N(1630), N(1710), N(1720),...). The interpretation of the dielectron channels will rely on the extraction of the couplings in the hadronic channels measured in the same experiment, as explained in the next section.

The ultimate goal is to extract etFF of the baryonic resonances or equivalently helicity amplitudes $A_{3/2}$, $A_{1/2}$, $S_{1/2}$ as a function of q^2 (for time-like photons the invariant mass of dielectrons) (see [92]). Such extraction would allow for the first time to extend the evolution of these functions measured in electro-scattering experiments into the time like region [93]. The helicity amplitudes can be extracted from the spin density matrix elements which can be derived from a measurement of triple differential cross sections, as shown in [89]. The amplitude for the unpolarized $\pi^-+p \to ne^+e^-$ reaction for a given momentum k and emission angle of the virtual photon ($z = cos\theta_{CM}$) and the angles (θ,ϕ) of the electron in the virtual γ rest frame is given by:

$$\mid \mathcal{A} \mid^2 = 4k^2[2\rho_{00}(1-cos^2\theta)+2\rho_{11}(1+cos^2\theta)+2\sqrt{2}k^2 sin(2\theta)cos\phi Re\rho_{10}+2sin^2\theta Re\rho_{1-1}cos(2\phi)] \tag{3.1}$$

A method to extract spin density matrix elements from a fit to experimental data has been developed based on the maximum likelihood method. Figure 3.1 shows the spin density matrix elements extracted from the quasi-free $\pi^-+p \to e^+e^-$ data collected in 2014 in three bins of virtual photon angle. The significant deviation of the ρ_{11} elements from 0.5 and the non zero value of ρ_{10} clearly demonstrate contributions of virtual photons with longitudinal polarization, which is already a significant information. In addition, the comparison to predictions of the Lagrangian model of [89] for the N(1520) contribution, where a VDM

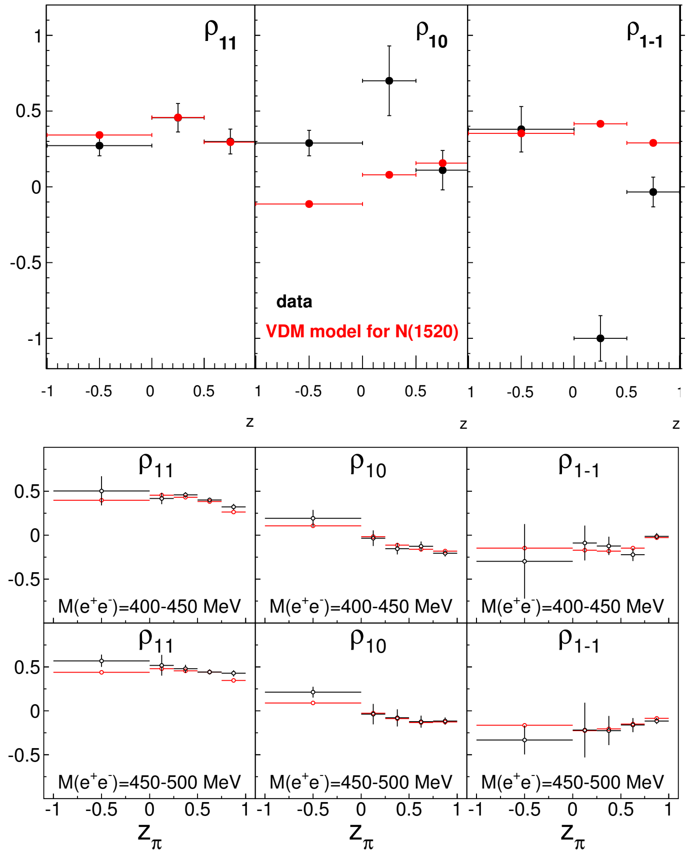

Figure 3.1: Top: Comparison of spin density matrix elements ρ_{11} , ρ_{10} , ρ_{1-1} extracted from the data (black dots) and from the model [89] as a function of z = cos (θ_{CM}) for dilepton masses $M_{ee} > 400$ MeV$/c^2$. Right: Projected precision on spin density matrix elements for 10^4 events. The black points are obtained in the full solid angle and the red points after reconstruction within the HADES acceptance.

form factor model is shown to demonstrate the capacity of already taken data to verify models, has been done. However, due to the variation of these coefficients as a function of the angle bin, it is clear that a better precision is needed to extract detailed information on the electromagnetic structure of the baryon transition. Furthermore, to identify nuclear effects a contribution from reactions of pions on carbon has to be independently measured with a nuclear target. Such information has also to be coupled to the Partial Wave Analysis of hadronic channels which allows to extract the amplitudes of the different resonant and non-resonant contributions.

Simulations show that a total statistics of 10^4 events in the $\pi^- + p \rightarrow ne^+e^-$ reaction is needed to extract the elements with precision of few percent in the forward direction, the backward region being affected by the HADES acceptance. The right part of Fig. 3.1 shows simulation results based on Eq. 3.1. For these estimates, we use a form factor model of the N-N(1520) transition with transverse (electric and magnetic) contributions as measured in photon-induced reactions ($\gamma n \rightarrow \pi^0 n$) and an additional small arbitrary longitudinal part (private communication A. Sarantsev). The evolution of the spin density matrix elements as a function of the virtual photon emission angle ($z = cos\theta$) for the two indicated invariant mass bins is shown. The black points show results obtained in the full solid angle and the red points within the HADES acceptance. In the forward region, both values agrees well, hence allowing for the extraction of the spin density matrix elements with good precision. To obtain similar statistical errors, we propose a measurement campaign with a total of 71 shifts, with 41 shifts on the PE target and 30 shifts on carbon. The count rate estimates (see Table 3.1) are based on the statistics collected in the first experiment. Furthermore, it was found that the contribution from the quasi-free reactions on carbon in the missing mass window is around a factor a 2 larger than from $\pi^{-}+p$ reactions. We assume an increase of the electron pair identification efficiency due to the new photon detector by a factor of 2 and an increase of the cross section by a factor of 2 with respect to the measurement at 0.7 GeV/c. It has to be noted that the measurements on the carbon target are needed to control nuclear effects in quasi-free reactions. The total statistics expected from PE and C targets is more than $4.6 \cdot 10^4$ events with $M_{ee} > M_{\pi^0}$. The measurements on carbon will also provide enough statistics for dielectron measurements off carbon, and even better statistics for meson production as discussed in section 3.2.4.

Similar studies can be performed in the fourth resonance region ($\sqrt{s} \sim 1.9$ GeV/c) using the same number of shifts in combination with measurements of the $\Lambda(1405)$ and kaonic states, as presented in the section 1.2.3. In this case, the proton beam at 3.5 GeV is more favorable for the production of the secondary pion beam.

3.2.2 Hadronic final states

In the region of mass around 1.7 GeV/c^2, the properties of baryonic resonances (masses, widths and decay branching ratios) are mainly known from elastic pion-nucleon scattering and electro-scattering experiments. However, analysis often suffers from lack of precise data on inelastic pion-nucleon channels. In addition, some states are not clearly established (*e.g.* $\Delta(1750)$). Our measurements will provide the missing data, and in particular precise differential distributions in several hadronic channels, and will therefore have a strong impact in the field of baryon spectroscopy. In addition to dielectrons, many hadronic channels like the already mentioned 2 π but also $K\Lambda$, $K\Sigma$, ηn and light vector meson production will be studied simultaneously to control resonance-meson couplings. The new HADES measurements will complement the precise data obtained from photon and electron-scattering experiments and will allow for a better understanding of the resonance mass spectrum and their decays. In this context one should underline the importance of precise two pion data for the understanding of the N^* spectrum around 2 GeV/c^2 where several new states were established via sequential $N^* \to \pi N^*(\Delta^*) \to N\pi\pi$ in channels with two neutral pions [94].

New HADES data for two and three pion production and new CLAS results on similar channels measured in electron scattering will scrutinize ω and ρ production above $\sqrt{s} > 1.7$ GeV and allow for a precise understanding of vector meson-resonance couplings. A combined PWA analysis of all available data, as demonstrated with already taken data, will allow to separate contributions from various resonances to the vector meson production and will be used to test the validity of VDM in the e^+e^- production. As already pointed out, understanding these couplings is also essential for the calculations of in-medium spectral functions and the interpretation of dielectron data from heavy ion collisions. In this context, an important intermediate step consists in studying cold matter effects via $\pi + A$ reactions which provide an excellent opportunity due to recoilless kinematics. Furthermore, absorption and re-scattering of long-lived mesons like for example kaons and ϕ mesons can be studied on nuclear targets with unprecedented statistics.

The count estimates for pionic channels are based on known cross sections (given in the second raw of Table 3.1) and a conservative beam intensity taken a factor 4 higher as compared to the first experiment. At 1.1 GeV/c, the pion yield produced in ^{14}N+Be reaction at 2 A GeV is a factor of two higher than at 0.7 GeV/c. In addition, a factor 2 on the primary beam intensity should easily be available, thanks to expected improvements of shielding and beam extraction efficiencies. An overall efficiency of 25% has been assumed, taking into account the accelerator duty factor, the acquisition dead-time and the rate of beam interruptions, based on the previous experiment.

The efficiency for pionic channels does not depend much on the center-of-mass energies and was taken as 14%, as measured in the previous experiment. For the neutral hyperon production we assume the reconstruction of $K_s^0 \rightarrow \pi^+\pi^-$ only and the separation of the Λ/Σ^0 via the missing mass technique. The missing mass resolution of the two-pion final state was measured to be $\sigma = 11$ MeV/c^2, hence sufficient to resolve the hyperon states. The efficiency for K_S^0 reconstruction has been estimated to be 4%, based on full scale GEANT simulations which were validated to previous reconstructions of kaons in HADES experiments. Based on previous HADES measurements, we use an efficiency of 13% for the Σ^+K^- channel. The η reconstruction efficiency of 8% has been obtained using simulations including the ECAL.

Table 3.1 below presents count rate estimates for one shift (8 hours) of beam with an intensity $I_\pi = 4 \times 10^5 \pi^-/s$ on the PE target, and π^-+p reactions at five values of $\sqrt{s}$ centered around $\sqrt{s} = 1.74$ GeV ($p = 1.12$ GeV).

$\sqrt{s}$	$\pi^+\pi^-n$	$\pi^0\pi^-p$	$K^0\Lambda$	Σ^0K^0	Σ^+K^-	ηn	e^+e^-n ($M_{ee} >$ 150 MeV/c^2)
σ	$10mb$	$7mb$	$0.6-0.3mb$	$0.25mb$	$0.2mb$	$1.25mb$	
1.68	$1.6 \cdot 10^6$	$1.1 \cdot 10^6$	$1.3 \cdot 10^4$	$0.6 \cdot 10^4$	$3 \cdot 10^4$	$8.0 \cdot 10^4$	220 (440)
1.71	$1.6 \cdot 10^6$	$1.1 \cdot 10^6$	$1.3 \cdot 10^4$	$0.6 \cdot 10^4$	$3 \cdot 10^4$	$8.0 \cdot 10^4$	
1.74	$1.6 \cdot 10^6$	$1.1 \cdot 10^6$	$1.3 \cdot 10^4$	$0.6 \cdot 10^4$	$3 \cdot 10^4$	$8.0 \cdot 10^4$	
1.77	$1.6 \cdot 10^6$	$1.1 \cdot 10^6$	$1.0 \cdot 10^4$	$0.6 \cdot 10^4$	$3 \cdot 10^4$	$8.0 \cdot 10^4$	
1.8	$1.6 \cdot 10^6$	$1.1 \cdot 10^6$	$0.7 \cdot 10^4$	$0.6 \cdot 10^4$	$3 \cdot 10^4$	$8.0 \cdot 10^4$	

Table 3.1: Count rate estimates for one shift for different channels of the π^-+p reaction at five different energies.

The PWA of the two pion channels require around 10^5 events. However, for the two particle final states as hyperon or η one needs less statistics. In order to significantly improve the experimental situation, where differences of a factor 2 between various measurements can be found (see [95]), we propose new measurements of differential distributions, with a statistical precision in each bin of a few percent. For example, with ten bins in angle, a total statistics of around 10^4 is required. For the most demanding measurement of the neutral hyperon channels, this can be obtained for each energy point with two shifts with PE target and two thirds of a shift on the carbon target.

3.2.3 Λ(1405) and kaonic bound states

Theoretical models constrained by K^--nucleon scattering data and kaonic hydrogen measurements do describe the $\Lambda(1405)$ as emerging naturally from the coupling of two poles: a rather narrow K^-p and a rather broad $\pi\Sigma$ pole [96, 97, 98, 99]. Experimentally, one observes that the $\Lambda(1405)$ spectral shape varies depending on the initial state [100, 101, 102, 103, 22]. In particular, HADES measured the reaction $p + p \rightarrow \Lambda(1405) + K^+ + p$ with subsequent

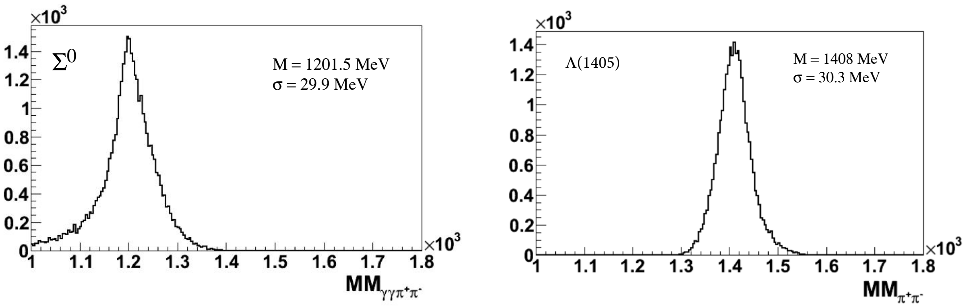

Figure 3.2: Left panel: Σ^0 signal reconstructed from the two pions and two photons missing mass from the reaction $\pi^- + p \to \Lambda(1405)(\Sigma^0 + \pi^0(\gamma\gamma)) + K^0_S(\to \pi^+ + \pi^-)$. Right: resulting $\Lambda(1405)$ spectral shape for the same reaction. See text for details.

decays into charged final states $\Lambda(1405) \to \Sigma^\pm\pi^\mp$ and found a shift of the $\Lambda(1405)$ spectral shape of about 25 MeV towards lower masses with respect to the nominal value [22]. This shift is different from the spectral shapes measured in kaon- and photon-induced reactions and new measurements with in-flight and stopped kaon beams are planned at the JPARC facility in the next years. Since from a theoretical point of view a coherent explanation of the measured $\Lambda(1405)$ spectral shape is missing, it would be extremely important to measure pion-induced reactions with good statistics, since the old data do not provide an accurate measurement. For this reason we propose to employ pion beams with 2 GeV kinetic energy to measure the reaction $\pi^- + p \to \Lambda(1405) + K^0$ and investigate the decays $\Lambda(1405) \to (\Sigma\pi)^0$. The availability of secondary pion beams and the excellent reconstruction capability of the HADES spectrometer offer a unique possibility to perform this measurement in an accurate way for the first time. The new electromagnetic calorimeter that will be implemented within HADES, will also allow for the exclusive measurements of the $\Sigma^0\pi^0$ decay channel, that was not possible up to now.

A full scale simulation of the reconstruction of the $\Lambda(1405)$ has been carried out employing also the electromagnetic calorimeter for the photons and π^0 reconstruction. The K^0 is reconstructed via its weak decay into $\pi^+\pi^-$ pairs. The three decays $\Lambda(1405) \to \Sigma^0\pi^0/\Sigma^+\pi^-/\Sigma^-\pi^+$ can be used to reconstruct the resonance but the neutral channel presents the advantage of being free from the background by the broad $\Sigma(1385)$ resonance that decays into the charged $\pi\Sigma$ final states. Figure 3.2 shows the results for one of the many analysis strategies that have been investigated where the K^0_S is reconstructed together with the 2 γ from the π^0 decay. The left panel of Fig. 3.2 shows the obtained Σ^0 signal after the K^0_S selection and the refit of the π^0 from its decay into two photons detected by the ECAL. A resolution of about 30 MeV/c^2 is obtained for the Σ^0 missing mass. The right panel of Fig. 3.2 shows the resulting missing mass to the K^0_S after the Σ^0 selection that corresponds to the $\Lambda(1405)$ spectral shape.

Table 3.2 shows the rates per day for the different decay channels obtained considering a pion beam intensity of 5×10^5 π^-/spill and a spill length of 4 sec for a beam momentum of 2 GeV/c, a PE target with 2.2% interaction length and a duty factor of 0.25. One can see that two out of four measurements will be enough to collect unprecedented rich statistics.

Additionally, π-induced reactions on light targets can also be employed to search for kaonic bound states. Due to the attractive K^-nucleon interaction, a bound K^-pp nuclear system can be formed and the determination of its binding energy could provide quan-

$\pi^- + p \to$	Reconstruction	resolution	Total Eff.	Rate/day
$\Lambda(1405)(\Sigma^0 + \pi^0) + K^0_S$	K^0_S,π^0 +π^0 refit	30.3 MeV	0.3 %	$2.4 \cdot 10^3$
$\Lambda(1405)(\Sigma^0 + \pi^0) + K^0_S$	K^0_S and $\Sigma^0 \to \Lambda + \gamma$ reco.	42 MeV	0.09 %	950
$\Lambda(1405)(\Sigma^+ + \pi^-) + K^0_S$	K^0_S and π^- reco.	33 MeV	1.7 %	$1.7 \cdot 10^4$
$\Lambda(1405)(\Sigma^+ + \pi^-) + K^0_S$	$\Sigma^+ \to p + \pi^0$, π^-+ π^0 refit	32 MeV	0.12%	$1.8 \cdot 10^3$
$\Lambda(1405)(\Sigma^- + \pi^+) + K^0_S$	K^0_S, π^+, π^- + refit n	27 MeV	0.5%	$4.7 \cdot 10^3$

Table 3.2: Expected count rates per day for the measurement of the $\Lambda(1405)$ spectral shape in π^-+PE reactions at a beam momentum of 2 GeV/c.

titative information about the interaction. Several experiments have been carried out to search for such bound states, but the experimental signature is not solid at all. From a theoretical point of view, these bound states are predicted to exist [104, 105, 106, 107, 108, 109, 110] but a broad range of binding energies (20 MeV<E$_{binding}$<100 MeV) and widths (40 MeV<Γ<100 MeV) under debate.

Recently the E27 experiment at JPARC exploited the reaction $\pi^+ + d \to K^+ + X$ to search for kaonic bound states and a significant excess is currently discussed [111]. A similar measurement can be performed by HADES for pion momenta larger than 1.7 GeV/c.

3.2.4 Vector meson production off nuclei

While medium modifications are expected to be stronger in a hot and dense medium as produced in heavy ion collisions, sizeable effects are already predicted in cold matter and can be explored using photon, proton or pion beams. One advantage consists in the fact that the system does not undergo such a large density and temperature evolution as in heavy ion collisions, which makes the interpretation of the results easier. Cold nuclear matter has been studied up to now mostly using photon and proton beams . In particular, the HADES collaboration achieved a breakthrough in this field thanks to its capability to measure the production of dielectrons at low p_T [20]. This feature is indeed essential to pin down in medium decays of the vector mesons. The kinematics of the π^-+A reaction presents the additional advantage of a small momentum of the produced particles (so-called nearly recoilless kinematics), which hence increases the number of decays inside the medium. Indeed, as can be seen in Fig. 3.3, omegas are produced in the pion beam experiment at 1.12 GeV/c, with a momentum lower than 0.6 GeV/c, *i.e.* much lower momenta than in the proton beam experiment at 3.5 GeV that we previously measured.

As described above, the measurements on the carbon target will be available from the proposed experiment, since they are needed to extract events corresponding to the $\pi^- + p$ reaction from the measurement on the polyethylene target.

Several predictions for e^+e^- production in π^-+A reactions exist in the literature (see *e.g.* [112, 113]) or have been developed recently using HSD or GiBUU transport calculations (private communication E. Bratkovskaya, J. Weil). The latter show very significant distortions of the dielectron invariant mass in π^-+Pb or π^-+Au if in-medium spectral functions of the ρ are included, but already significant effects can be seen in the case of π^-+C. For measurements above the omega meson threshold ($\sqrt{s_{NN}} = 1.72$ GeV/c), absorption of the omega can be measured, using the ratio to the yield measured on the proton, as already studied in the p+Nb reaction 1.1.1.

Another interesting aspect of the e^+e^- production in a light nucleus is related to the $\rho-\omega$ interference. As mentioned in section 3.2.1, significant interferences between the ρ and ω contributions are predicted for the $\pi^- p \to ne^+e^-$ reaction. These effects should vanish

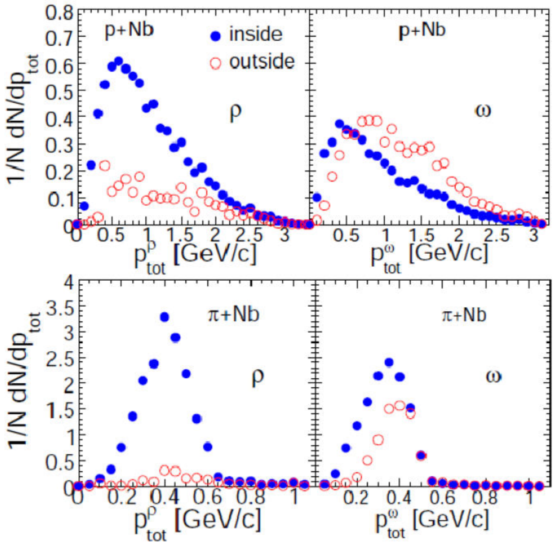

Figure 3.3: Laboratory momentum distributions for inside and outside decay of ρ's (left) and ω's (right) for pNb reactions at 3.5 GeV incident energy (upper panels) and for πNb reactions at 1.17 GeV (lower panels).

in nuclear matter, but (according to private communication Gy. Wolf), be still significant in a carbon nucleus. Our data on proton and carbon will help to quantify this de-coherence process.

With 34 shifts of beam on the carbon target, as needed to get sufficient precision for the study of the π^-+p reaction in the subtraction procedure, we can expect about $1.9 \cdot 10^4$ e^+e^- pairs coming from the ρ and about the same amount from the ω. Such a collection of events will allow for a precise determination of the differential cross section as a function of the e^+e^- invariant mass and a detailed investigation of de-coherence and ω absorption effects.

We will also provide differential and total cross sections in π^-+C for many mesons (pions, ω, η, K, ϕ, ...). Such data indeed do not exist in this energy range and are important to test transport models and cascade models, which are used *e.g.* for GEANT4 simulations.

3.3 Ag+Ag at 1.65 A GeV

Simulations were performed with events generated with UrQMD for the 44% most central collisions (*i.e.* $b \leq 8\,\mathrm{fm}$). Into these events enriched rare signals were embedded after simulating their phase space distribution by means of the PLUTO event generator. Respective down scale factors were afterwards applied in the post analysis. These events were then processed with GEANT including the following (detector) systems: a 15-fold segmented *Ag*-target, magnet, the new HADES RICH (*cf.* s. 2.2.2), four planes of MDC, the TOF, the RPC and the new ECAL (*cf.* s. 2.2.1). The digitizers (which simulate the detector response based on the GEANT output) of the two new detector systems were tuned based on prototype measurements, while the parameter set derived for the Au+Au data (2012 beam time) was used for all other detectors. The so generated events were then reconstructed using the standard analysis package HYDRA.

3.3.1 Dielectron observables

In the dielectron channel, we will focus on the properties of the low- and intermediate-mass excess as well as on the spectroscopy of light (ω, ϕ) vector mesons. The feasibility study was performed with 10^7 UrQMD events including e^+e^- final states, as well as the necessary background that influences their reconstruction efficiency, from (a) π^0- and (b) η-Dalitz decays, (c) ω and (d) ϕ simulated in Pluto as originating from a thermal fireball and finally (e) in-medium radiation via ρ^0's produced assuming spectral functions with thermal parameters obtained with the coarse-graining approach [43]. In total 10^7 e^+e^- pairs, each from decays of the three vector mesons, were embedded. To enhance the statistics of the signal spectrum, for the (f) ω-Dalitz channel (10^7 pairs) and a larger sample of in-medium (g) ρ^0 (10^8 pairs), phase space distributions were simulated and properly scaled using the reconstruction efficiencies as a function of dielectron invariant mass from the full simulation above. The sources (c)-(g) were normalized based on measured multiplicities according to [15] and [43], scaled with $(A_{\text{part}}(\text{AgAg})/A_{\text{part}}(\text{ArKCl}))^{1.4}$ to account for the different system sizes in the given centrality classes. Combinatorial background was estimated from same-event like-sign pairs of leptons from (a) and (b) in $M_{ee} < 0.4$ GeV$/c^2$ and from event mixing of the same leptons for higher invariant masses. For the particle identification, lepton candidates were selected by track quality criteria as well as the conditions $p > 100$ MeV$/c$, $\beta > 0.9$ and matching of the track to a RICH ring allowing declinations of $\theta \leq 1°$. All other analysis steps followed those applied in the analysis of the 2016 Au+Au data.

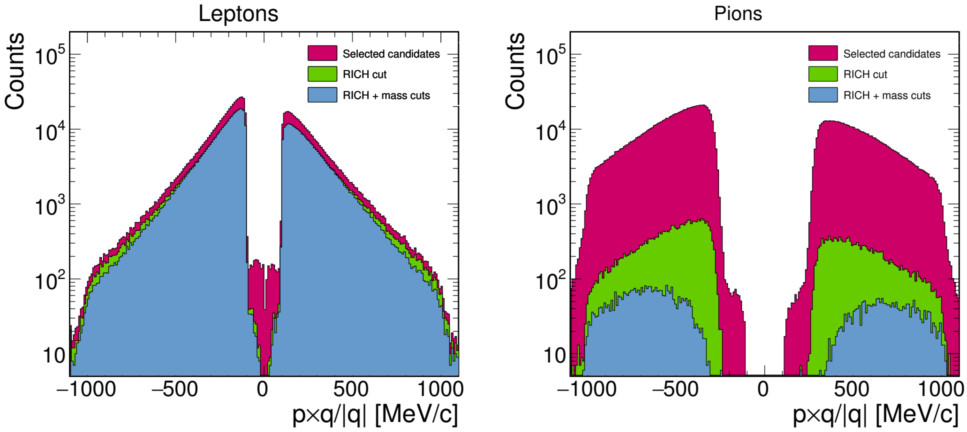

Figure 3.4: Left: Momentum distributions of leptons after subsequent lepton identification cuts. Magenta: selected lepton candidates, green area: after $\delta\theta \leq 1°$ cut on spacial matching between RICH ring and track, blue area: after an additional velocity versus momentum graphical cut. Right: same for charged pions.

Figure 3.4 shows momentum distributions of reconstructed lepton candidates after each identification step separately for true leptons (left panel) and misidentified pions (right panel). The strong discrimination power of the lepton identification cuts is demonstrated by the strong suppression of fake electrons (pions) while preserving most of the true electrons (Leptons).

The invariant-mass distributions of electron pairs, including full event reconstruction and electron identification after applying background rejection cuts, together with a cocktail of all signal sources is shown in the left panel of Fig. 3.5. The main source of random combinations is a mix of incompletely detected pairs from π^0-Dalitz decays or external conversion of photons in the detector (target) material. In the analysis, all electron tracks forming unlike-sign pairs with an opening angle $\alpha \leq 9°$ are rejected and not used for further pairing. The resulting ratio of signal to combinatorial background (S/B) is shown in the right panel of Fig. 3.5. At this level of background rejection the ω and ϕ signals are outshone by the combinatorial background. The S/B ratio at the ω and ϕ pole mass

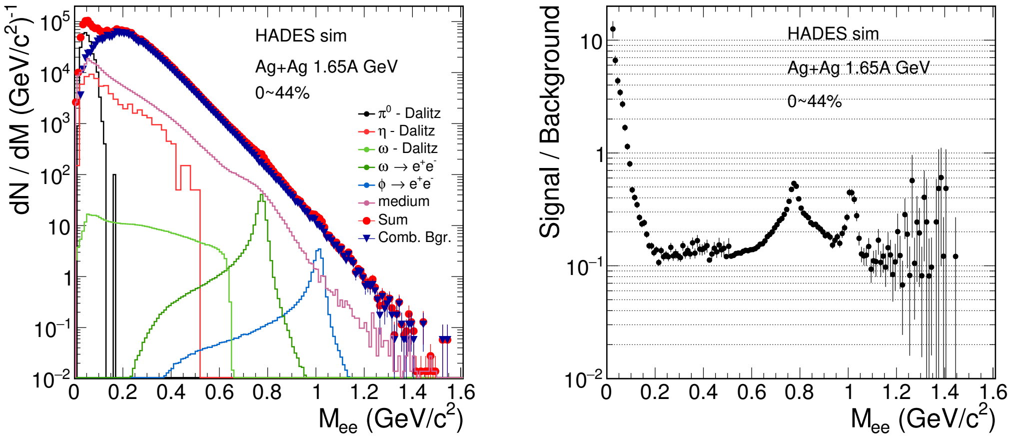

Figure 3.5: Left: Dielectron invariant mass distribution reconstructed in Ag+Ag collisions at 1.65 A GeV. Sources of e^+e^- are shown in different colors. Right: Signal-to-combinatorial background ratio as a function of invariant mass.

amounts to 0.5 at a total signal reconstruction efficiency of 50%. For the invariant mass region $0.15 \leq M_{ee}/(\mathrm{MeV}/c^2) \leq 0.55$ an integrated S/B of (1/10) was obtained. Also for M_{ee} above 1 GeV/c^2 the signal-to-background ratio is of the order of 10% and will allow for a significant signal extraction.

Table 3.3 shows count-rate estimates for the number of reconstructed signal pairs from different sources. The multiplicities of π^0-Dalitz and η-Dalitz pairs are based on meson multiplicities computed by the UrQMD model. The continuum pairs are based on the coarse-grained transport model calculations for Ar+KCl assuming thermal emission from the bulk. Their rates were further scaled to account system size dependence and energy dependence.

M_{ee} range	<0.15 GeV/c^2	0.15-0.45 GeV/c^2	0.3-0.7 GeV/c^2	>1 GeV/c^2
Rate [84 shifts]	$2.89 \cdot 10^6$	$7.1 \cdot 10^5$	$2.1 \cdot 10^5$	107

Mesons	$\pi^0 \to \gamma e^+e^-$	$\eta \to \gamma e^+e^-$	$\omega \to e^+e^-$	$\phi \to e^+e^-$
Rate [84 shifts]	$1.5 \cdot 10^6$	$7.32 \cdot 10^5$	179	62

Table 3.3: Pair rates of vector-meson direct decays and e^+e^- continuum recorded per 4 weeks of the beam on target (selecting 44% of most central Ag+Ag collisions). This corresponds to $5 \cdot 10^9$ events (collected during 84 shifts) assuming beam intensity of 1.5×10^6 ions per second, 1.5% interaction length target and 10 kHz trigger rate.

We have assumed a beam intensity of 1.5×10^6 ions per second and a 1.5% interaction target. Based on our experience in the Au+Au run and assuming that the LVL1 trigger (based on charged hit multiplicity in ToF and RPC) selects only 44% of the total cross section and gives 10 kHz accepted LVL1 trigger rate and 10^6 events per hour on disc (this assumption includes a dead time 52% and a duty factor of 61%).

In Fig. 3.6 the cocktail described above is compared to the HSD [45] calculation for Ag+Ag at 1.65 A GeV in the mass range, where the in-medium radiation plays a dominant role. The error bars on the cocktail were computed as statistical uncertainty of signal after combinatorial background subtraction in the case that the statistics will be sufficient to produce 10^5 e^+e^- pairs from in-medium ρ (*i.e.* 5×10^9 events). Clearly, this statistics would allow to discriminate between the two model with high significance.

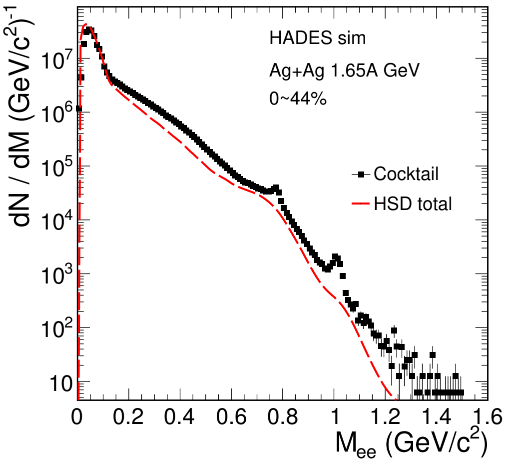

Figure 3.6: Comparison of the invariant mass spectrum of the cocktail including in-medium ρ from coarse-grained transport model calculations (black squares) to the one from the HSD model (dashed red curve). The statistics corresponds to 84 shifts.

3.3.2 (Multi) strangeness production

The main goals are to search for multi-strange baryons in connection to our findings in p+Nb and Ar+KCl, and to extend the excitation function of particles containing (multi) strangeness. Indeed, the unexpected high cascade yield is by now not explained theoretically and calls for more data [27]. This strangeness study will include ϕ meson production via the K^+K^- decay channel, kaon production characteristics, $\Lambda(1115)$, $\Sigma(1385)$ and $\Xi(1321)$ strange baryon production, and HBT correlations.
The presence of the Ξ^- excess in Ar+KCl but also in cold nuclear matter [28] (see for details Section 1.1.2) calls for a systematic investigation of the system size dependence of this excess. Therefore, an additional measurement in a heavier system than Ar+KCl is necessary. Due to the lower energy in combination with the huge combinatoric in Au+Au collisions at 1.23 A GeV the reconstruction of the Ξ^- was not successful until now.

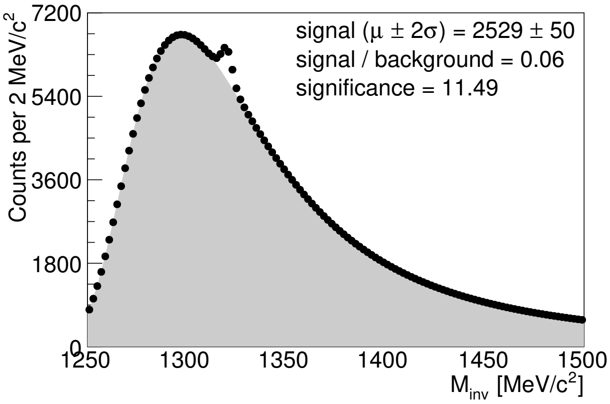

Figure 3.7: Full scale simulation of Λ+π^- candidates invariant mass distribution after using the Ξ^- decay topology for background suppression, see text for details.

Ag+Ag collisions at 1.65 A GeV have been identified as the ideal environment to investigate Ξ^- production inside a heavy collision system. For the estimate of the Ξ^- yield we assume that the small difference in kinetic beam energy of 0.09 GeV between the measured Ar+KCl and the Ag+Ag systems is compensated by the stronger than linear increase with the mean number of participants observed for strange hadron yields. Hence, we scale the Ξ^- yield of 2×10^{-4} measured in Ar+KCl by a factor 3 in order to take the larger number of mean participants per reaction into account. Subsequently, we generated thermally

	Rates/dy	F_{ACC}	F_{DAQ}	F_{Apart}	Rates/dy	Rate [84 shifts]
K^+	$1.1 \cdot 10^4$	2	4	3	$2.7 \cdot 10^5$	$7.6 \cdot 10^6$
K^-	270	2	4	3	$6.5 \cdot 10^3$	$1.8 \cdot 10^5$
K_s^0	$2.3 \cdot 10^3$	1	4	3	$2.72 \cdot 10^4$	$6.36 \cdot 10^5$
Λ	$2.3 \cdot 10^3$	1	4	3	$2.72 \cdot 10^4$	$6.36 \cdot 10^5$
ϕ	7	1	4	3	84	$2.4 \cdot 10^3$

Table 3.4: Gain factors and estimated count rates per day (and per 4 weeks of beam on target) for various hadrons carrying strangeness, see text for details.

distributed Ξ^- hyperons with the given rate and embedded them into simulated UrQMD Ag+Ag events. The data were transported through a full scale GEANT3 simulation and reconstruction similar as for real data. We have analyzed simulated data corresponding to 5×10^9 events. The resulting Λ+π^- invariant mass distribution, after using the Ξ^- decay topology for background suppression, is presented in Fig. 3.7. A clear Ξ^- signal is visible above the background with the significance of 11.5. The wide rapidity coverage of 0.3 to 1.2, in combination with the about $2.5 \cdot 10^3$ reconstructed Ξ^-, allows for a multi-differential analysis in rapidity and transverse momentum, for the first time.

The count rates of the other hadrons carrying strangeness are also estimated based on the number of reconstructed counts in Ar+KCl collisions at 1.76 A GeV. For this estimate we assume again that the slight difference in kinetic beam energy is compensated by the stronger than linear increase with the mean number of participants observed for strange particles. The estimated gain due to the geometrical acceptance F_{ACC}, the data acquisition F_{DAQ} and the larger collision system F_{Apart} are taken into account by multiplicative factors. Due to an older time-of-flight wall at low polar angles charged kaons have only been reconstructed in the region between polar angles between 45° and 85° for Ar+KCl collisions. The installation of the RPC detector in 2010 allows for identification of charged kaons also at lower polar angles, hence we assume a $F_{ACC} = 2$ in case of charged kaons. Compared to Ar+KCl we assume a F_{DAQ}=4 times faster data acquisition and similar as for the Ξ^- a factor $F_{Apart} = 3$ is estimated to take into account the larger collision system.

The results are summarized in Table 3.4.
This gain in statistic will enable us to investigate the flow distributions even of the rare hadrons in great detail which will help to increase our understanding of the production and propagation of strangeness further.

3.3.3 $\phi \to e^+e^-$ vs. $\phi \to K^+K^-$

Contrary to the ρ meson with a lifetime of 1.3 fm/c, much smaller than the lifetime of the fireball (7-10 fm), the ϕ has a lifetime of 44 fm/c. Therefore in-medium effects on the mass or width might be difficult to isolate experimentally, and might only appear at very low p_T. A possible way of tracing down those modifications is the comparison of the particle yields and spectra in the dilepton and in the kaon channel: since the ϕ is below the free N+N threshold for the $\phi \to K^+K^-$ channel, even a small change in its spectral properties should lead to a significant difference in the two channels. Any differences in two channels could also be attributed to final state effects related to in-medium kaon absorption or re-scattering.

3.3.4 Thermal particle production

A detailed comparison of the Ar+KCl reactions at 1.76 A GeV with the statistical model fit has been shown in Section 1.1.3. A similar investigation in case of Au+Au collisions at 1.23 A GeV kinetic beam energy revealed that the inclusion of rarely produced hadron species, which have not been measured before at such low energies, drives statistical model fits to higher values of the parameters T and μ_B [114]. In order to confirm this trend, a measurement at higher energies, where the cross sections of these hadron species in Ag+Ag collisions at 1.65 A GeV are significantly increased and hence the statistical error bars are reduced, is mandatory.

3.3.5 Correlations and fluctuations

With an expected statistics of $5 \cdot 10^9$ triggered Ag+Ag events, the acquired data sample will allow to investigate the net proton number, as well as net charge fluctuations up to the 5^{th}-order cumulant at least and probably even up to 6^{th} order. This will be the first data set world-wide giving access to the cumulant ratios κ_5/κ_2 and κ_6/κ_2, expected to be particularly sensitive to features of the QCD phase diagram (see *e.g.* [115]), with sufficient statistical precision. Instrumental effects, due to finite detector acceptance and efficiency as well as to volume fluctuations, will have to be controlled appropriately of course. The aim to study these observables in the energy regime of SIS18 is to provide complementary information with respect to the beam energy scans done (and to be done) at RHIC in both, the collider and the fixed-target modes. We will indeed be able to extend the systematic investigation of the susceptibilities of the QCD phase-diagram to the region of highest baryonchemical potential accessible in heavy-ion collisions.

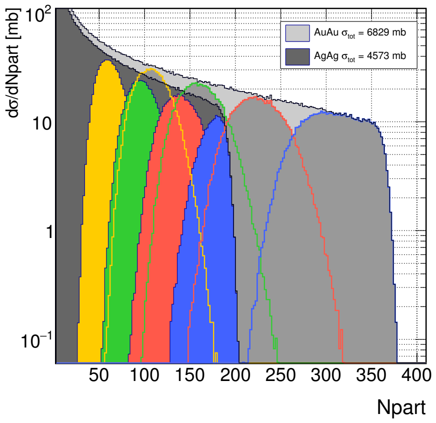

Figure 3.8: N_{part} distributions for Ag+Ag collisions at 1.65 A GeV and Au+Au collisions at 1.23 A GeV as calculated with a Glauber MC model. The different centrality classes, each corresponding to 10 % of the total cross section and selected via the hit multiplicity seen by the TOF and RPC detectors, are shown in color.

The proposed Ag+Ag data set will also allow to extend the flow studies currently being performed for Au+Au (see chapter 1). A systematic measurement of flow harmonics up to order three (*i.e.* v_1, v_2 and v_3) and their fluctuations will be possible for identified particles, providing important information on the properties of the dense baryonic matter produced in these collisions. An important aspect of the Ag+Ag collisions system is that it has a different surface-to-volume ratio than the larger Au+Au system and thus allows to study geometrical aspects of collective phenomena from a different perspective.

An important prerequisite for the interpretation of the fluctuation and flow measurements is a good understanding of the size and shape of the involved reaction volume. We address this points with the help of a Glauber MC model. Figure 3.8 shows the N_{part} distributions for the four most central centrality classes (each 10 % of the total cross section) in Ag+Ag and Au+Au collisions, as they can be selected via the hit multiplicity in the TOF and RPC detectors. A good separation of the event classes can be achieved also for the smaller Ag+Ag system.

3.4 p+p at 4.5 GeV

Measurements of hadron production off cold nuclear matter in p+A collisons provide an important direct reference for heavy-ion collisions and allow for studies of several important elementary processes. They can also serve in a similar way as measurements in π^-+A reactions as a test bed for microscopic transport theory. HADES has already studied p+p and p+Nb collisions at 3.5 GeV. Yet, many of the interesting observations made so far, like Ξ^-, $\Lambda(1405)$, ω production, suffer from poor statistical significance or call for further multi-differential analyses. Also, a systematic analysis of the contribution of resonances to different final states, including the effect of interference among broad resonances carried out for the p+p at 3.5 GeV and 1.25 GeV data sample, should be repeated for other beam energies to establish a solid reference.

Particle identification in the 2008 run was limited since no fast start detector was available at the time, but meanwhile HADES has developed start detectors based on monocrystalline CVD diamond which combine high rate-capability with excellent time resolution for minimum ionizing particles. Also, the data acquisition rate has been improved, which currently allows for high statistics runs. Further gains are expected in dielectron reconstruction due to the improved RICH read-out. A high statistics p+A run would thus enable very important studies of ω and ϕ production and propagation, in both the hadronic and the leptonic final states, dielectron production in the intermediate mass range (>1 GeV/c^2), strange meson and multi-strange baryon production. Runs with higher proton beam energies (maximal SIS18 energy is 4.5 GeV) will open the possibility of detailed studies of the excitation function of multi-strange baryon production, excited hyperon states and the first measurements of their electromagnetic Dalitz decays. Particularly, a high statistics p+p run at the maximum energy provided by the SIS18 accelerator will provide the missing reference measurement for high-mass resonances contributing to the measured final states and, among other things, for the Ξ^- production in elementary reactions. The latter will help to answer the important question, whether the high rates observed in p+Nb and Ar+KCl are related to hadronic many-body effects or not. Furthermore, such measurements will provide an important reference for the future CBM program at FAIR and are also complementary to the planned studies of hyperon production in proton-antiproton collisions with PANDA.

3.4.1 Inclusive dielectron observables

The following feasibility study was done in nearly the same way as for Ag+Ag collisions at $1.65\,A$ GeV, discussed in section 3.3.1. 10^8 UrQMD events were used to generate π^0 and η contributions as well as the combinatorial background. The multiplicity of $\Delta(1232)$ is based on our measurements [19] corrected for the respective beam energy dependence. For the Dalitz decay $\Delta \to N\gamma^* \to Ne^+e^-$, the mass-dependence of the width is calculated from the matrix element extracted from Krivoruchenko *et al.* [92]. The ω multiplicity is based on our measurements [19] corrected for the respective beam energy. The multiplicity of ϕ is based on world data. The resulting invariant mass distribution of the cocktail and the ratio of signal to combinatorial background are shown in Fig. 3.9. Please not that the contribution from high mass resonances decaying to ρN is not included to the cocktail.

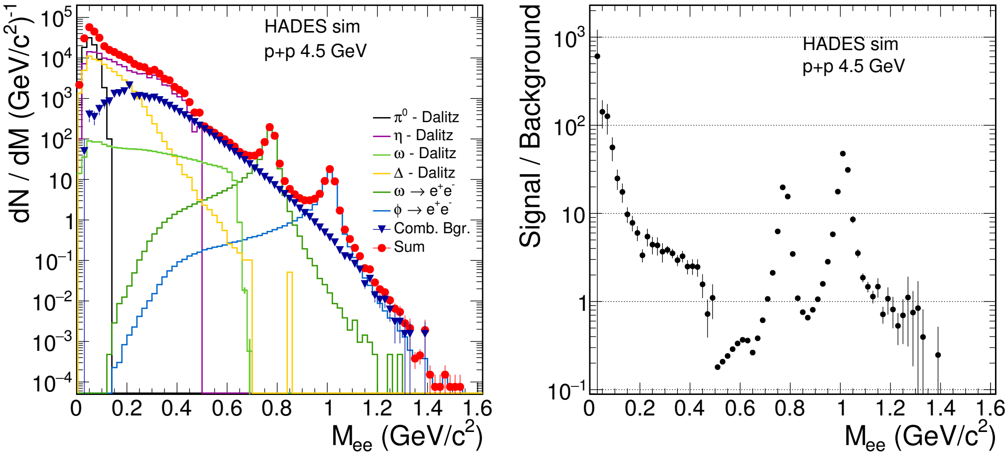

Figure 3.9: Left: Invariant mass distribution of e^+e^- pairs reconstructed in p+p collisions at 4.5 GeV. Right: signal-to-background ratio as a function of invariant mass.

M_{ee} range	<0.15 GeV/c^2	0.15-0.45 GeV/c^2	0.3-0.7 GeV/c^2	>1 GeV/c^2
Rate [84 shifts]	$3.80 \cdot 10^5$	$1.34 \cdot 10^5$	$2.93 \cdot 10^4$ ($2.93 \cdot 10^5$)	52 (520)

Mesons	$\pi^0 \to \gamma e^+e^-$	$\eta \to \gamma e^+e^-$	$\omega \to e^+e^-$	$\phi \to e^+e^-$
Rate [84 shifts]	$1.49 \cdot 10^5$	$2.23 \cdot 10^5$	$9.54 \cdot 10^2$	102

Table 3.5: Pair rates of vector meson direct decays and e^+e^- continuum recorded during 4 weeks of the proton beam on LH$_2$ target. This corresponds to $9 \cdot 10^9$ events (collected during 84 shifts) assuming beam intensity of 1.5×10^7 protons per second, a 1% interaction length target and a trigger rate of 20 kHz.

Introducing high mass resonances to the cocktail would lift the e^+e^- signal in the relevant mass bins (*i.e.* 0.3-0.7 GeV/c^2 and >1 GeV/c^2) by factor of 10 [19] and fill the gap in the $M_{ee} > 0.4$ MeV/c^2. We indicated the estimated e^+e^- rate estimates including this fact in brackets (see Table 3.5).

3.4.2 Ξ^- production

The excess of Ξ^- production in cold nuclear matter (see detailed discussion in Section 1.1.2) has several interesting implications for the interpretation of the heavy-ion data as its origin seems to be already present in the elementary channels without the involvement of many body effects in the medium. Therefore, it is of great importance to investigate the system size dependence of this excess and a measurement of the Ξ^- yield in p+p reactions close to threshold is mandatory.

The production of Ξ^- in the reaction $p+p \to \Xi^- K^+ K^+ p \to \Lambda \pi^- K^+ K^+ p$ can be measured with the upgraded HADES spectrometer, taking advantage of a specific kinematic configuration related to the small Q-value of the reaction close to the threshold. Simulations show that a significant fraction of the protons from either the Λ decay or the direct production is emitted at small angles w.r.t to beam axis and can be efficiently detected in the Forward Detector (FD). On the other hand, soft pions are emitted at larger angles and can be reconstructed in the HADES detector over the complete momentum range using particle identification. The FD is operating in a region without magnetic filed, but the reconstruction of the proton momentum can nevertheless be achieved by a precise time-of-flight measurement in the RPC ($\sigma t = 70$ ps) and a measurement of the track direction by means of the straw tube tracker.

The combinatorial background and background due to particle mis-identification in the FD will be suppressed by topological cuts on (a) the displaced vertex position of the $p\pi^-$ pair candidates ($V_z > 50$ mm) and (b) the minimal distance between proton and pion candidate tracks ($d < 4$ mm). Figure 3.10 shows as example for the semi-inclusive reconstruction of the Ξ^- signal achieved in p+p collisions at 4.5 GeV in two steps: (a) reconstruction of the $\Lambda \to p\pi^-$ invariant mass of proton track candidates in the FD and pions in the HADES (the red histogram shows the combinatorial background originating from combinations of pions from the Λ and the Ξ^- decays and protons) (b) Ξ^- reconstruction via the $\Lambda\pi^-$ invariant mass with a condition on the $p\pi^-$ invariant mass requiring it to be around the Λ peak (left panel).

The reconstructed yield is normalized to the number of produced Ξ^- and includes the branching ratios. The total reconstruction efficiency (including branching ratios) amounts to 9%. This corresponds to around $8 \cdot 10^3$ reconstructed Ξ^- events in p+p collisions at 4.5 GeV assuming a beam intensity of 2×10^8 protons/s and 1μb production cross section. Such intensity can be handled by the upgraded (200 kHz) DAQ system (*cf.* s. 2.1.1).

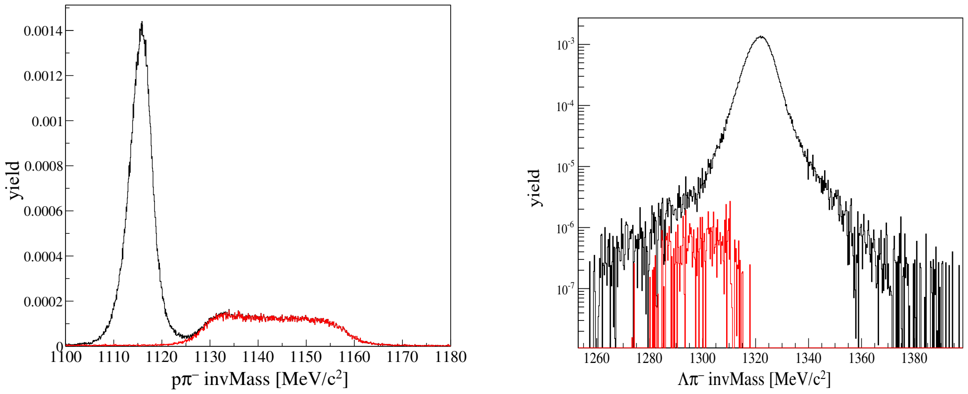

Figure 3.10: Left: Invariant mass distribution of proton track candidates measured in the FD and π^- reconstructed in HADES from $\Xi^- \to \Lambda\pi^- \to p\pi^-\pi^-$ decays (combinatorial background shown in red) after all cuts (see text of the details). Right: $\Lambda\pi^-$ invariant mass distribution, where the Λ are selected from the $p\pi^-$ invariant mass distribution around the Λ peak (shown on the left).

3.4.3 Hyperon form factors

Measurements of the electromagnetic decays of excited hyperons provide an important insight into their structure. The theoretical work [116] stressing the importance of the hyperon radiative decays has been published in the mid-eighties, but there was no experimental progress in the last thirty years.

The hyperon structure can be probed by measurements of the electromagnetic form factors, which are in general a function of the four momentum transfer (q^2) of the virtual photon exchanged either in electro-production experiments (space-like domain where $q^2 < 0$), Dalitz decays ($Y^* \to \Lambda e^+e^-$) or in e^+e^- annihilation experiments (the latter two probe time-like domain where $q^2 > 0$). There is also only few data in the PDG on radiative decays involving real photons.

Recently the CLEO collaboration provided the first measurements of hyperon production in the annihilation experiment at large momentum transfers ($q^2 > 14.2$ GeV^2/c^2) which indicate an important role of correlation effects between quarks [117]. Indeed, quark models, as for example [116], predict a strong dependence of the branching ratios on the hyperon structure, particularly the effects of quark correlation. Also the BESII collaboration is investigating a sector of large momentum transfers (scale of a few GeV), but no results are published yet. Hence, results from HADES on both photon and dielectron decays like $\Lambda(1405) \to \Lambda\gamma(e^+e^-)$ or $\Lambda(1520) \to \gamma(e^+e^-)$ will have significant impact on the understanding of the structure of the strange resonances in the region of small q^2. Particularly, it will be interesting to compare such decays with transitions characterized by the same spin and parity change, but for states which differ by strangeness content like for example $\Lambda(1520)$ and $D_{13}(1520)$ (discussed in the previous section). One of the questions is whether the VDM ansatz holds also in the strange baryon sector, as for example predicted by [118]. Moreover, more differential studies of the decay width as a function of the four momentum transfer and the angular distribution of the final state particle will provide a possibility to measure the magnetic and electric transition form factors of the radiative decays.

These measurement will be possible thanks to the excellent reconstruction capabilities of HADES for dileptons and Λ hyperons, but require a high-rate DAQ system (200 kHz upgrade, *cf.* s. 2.1.1). The hyperon reconstruction will benefit from the proposed Forward Detector (FD) (*cf.* s. 2.2.3) extending the HADES acceptance to forward direction essential for the reconstruction of the proton from hyperon decays. The general idea is to perform a semi-inclusive reconstruction of excited hyperon decays tagged by the reconstruction of the $\Lambda \to p\pi^-$ ground state in association with a dilectron pair. The decaying resonance states can be reconstructed by the Λe^+e^- invariant mass taking advantage of the relatively small widths of the hyperons (like $\Lambda(1520), \Lambda(1405)/\Sigma(1385), \Sigma(1192)$). The measurement can be performed as well in p+p as in p+A collisions. The dielectrons and the pion will be detected in HADES using complete PID information, while the proton from the Λ decay will be measured as well in HADES as in the FD. Since the latter is operating in a region without magnetic field, a reconstruction of the momentum vector will be provided by a precise time-of-flight measurement in the RPC ($\sigma t = 70$ ps) and measurement of the track direction by means of the straw tube stations. The combinatorial background and background due to particle miss-identification in the FD will be suppressed by topological cuts on (a) the displaced vertex position of the $p\pi^-$ pair candidates ($V_z > 30$ mm) and (b) teh minimal distance between proton and pion candidate tracks ($d < 4$ mm). Simulations have been performed for the benchmark channel $\Lambda(1520) \to \Lambda e^+e^- \to p\pi^-e^+e^-$ and for the background channel $\Lambda(1520) \to \Lambda\pi^0\pi^0$ (assuming 10% decay branching ratio) and also for a non-resonant background of similar strength, including one and three neutral pions associated with the Λ. The background originating from the prompt decays of the type $p\pi^-\pi^0\pi^+\pi^-$ has been effectively rejected (98%) by the topological cuts. The signal-to-background ratio has also been investigated by an analysis of experimental data taken in p+p collisions at 3.5 GeV [119] and shows that the ratio is in the order of unity. The simulation results are shown in Fig. 3.12. The total reconstruction efficiency of such decays is of the order of 1.6% which for a total inclusive cross section of Λ production in p+p collisions at 4.5 GeV in the order of 300 μb [120] leads to about 550 semi-inclusive e^+e^- associated with Λ events per day for a PE target and a 2×10^8 proton/s beam.

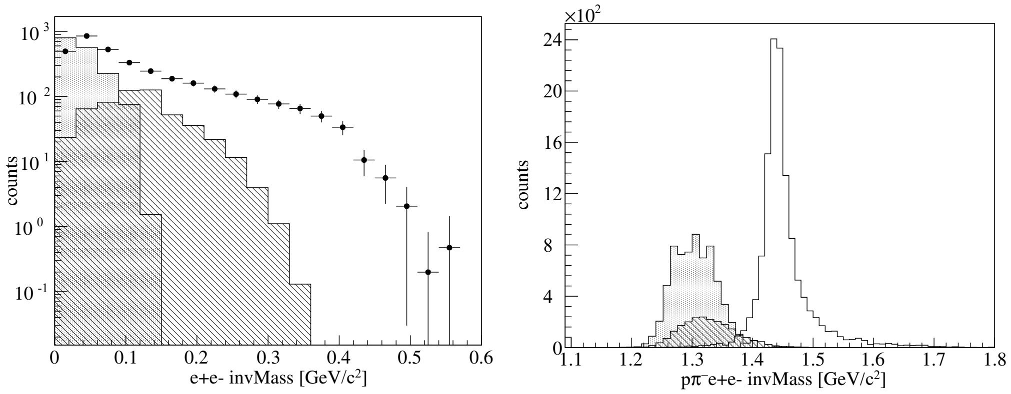

Figure 3.11: Left: Invariant mass distribution of e^+e^- from $\Lambda(1520)$ Dalitz decays after all cuts (see text of the details) and a window on the Λe^+e^- invariant mass, corresponding to the $\Lambda(1520)$ peak, shown on the right, for p+p collisions. Shaded histograms show background contribution from one, two and three neutral pion production (see text for details).

3.5 p+Ag at 4.5 GeV

3.5.1 Inclusive dielectron observables

The feasibility analysis was done in the same way as for p+p at 4.5 GeV. The cross sections for the cocktail contributions besides π^0 and η were scaled up by 42 to account for mean participant number and different reaction cross-sections. The invariant mass distribution corresponding to 10^8 simulated events after the full analysis chain together with the ratio of signal to combinatorial background are shown in Fig. 3.12. ω and ϕ are clearly visible above the combinatorial background. The rates estimated for various e^+e^- sources are sumarized in the Table 3.12.

M_{ee} range	<0.15 GeV/c^2	0.15-0.45 GeV/c^2	0.3-0.7 GeV/c^2	>1 GeV/c^2
Rate [84 shifts]	$8.01 \cdot 10^5$	$2.28 \cdot 10^5$	$4.05 \cdot 10^4$	116

Mesons	$\pi^0 \rightarrow \gamma e^+e^-$	$\eta \rightarrow \gamma e^+e^-$	$\omega \rightarrow e^+e^-$	$\phi \rightarrow e^+e^-$
Rate [84 shifts]	$3.29 \cdot 10^5$	$3.90 \cdot 10^5$	$2.14 \cdot 10^3$	229

Table 3.6: Pair rates of vector-meson direct decays and e^+e^- continuum recorded per 4 weeks of the proton beam on Ag target. This corresponds to $9 \cdot 10^9$ events (collected during 84 shifts) assuming beam intensity of 1.5×10^7 protons per second, 2.8% interaction length target and 20 kHz trigger rate.

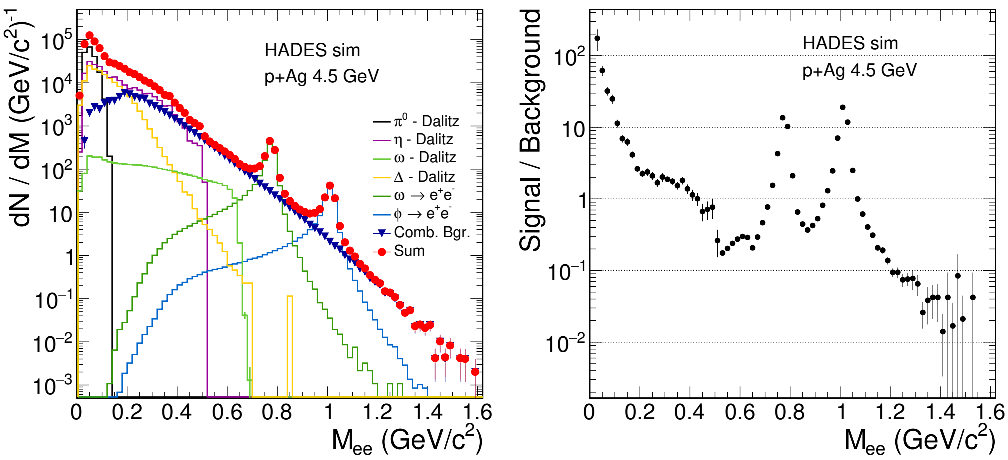

Figure 3.12: Left: Invariant mass distribution of e^+e^- in p+Ag collisions at 4.5 GeV. Right: Signal-to-background ratio.

3.5.2 Search for a dark photon in the dielectron channel

The expected high-statistics dilepton samples will allow to implement a search for a hypothetical mediator of the interaction between dark-matter particles, the so-called dark photon (or A'). The HADES collaboration published first results on such a search in dilepton data already in 2014 [21]. Then we were looking for a dark photon decay signal into e^+e^- pairs in inclusive dielectron spectra obtained from 3.5 GeV proton-induced reactions on either a LH$_2$ or Nb target, as well as in the Ar+KCl at 1.76 A GeV collisions. The reconstructed e^+e^- invariant-mass distributions consisted of a superposition of contributions from different sources which, at masses below 0.6 GeV/c^2, were mainly due to electromagnetic decays of the π^0, η, and the Δ resonance. Assuming a substantial increase of the statistics in the proposed future experiments, we will be able to lower further the actual 90% confidential limit (CL) on such a particle.

Figure 3.13 presents the status of dark-photon searches done in various experiments world-wide, shown in terms of a 90% CL on the upper value of the mixing between photon

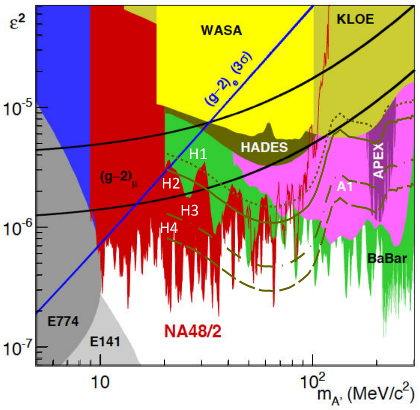

Figure 3.13: Expected HADES exclusion limits of a dark photon search. The four lines correspond to pion-induced reactions (H1, dotted), p+Ag with 20 kHz trigger rate (H2, solid), p+Ag with 80 kHz (H3, dashed-dotted), and p+Ag with 200 kHz (H4, dashed), respectively.

and dark photon, ε^2, vs. the dark photon mass. The published HADES result is also shown as well as predicted sensitivities of future HADES experiments. The four curves labeled H1, H2, H3, and H4 correspond to expected upper limits for different experimental scenarios: pion-induced reactions (H1) and p+Ag at 4.5 GeV (H2, H3, and H4 assuming 20 kHz, 80 kHz, and 200 kHz trigger rate, respectively). The 80 kHz scenario will become possible after a replacement of the MDC front-end electronics, the 200 kHz scenario needs in addition a complete change of the DAQ read-out scheme (*cf.* s. 2.1.1). With these upgrades, we will be able to push the 90% CL on the mixing parameter ε^2 well below the 10^{-6} level.

3.5.3 Hyperon-nucleon interactions

Thanks to the upgrade of the HADES data acquisition system (*cf.* s. 2.1.1), data statistics up to ten times larger than currently available will be collected. On the other hand, the employment of the new electromagnetic calorimeter will allow to reconstruct also Σ^0 hyperons with good statistics and perform Σ^0-p femtoscopy. These new measurements will allow to investigate the hyperon-nucleon interaction with unprecedented precision. Table 3.7 sumarizes the expected statistics of hyperon-proton pairs in a beam time of two weeks.

Experiment	Λ	Λp	Σ	Σp
HADES p+Ag (4.5 GeV)	$3 \cdot 10^6$	$1.5 \cdot 10^5$	10^6	$8 \cdot 10^4$

Table 3.7: Expected hyperon statistics for the measurement p+Ag. The numbers of expected hyperon-nucleon pairs refer to a selection of the relative momentum lower than 150 MeV/c.

3.5.4 Study of short-range correlations in nuclei

Below is an executive summary of the proposed study of short-range correlations in nuclei using the HADES spectrometer. Please see $https://www.hen-lab.com/srchades$ for more detailed on the proposed measurement.

Introduction

Recent high-momentum-transfer triple-coincidence A$(e, e^{'}pN)$ and ^{12}C$(p, 2pn)$ measurements [121, 122, 123, 124, 125, 126] (where A stands for ^{4}He, ^{12}C, ^{27}Al, ^{56}Fe and ^{208}Pb) have shown that nucleons in the nuclear ground state form nucleon pairs with large relative momentum and small center-of-mass (cm) momentum, where large and small are relative to the Fermi momentum of the nucleus (k_F). We refer to these as Short Range Correlated (SRC) pairs [127, 128, 129, 130, 131, 133]. In the range of missing-momentum (*i.e.* the knocked-out proton's initial momentum in the absence of re-interactions) from 300–600 MeV/c, these pairs were found to dominate the nuclear momentum distribution, with neutron-proton (np) pairs nearly 20 times more prevalent than proton-proton (pp) pairs and, by inference, neutron-neutron (nn) pairs. The strong preference for np pairs is interpreted as due to the dominance of the tensor part of the NN interaction at the probed distances [134, 135, 136, 137, 138]. Some of the highlights from the last two decades of experimental SRC studies are shown in Fig. 3.14.

The experimental program proposed here (as part of FAIR Phase-0) is to study SRC via measurement of the exclusive A$(p, 2pN)$ reactions (N = neutron or proton). The proposed

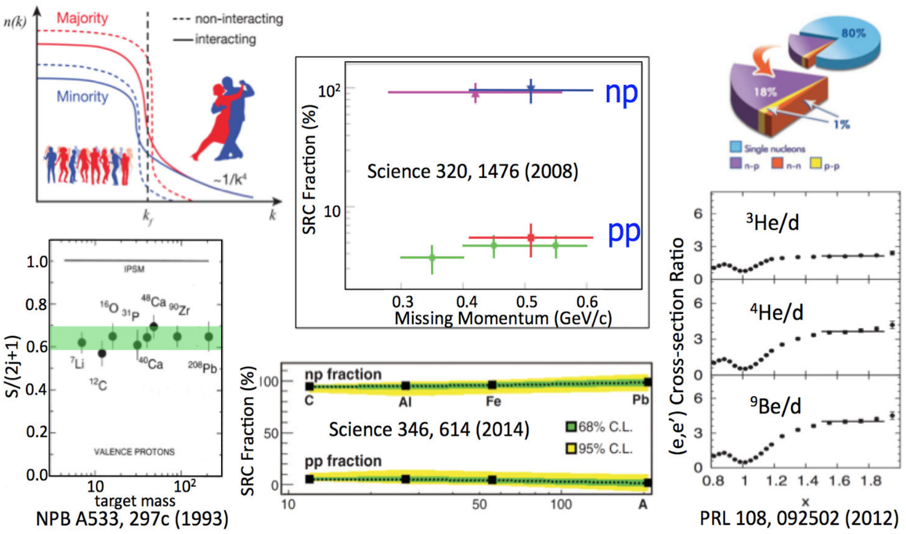

Figure 3.14: Collection of the SRC highlight results.

measurement will utilize the 4.5 GeV high intensity SIS18 proton beam and the large acceptance HADES spectrometer with part of the NeuLAND detector to measure the recoil neutron [139] and detect the two leading protons emitted in the reaction. Details of the physics program can be found in [140]; here we summarize its main highlights. The first measurement of the SRC pairs assumes a proton beam of 2×10^6 protons/sec incident on a segmented ^{107}Ag target running in parallel to the dielectron experiment (*cf.* s. 3.5.1) but with an additional detector at backward angles to measure recoil neutrons [140]. The scientific goals of this measurement are to:

1. Investigate the Migdal-Luttinger jump in the nucleonic momentum distribution which describes the transition from a mean-field part to the high-momentum tail that is dominated by SRC. **The main advantage of HADES is the high statistics that will allow accurate mapping of the expected transition.**

2. Study the factorization of the reaction mechanisms at low energies **to understand the limits of factorization in hard breakup reaction towards the development of a FAIR program to study SRC in short-lived nuclei in inverse kinematics**.

We estimate **a total of about** $2.2 \cdot 10^3$ **np-SRC events from the** $^{107}\mathbf{Ag}(p, 2pn)$ **reaction** [140] (10 times more events than the existing JLab $(e, e'pn)$ data). The simulated expected results are shown in Fig. 3.15 (left panel), compared to the ^{12}C$(p, 2pn)$ data from BNL [123, 124] that had limited statistics of 18 np-SRC events (insert).

We anticipate having sufficient data to determine the minimal value of |-t| for which the reaction factorizes and can be described as a product of the elementary cross section times a decay function of the SRC pair. This information is important both for understanding the reaction dynamics, but also for planning future studies of SRC with relativistic beams of unstable nuclei in inverse kinematics at FAIR.

For a second measurement of SRCs (after 2019), we assume a dedicated run with 1×10^7 protons/sec and the ability to detect recoil protons and neutrons using different nuclear targets *e.g.* ^{12}C, ^{40,48}Ca, ^{56}Fe and ^{107}Ag [140]. The goals for this measurement are to:

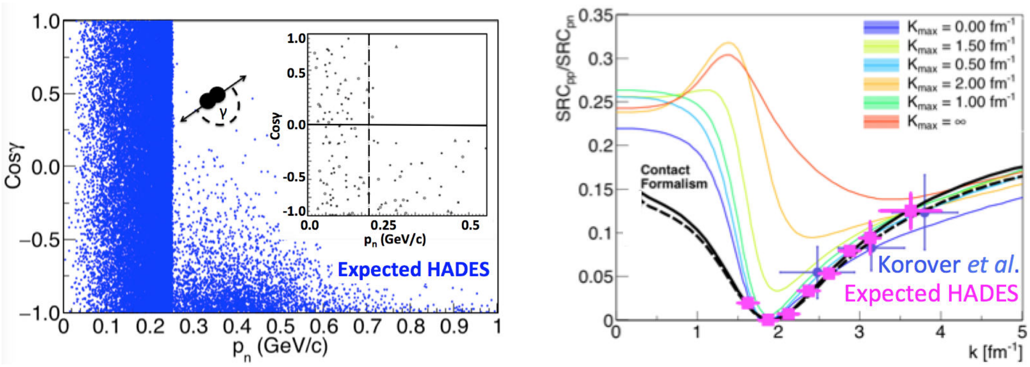

Figure 3.15: Left: The Migdal jump as can be mapped with the anticipated GSI events taking into account the expected statistics and resolution, compared with existing BNL data [123, 124] shown in the insert. Right: The ratio of pp to pn SRC pairs in ^{4}He as a function of the pair momentum extracted from $^4\text{He}(e, e'pN)$ measurements (circles) [126]. The colored lines show ab-initio two-body momentum density ratios, integrated over the cm momentum from 0 to K$_{max}$ (we vary K$_{max}$ from zero to infinity [136]). The solid (dashed) black line is a contact theory prediction of [141]. The square points show the projection of the pp/pn ratios with the expected statistics from GSI.

1. Study the details of the short-range part of the NN interaction, in particular **the transition from tensor dominance to the repulsive scalar core.**
2. **Measure exclusive A(p,2p2N) quasi-elastic reactions to probe, for the first time, 3N-SRCs configurations.**

In Fig. 3.15 (right panel) state-of-the-art ab-initio calculations [136] and measured [126] proton-proton (pp) to proton-neutron (pn) pair density ratios in ^{4}He are shown as a function of their relative momentum. The calculated pair density ratio is obtained by integrating up to maximum cm momentum, K$_{max}$, that varies from zero to infinity. The dashed line is a contact formalism-based calculation [141] that assumes SRC pairs can be described by a function that depends on the pair cm momentum (Q) times a universal two-body function that depends only on the pair relative momentum (q).

The transition from tensor dominance to the repulsive scalar core is clear in both the calculations and the data. However, the present data [126] have large statistical uncertainties that limit its ability to challenge the theoretical calculations. We anticipate collecting **a total of about** $10 \cdot 10^3$ **np-SRC and** $6.3 \cdot 10^3$ **pp-SRC events** which equals to a 100 times increase in statistics compared to the existing JLab data. The expected HADES measurements are also shown in Fig. 3.15.

The high statistics of 2N-SRCs will permit also to search for 3N-SRCs via the $\text{A}(p, 2pnn)$ and $\text{A}(p, 2ppn)$ reactions (two recoil nucleons). Neither the rate nor the geometry of these 3N-SRCs is known. The yield of 3N-SRC events (assuming that their statistics are 1% of the 2N-SRC pairs) will allow us to identify and study these events for the first time.

The Measurement

The kinematical scheme for a triple coincidence measurement is shown in Fig. 3.16 (left panel).

In the Plane Wave Impulse Approximation (PWIA) for a pair at rest, P_{miss} is equal in size and opposite to the 3-momentum of the recoil nucleon. Simulations for $\text{A}(p, 2pN)$ for a

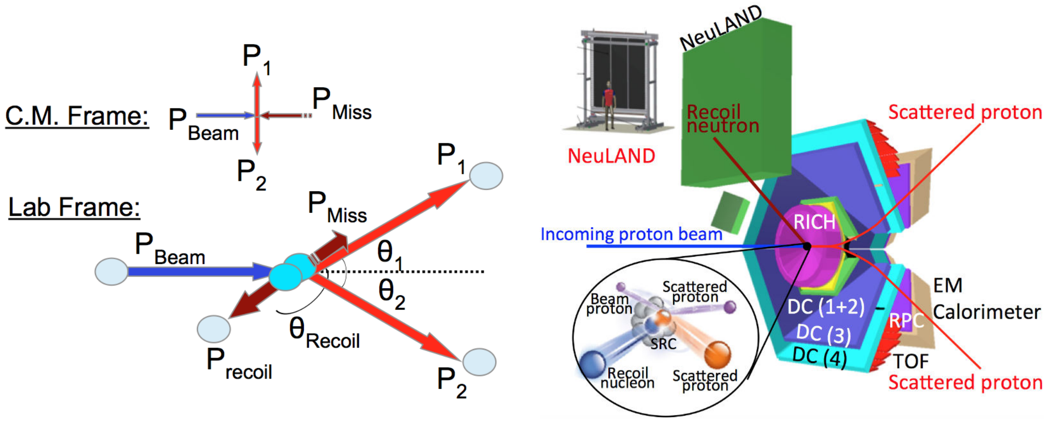

Figure 3.16: Left: Kinematics for a proton beam scattering off of a proton in a SRC-pair. The beam proton scatters from a proton within the SRC-pair with initial momentum P_{miss} at $\theta_{cm} = 90°$, knocking it from the nucleus. The short-range-correlated partner recoils backward with momentum P_{recoil}. Right: The proposed experimental setup including HADES and the NeuLAND detectors. Parts of HADES such as the RICH, the sets of Drift Chambers (DC), the Resistive Plate Chambers (RPC), the Time Of Flight (TOF) system, and the electromagnetic (EM) calorimeter can be seen in the figure together with NeuLAND detector and one of the two small recoil detectors.

proton beam energy 4.5 GeV can be found in ref. [140]. The kinematical constraints imposed in the simulation are: energy and momentum conservation: $\theta_{cm} = 90 \pm 30°$, co-planarity: $(|\Delta\phi| = 180 \pm 20°)$, $|s, t, u| \geq 2\ \mathrm{GeV}/c^{\ 2}$, $|P_{miss}| \geq 250\ \mathrm{MeV}/c$. The forward going protons mostly scatter at laboratory angles of 18–45° relative to the beam with momentum of 1.5–5.0 GeV/c. The backward going recoil nucleons can be detected at laboratory polar angles of 90–160° [140].

The kinematics dictate the necessary detection system: a forward detector to measure the two leading protons and to form the event trigger (HADES), along with a backward detector to measure the recoil nucleon (part of NeuLAND) in coincidence with the forward going protons. Additional small size detectors are also considered to increase 3N-SRC sensitivity. Details on the setup can be found in ref. [140].

For the first SRC measurement, we propose using a ^{107}Ag target and run in parallel to the dilepton program. For a future dedicated SRC measurement, we also propose to use additional nuclei such as ^{12}C, ^{40,48}Ca, ^{56}Fe. The target thickness are chosen to yield 2% interaction probability. To allow low energy protons to exit the target, we propose using 10 foils separated by 5.5 mm [140]. The trigger schemes along with anticipated signal and background rates for both the first phase (in parallel with the dilepton measurement) and second phase (dedicated SRC run) are described in detail in ref. [140].

3.6 Reconstruction of photons and photonic decays of neutral mesons

The addition of a calorimeter to HADES allows to measure real photons. This opens the possibility to identify light neutral pseudo-scalar mesons (π^0 and η) via their decay into two photons. To investigate the feasibility of π^0 and η reconstruction, events from a dedicated UrQMD simulations of Ag+Ag collisions at 1.65 A GeV and proton-induced reactions on a

LH_2 or Ag target at 4.5 GeV were used with statistics of 10^7 and 10^8 respectively. In the case of Ag+Ag reaction, the 44% most central events were simulated (maximum impact parameter $b_{max} = 8$ fm). The results presented here correspond to semi-central events, 20.6% - 43.7% centrality, with a statistics of 5.3 million events.

A full GEANT3 simulation of the ECAL detector and all other detectors of the HADES setup was performed. In the π^0 and η analysis, the diphoton mass was reconstructed taking into account all possible combinations of the identified photons. To estimate the combinatorial background, the mixed-event method was used. All combinations of two photons from different events formed the invariant-mass background distribution which was then normalized to the measured one outside the meson peaks. In order to improve π^0 reconstruction, only photons with energy above 150 MeV were used for both signal and background reconstruction.

Table 3.8 shows the meson multiplicities in full solid angle, geometrical acceptance and reconstruction efficiency of π^0 and η. Please note that the acceptance factor (ACC) includes also the decay branching ratio into $\gamma\gamma$. Acceptance is quoted with two numbers, where the first one includes a minimum cut on energy deposited in the calorimeter in order to have better signal-to-background (S/B) ratio in the π^0 region. Table 3.9 summarizes the quality of the π^0 and η reconstruction. The upper two rows of the table correspond to the number of simulated events, whereas the lower two rows to the expected number of events obtained in a run $5 \cdot 10^9$ for Ag+Ag and $9 \cdot 10^9$ for proton-induced reactions, respectively.

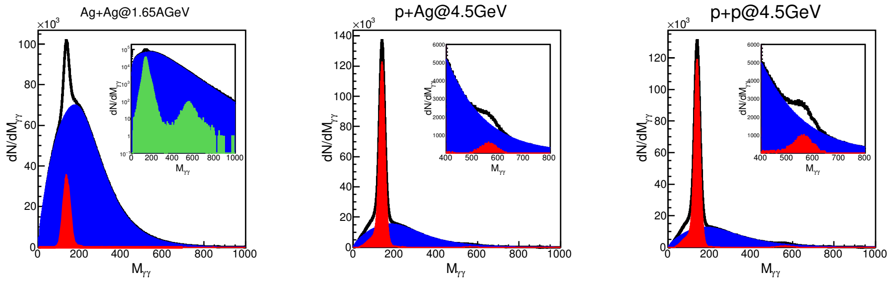

Figure 3.17: Diphoton invariant mass spectra reconstructed in Ag+Ag (left panel), p+Ag (middle panel) and p+p (right panel) collisions together with the mixed-event combinatorial background (blue histogram) and signal after background subtraction (red histogram) and true signal from Geant3 (green).

For both systems, a clear π^0 peak is visible on top of the combinatorial background, for p+Ag and p+p also the η is visible. However, in 4 weeks of Ag beam we expect $5 \cdot 10^9$ events which, with careful combinatorial background subtraction, will allow to extract a significant η signal as well (see Table 3.9). As a conclusion, from the expected statistics it will be possible to perform a differential analysis for both mesons using the ECAL.

	Ag+Ag	p+Ag	p+p	Ag+Ag	p+Ag	p+p
	$\pi^0 \rightarrow \gamma\gamma$			$\eta \rightarrow \gamma\gamma$		
mult/evt	5.36	0.945	0.42	0.053	0.0263	0.0186
ACC [%]	4.6(9.2)	3.6(6.2)	8.0(13)	4.7(4.7)	2.2(2.2)	4.0(4.0)
EFF [%]	50	60	61	53	59	59

Table 3.8: Meson multiplicities in full solid angle, geometrical acceptance and reconstruction efficiency of the π^0 and η.

	Ag+Ag	p+Ag	p+p	Ag+Ag	p+Ag	p+p
	$\pi^0 \to \gamma\gamma$			$\eta \to \gamma\gamma$		
S/B	0.3	3.5	4.3	0.007	0.2	0.24
S/$\sqrt{S+B}$	378	1340	1262	5.5	71	93
σ [MeV (%)]	16 (11)	13 (9)	13(10)	43 (8.3)	41 (7.3)	41(7.4)
S/$\sqrt{S+B}[4weeks]$	8318	11774	11995	120	683	891
$Rate[4weeks]$	$3.2\cdot 10^8$	$1.8\cdot 10^8$	$1.8\cdot 10^8$	$3.4\cdot 10^6$	$3.0\cdot 10^6$	$3.9\cdot 10^6$

Table 3.9: Quality of the π^0 and η reconstruction using the electromagnetic calorimeter.

3.7 Physics goals for SIS100 operation

The motivation for operating HADES as part of the Compressed Baryonic Matter program at SIS100 is two-fold: First, HADES can bridge the gap from the SIS18 energies to the upper SIS100 region where the CBM acceptance is more favorable. It offers the opportunity to measure dilepton spectra and strange particles in heavy-ion collisions with two different spectrometers allowing to better control systematic uncertainties. Second, HADES can serve as ideal spectrometer to continue reference measurements focusing on cold matter studies. As medium-effects feature strong momentum dependence, the relevant phase space for meson production and propagation is near the target rapidity. The acceptance for *e.g.* pions is almost two units of rapidity centered around $y_{lab} = 1$. Moreover, HADES can also be operated with a liquid hydrogen target providing valuable data from p+p collisions which is not foreseen in CBM. Any reference measurements, as well as a continuation of the physics program of HADES at SIS18 is possible at the new experimental site.

Chapter 4

Proposed experiments for 2018 - 2019

Contents

4.1 HADES proposal pion

Pion induced reactions

The HADES Collaboration

Spokespersons: J. Stroth (j.stroth@gsi.de), P. Tlusty (tlusty@ujf.cas.cz)
GSI contact: J. Pietraszko (j.pietraszko@gsi.de)

Infrastructure: SIS18, pion production target and HADES cave

Beam: Nitrogen at $2\,A$ GeV, maximum intensity, slow extraction

Abstract

We will study baryon excitation and decay in the third resonance region. Emphasis is on the electromagnetic structure of baryons and the role of intermediate ρ mesons as doorway states in the decay process. The measurement of e^+e^- production off the nucleon is sensitive to the electromagnetic transition form factors of baryons in the time-like region and probes the role of vector mesons (ρ, ω). Differential cross sections for hadronic final states will be included in Partial Wave Analyses to extract various baryon-meson couplings, among which are ρN and ωN, with unprecedented precision. Pion-nucleus data allow to investigate medium effects in cold nuclear matter. The whole data set constitutes an important input to calculations of the emissivity of dense and hot hadronic matter. Details can be found in chapters 3.1.1 and 3.2.

Below is an executive summary of the proposed study with π^- beam using the HADES spectrometer. Please see `http://web-docs.gsi.de/~galatyuk/hades_public/HadesSis18_proposal_19_June_2017_final.pdf` for more details on the proposed measurement.

This is a new experiment proposal.

We request 89 shifts.

4.1.1 State of the art

The main goal of the HADES experiment is to explore the microscopic structure of dense baryonic matter. HADES experiments performed in the last years in nucleus-nucleus and proton-nucleus reactions (*cf.* s. 1.1.1) have shown the important role played by the propagation of far off-shell ρ mesons due to their coupling to baryonic resonances in hadronic matter, visible as an excess radiation of the e^+e^- production above conventional sources for invariant masses below the vector meson poles. To provide a reference to these medium effects and to study the electromagnetic structure of the baryonic resonances an important programme has been developed by the HADES collaboration which investigates elementary reactions like pp, quasi-free $'n'p$ and recently πp (*cf.* s. 1.2). We propose to use the GSI pion beam for an experiment that combines the two aspects of this program and will provide results connecting hadronic physics and nuclear matter studies.

Pion beam experiments are a unique tool for baryon spectroscopy. While very precise data exist for many hadronic channels from photon-induced reactions, progress in the determination of the baryon spectrum and its decay property is currently limited by the lack of precise data from pion beam experiments. The combination of the GSI pion beam with the HADES detector offers the opportunity to improve the very poor existing data base for such reactions. A better determination of the couplings of baryonic resonances to ρN and ωN final states is particularly important for the HADES program due to their important role in dilepton emission. Moreover, the $\pi^- p \rightarrow n e^+ e^-$ reaction can be used to study the electromagnetic structure of baryon transitions in the region of small positive four-momentum transfer squared ($q^2 = M_{ee}^2$), where vector meson poles play an important role. This information is complementary to the one obtained in electron scattering experiments in the space like region ($q^2 < 0$) and is therefore needed for a global understanding of these transitions. The differential cross sections in the $\pi^- p \rightarrow n e^+ e^-$ reaction can be parametrized in a model independent way using different equivalent functions (helicity amplitudes, form factors or density matrix elements), which contain information on the electromagnetic structure of the baryon transitions. In the context of the HADES programme, the justification for studying the $\pi^- p \rightarrow n e^+ e^-$ reaction is to establish the role of vector mesons in baryon electromagnetic transitions. More generally, the data base for meson production in pion-nucleus reactions is of fundamental interest for many applications, like *e.g.* the validation of hadronic models used for GEANT4 simulations and as reference for microscopic transport models used to describe heavy-ion collisions.

While medium modifications are expected to be stronger in heavy-ion collisions due to the elevated densities, sizeable effects are already predicted in cold matter. The latter has been mainly studied up to now using photon or proton beams. A breakthrough was achieved by the HADES collaboration thanks to the capability to measure dielectrons close to target rapidity, *i.e.* at low relative momentum to the cold matter. The pion beams offer an even increased sensitivity due to their specific (nearly recoilless) kinematics (*cf.* s. 3.1.2). The proposed measurements on the carbon target will provide information on effects like Fermi momentum and multi-body interactions, yet the full picture will become available once also high-statistics data are a heavy target (*cf.* s. 3.2.4).

The feasibility of such measurements with a pion beam has been successfully tested by the HADES collaboration in two experiments in 2014. In the first one, kaon production was studied in π^-+C and π^-+W reactions at $\sqrt{s} \sim 2\,\text{GeV}$. In the second one, the pion production on hydrogen and the "quasi-free" dielectron production were explored using a polyethylene ($(\text{CH}_2)_n$=PE) target in the second resonance region ($\sqrt{s} \simeq 1.49\,\text{GeV}$) (*cf.* Sect. 1.2.2 and [147]). We propose here a new experiment under much improved conditions for the third resonance region ($\sqrt{s} \sim 1.74\,\text{GeV}$), where many baryonic resonances contribute ($\Delta(1620), \Delta(1700), N(1650), N(1675), N(1630), N(1710), N(1720), \cdots$). We will study both, dielectron and (strange) meson production in π^-+p and π^-+C reactions.

4.1.2 Expected results

The expected results will have an impact in three different fields which are intimately connected as described in the previous section.

- **Electromagnetic structure of baryonic resonances:** These data will provide the very first precise information on time like electromagnetic baryon transitions in the third resonance region. The energy $\sqrt{s} = 1.74$ GeV is chosen 20 MeV above the ω threshold, a region where significant $\rho - \omega$ interference effects are predicted. In addition to the invariant-mass distribution, additional sensitivity to the electromagnetic structure of the baryon transitions will be obtained by the extraction of the spin density matrix coefficients from the lepton angular distributions. As mentioned above, these coefficients provide a parametrization of the data which can be directly compared to models. Fig. 4.1 shows the data quality of relevant spin density matrix elements which can be reached with the running time detailed below (*cf.* s. 4.1.4). The analysis of the 2014 experiment allowed for a proof-of-principle of the method and for the extraction of first preliminary results in the region of the N(1520) (*cf.* s. 3.2.1). This time, we aim to acquire a statistics for the signal 20 times larger (*cf.* s.3.2.2). With this increased statistics, we will reconstruct the longitudinal (related to Coulomb form factors) and transverse (related to the Electric and Magnetic form factors) contributions at finite $q^2(= M_{ee}^2)$ using the amplitudes measured in the channel $\gamma n \rightarrow \pi^- p$. In addition, thanks to the precise ρN and ωN couplings that will be obtained from the analysis of the two pion production channels, the validity of the Vector Dominance Model can be checked. Finally, the predicted $\rho - \omega$ interference effects [142, 143] can also be investigated.

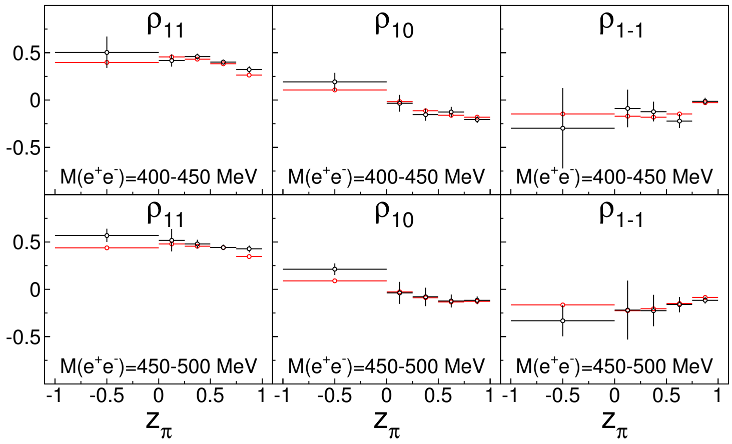

Figure 4.1: Precision on the spin density matrix elements ρ_{11}, ρ_{10} , ρ_{1-1} expected for 10^4 background-free events as a function of $z = cos\theta_{CM}$ and for two bins in dilepton invariant mass M_{ee}. The red points show results obtained in the full solid angle and the black points for events measured within the HADES acceptance.

- **Baryon-meson couplings:** We will measure various exclusive hadronic channels in the π^-+p reaction, between $\sqrt{s} = 1.68$ GeV and $\sqrt{s} = 1.8$ GeV at five different energies, using a spacing of 30 MeV. These data will provide an extraction of many poorly known hadronic couplings of baryon states in the third resonance region. Thanks to our collaboration with the Bonn-Gatchina group, these measurements will be included in a Partial Wave Analysis, together with the very precise existing measurements of photon induced reactions. Many exclusive channels will be measured simultaneously, including also channels with neutral mesons, thanks to the new Electromagnetic Calorimeter (*cf.* s. 2.2.1). In first place, the two-pion channels with a cross section of order $7 - 10$ mb can be measured with a very large statistics and will provide new determinations of the very poorly known branchings to the 2πN channels, and especially to ρN which has a strong impact for medium effects, as mentioned above. Resonant channels of the type $N(1440)\pi, N(1520)\pi, \cdots$ also attract much interest since they are related to a three body nature of baryonic resonances, which might be a dominant character in the case of the unobserved (or "missing") resonances. The data base for the ηn, KΛ and $K\Sigma$ channels will be also improved, which can in particular be used to firmly establish the existence of some resonances. The HADES measurements of hadronic channels in the π^-+p reaction will therefore act as a precursor for future meson beam experiments dedicated to baryon spectroscopy[144, 145].

- **Cold nuclear matter effects:** The measurements with the carbon target, which are needed for extracting the proton contribution in the PE target, will also be used to study e^+e^- and meson production in π^-+C reactions. Inclusive dielectron invariant mass spectra will provide a useful reference for studies of cold matter effects in heavier targets and significant effects could possibly be already observed as well. We will measure the excess of dielectron production below the vector meson pole, which is supposed to be due to the propagation of off-shell ρ mesons. In addition, due to the moderate recoil of mesons produced off baryons in pion induced reactions, a large fraction of the produced ωs will decay inside the nucleus. This gives a unique possibility to observe possible in-medium distortion of the ω spectral function in addition to the ρ one, with already measurable effects being predicted in a small nucleus such as carbon [113]. Using the proton target spectra as a reference, ω absorption effects, sensitive to the ω-N potential will be studied for a small system. We will also try, using again the proton target reference, to investigate ρ-ω interference effects, which are predicted to gradually vanish in the medium. Mesons (pions, η, kaons,...) will be very copiously produced and their production spectra will serve as valuable benchmark for hadronic models. Kaons will be used to study the kaon-nucleus potential as demonstrated for HADES data in p+Nb [20] and under investigation in the most recent pion beam data from the 2014 experiment.

4.1.3 Experimental set-up

We will use the HADES setup, with all sub-detectors, including the new Electromagnetic Calorimeter and the pion tracker, which is based on two planes of silicon detectors placed in the beam line (CERBERUS) and the segmented scCVS-based diamond detector in front of the HADES target. The secondary pion beam is produced using an extracted primary ^{14}N beam at the highest possible intensity impinging on a 10 cm long beryllium target. During the commissioning pion-beam experiment in 2014 we validated the beam optics of the transport section behind the production target. In order to guarantee optimal momentum resolution of the pion beam reconstruction, which is in particular important for the exclusive channels, a precise and reproducible focus of the primary beam onto the center point of the production target is required. The pions in a selected momentum range (with a bandwidth of about 1.7% (*rms*) are transported up to the HADES target by a set of nine quadrupoles and two dipoles. We will use the quadrupole settings, deduced from second order beam optics calculations, that optimize the acceptance and focus requirements of the pion beam line. Different incident momenta of the pion beam will be selected by scaling the pion transport line accordingly. The event-by-event pion beam momentum reconstruction, with a resolution better than 0.3%, is enabled by in-beam tracking detector CERBEROS.

We will use two different targets: a polyethylene (PE) block with a length of 4.6 cm and a diameter of 12 mm and a carbon (C) target consisting of 7 segments, each 3.6 mm long, 12 m in diameter and interspersed by 7.1 mm. The choice of a PE target is dictated by the larger density (factor 2) of protons ($4\ 10^{23}\ /\mathrm{cm}^2$) as compared to the one available in a LH_2 targets and the absence of background originating from interactions with the target vessel. The latter is unavoidable due to the pion beam diameter (FWHM $\sim 1.5 - 2\,\mathrm{cm}$) which exceeds the diameter of the LH_2 target. Both targets exist and were already used in the previous experiment. The trigger of the acquisition will be given by a coincidence between a fast signal in the diamond detector and at least two signals in the RPCs or TOF-scintillators.

4.1.4 Justification of the beam time

The experiment in 2014 was realized with $2\ 10^5$ pions per spill on the HADES target produced by a few 10^{10} primary nitrogen ions. We used moderate extraction times to realize a 50% duty cycle. We used 36 shifts with on average 14 h beam on target per day. From this statistics we obtained, at a pion momentum of 0.7 GeV/c, 500 reconstructed e^+e^- pairs in the channel $\pi^- p \to ne^+e^-$, and 1000 in the same channel but from quasi-free reactions on the carbon in the PE target.

To arrive this time at the required statistics of close to 10^4 pairs above π^0 mass from π^-+p reactions (*cf.* s. 4.1.2 above), we need only 41 shifts on PE. This beam time estimate considers the following changes w.r.t. 2014 influencing the rate with which the statistics is collected. First, the flux of π^- with $p = 1.1$ GeV/c at the production target is a factor of two higher compared to π^- with momentum $p = 0.7$ GeV/c^2, due to the forward boost of the produced pions [146]. Second, we assume that the the primary beam intensity at the production target can be increased by a factor of two due to the now enhanced shielding and additional measures taken by the accelerator group to improve the extraction efficiency. Indeed, an operation with intensities close to 10^{11} ions in SIS18 was shortly reached during the commissioning run in 2014 but had to be abandoned due to insufficient extraction efficiency and shielding at that time. More over, we take into account the increase of the ρ / ω production cross section due to the higher pion momentum by another factor two, and further assume an improved e^+e^- reconstruction efficiency by yet another factor two due to the new RICH photon detector. All together we therefore consider that the collection rate increases by a factor 16.

The number of shifts needed for measurements with the carbon target is calculated to minimize statistical errors due to the subtraction, a situation which we unfortunately encountered in 2014 due to the limited beam time. Now we expect a statistics of $1.7 \cdot 10^4$ reconstructed pairs above the π^0-Dalitz region which can be used to study medium effects on ρ and ω production. Between 30% and 50% of these pairs are expected to stem from ω decay and can thus be used to investigate nuclear effects in ω production. Last but not least, combining the measurements obtained from both targets, we can also analyze a total of $4.6 \cdot 10^4$ pairs from a mix of free and quasi-free $\pi^- + p \to ne^+e^-$ reactions.

To study the hadronic channels, we want to perform an energy scan by adding two measurements below ($\sqrt{s} = 1.68$ and 1.71 GeV/c^2) and two above ($\sqrt{s} = 1.77$ and 1.8 GeV/c^2)

$\sqrt{s}$ (GeV)	shifts PE(C)	$\pi^+\pi^-n$	$\pi^0\pi^-p$	$K^0\Lambda$	Σ^0K^0	Σ^+K^-	ηn	e^+e^-n ($M > 150MeV/c^2$)
σ		10 mb	7 mb	0.6–0.3 mb	0.25 mb	0.2 mb	1.25 mb	
1.68	2 (1)	$3.2\ 10^6$	$2.2\ 10^6$	$2.6\ 10^4$	$1.2\ 10^4$	$6\ 10^4$	$1.6\ 10^5$	440 (1320) (570)
1.71	2 (1)	$3.2\ 10^6$	$2.2\ 10^6$	$2.6\ 10^4$	$1.2\ 10^4$	$6\ 10^4$	$1.6\ 10^5$	440 (1320) (570)
1.74	41 (30)	$6.6\ 10^8$	$4.5\ 10^7$	$5.3\ 10^5$	$2.5\ 10^5$	$1.2\ 10^6$	$3.3\ 10^6$	9000 (27 k) (17 k)
1.77	2 (1)	$3.2\ 10^7$	$2.2\ 10^6$	$2.0\ 10^4$	$1.2\ 10^4$	$6\ 10^4$	$1.6\ 10^5$	440 (1320) (570)
1.8	2 (1)	$3.2\ 10^7$	$2.2\ 10^6$	$1.4\ 10^4$	$1.2\ 10^4$	$6\ 10^4$	$1.6\ 10^5$	440 (1320) (570)

Table 4.1: Number of requested shifts for the measurements on the polyethylene (PE) and C (in brackets) and expected number of reconstructed events (histogram entries) for the reaction on free protons for the different channels. For the e^+e^-n channel three numbers are given referring to the number of reconstructed events corresponding to free π^-+p scattering and additionally the total from reaction in the PE target and for the carbon target (numbers in first and second bracket, respectively).

the center energy. As deduced from the analysis of the 2014 experiment, the Partial Wave Analysis of these reactions requires a statistics of about 10^5 events after subtraction of the carbon induced contributions for the $2\pi N$ channels and of 10^4 for the two-body channels. For the channel Σ^0K^0, which has the smallest yield (*cf.* s. 3.2.2), this goal can be obtained with two shifts on the PE target and one shift on the C target This amount to a total of 12 additional shifts for the excitation function of hadronic final states. The e^+e^- events provided by these measurements can be added to the statistics measured at $\sqrt{s} = 1.74\,\text{GeV}$, hence providing more than 10^4 pairs for the $\pi^-p \to ne^+e^-$ reaction for e^+e^- invariant masses larger than the π^0 mass. The table 4.1 summarizes the total yields that will be measured for the different channels at the five energies.

Finally, we need six additional shifts for tuning of the beam line. In particular, the alignment of the primary beam on the pion production target and of the pion beam on the diamond detector in front of the PE/C targets needs careful adjustments of the corresponding dipoles. Our total request therefore amounts to **89** shifts.

4.2 HADES proposal ion

Studies of resonance matter with Ag+Ag collisions.

The HADES Collaboration

Spokespersons: J. Stroth (j.stroth@gsi.de), P. Tlusty (tlusty@ujf.cas.cz)
GSI contact: J. Pietraszko (j.pietraszko@gsi.de)

Infrastructure: SIS18 and HADES cave

Beam: Ag at 1.65 A GeV, beam intensity 2×10^6 ions/s (flat top), slow extraction

Abstract

We will study baryonic matter in the region of high net-baryon density. The Ag+Ag collision system is optimized to reach a high enough beam energy for abundant strangeness and vector meson production while yet realizing a large interaction volume. We aim at a high statistics run to enable the observation of the ϕ meson, in both the e^+e^- and K^+K^- decay channels. This statistics will also yield continuum dielectrons in the region where $\rho - a_1$ chiral mixing is expected and might open the door to triple-strange baryons. Details can be found in sections 3.1.1 and 3.1.3.

Below is an executive summary of the proposed study with Ag beam using the HADES spectrometer. Please see `http://web-docs.gsi.de/~galatyuk/hades_public/HadesSis18_proposal_19_June_2017_final.pdf` for more details on the proposed measurement.

This is a new experiment proposal.

We request 88 shifts.

4.2.1 State-of-the-art

Unraveling the properties of strongly interacting (QCD) matter at non-zero temperatures and densities is essential for our understanding of the physics at the smallest and largest scales, from nuclei to neutron stars, supernova explosions and the early universe. In the laboratory, QCD matter is studied with the help of nuclear collisions where matter under extreme conditions is produced in a transient state. The conditions reached in such collisions can be altered by choosing different beams and by varying the collision energy [4, 5, 6, 7, 8, 9, 10, 13]. In heavy-ion collisions at a few GeV per nucleon the system is compressed in the initial phase of the reaction beyond nuclear ground state density [43, 148] and hence substantial modifications of the hadron properties are expected to occur [38, 149]. It is conjectured that at high enough densities hadronic degrees of freedom finally disappear and a chirally restored phase of quarks emerges [11, 12, 14].

The combined measurement of dielectrons and strangeness performed by HADES in Ar+KCl and Au+Au collisions have provided new intriguing results which call for further systematic investigations. The spectral distribution of virtual photons emitted from the collision zone of A+A collisions indicates strong medium effects beyond those resulting from a pure superposition of individual N+N collisions [15, 16]. This observable as well as the measured hadron abundances in the final state [9] show features of a thermalized fireball. Baryon-driven medium effects influence significantly the ρ meson in-medium spectral function and are considered essential in describing the low-mass dilepton spectra [14, 34, 35, 36, 37]. For the first time at SIS energies, an ω meson signal in the e^+e^- decay channel has been identified in p+p [19, 40], p+A [20] and Ar+KCl [15] collisions. Furthermore, the anticipated 2% mass resolution has been demonstrated in the analyzed p+p data. While the measured abundances of all reconstructed particles are well described by assuming thermalization, the double strange $\Xi^-(1321)$ production in A+A [27] and p+A [28] collisions exhibits a sizeable enhancement above predictions of statistical hadronization and transport model calculations.

A deeper understanding of the microscopic properties of resonance matter requires, however, systematic multi-differential analyses of various observables. Up to now, due to the limited statistics, the study of multi-differential emission probabilities of vector mesons and multi-strange hadrons was not possible. Therefore, we propose to continue the investigations with a large collision systems and at the highest possible beam energies achievable at SIS18. Optimal for these purposes is the Ag+Ag system at 1.65 A GeV. It allows to perform high-statistics and systematic investigations of e^+e^- pair production in invariant-mass region of vector mesons and above 1 GeV/c^2 to complete the systematics on (multi-)strangeness production and propagation in heavy-ion reactions, and to further investigate particle correlations and fluctuations. HADES is at the moment the only fixed-target experiment exploring the QCD phase diagram in the region of highest baryochemical potentials, thus marking the lowest point in the excitation functions of various observables. With its experiments during FAIR Phase-0, HADES will thus act as a precursor of the future experiments at SIS100.

4.2.2 Expected results

We propose an experiment which focuses on measuring a medium-heavy collision system at the maximum energy available at SIS18 in order to increase the NN center-of-mass energy in favor of an enhanced strangeness and vector meson production. With HADES we will be able to concurrently conduct the dielectron and the strangeness measurements.

The pillars of this strategy are:

- **Onset of chiral symmetry restoration in baryon rich matter [50]**: a first measurement, at SIS18 collision energies, of the e^+e^- invariant-mass spectrum in the region where the $\rho - a_1$ chiral mixing is expected to contribute. The production of the a_1 and its spectral function are expected to shape the e^+e^- spectrum above $1\,\mathrm{GeV}/c^2$ via the process $\pi^0 + a_1 \to e^+e^-$. Emphasis is therefore put on the systematic investigation of the multi-differential emission probability of dileptons in the intermediate-mass range (IMR). We will monitor the behavior of e^+e^- spectra beyond $M_{ee} \simeq 1\ \mathrm{GeV}/c^2$ in elementary and heavy-ion collisions. The results of full-scale simulations show that we will be able to measure significant e^+e^- spectra in the IMR. This is demonstrated in Fig. 4.2.

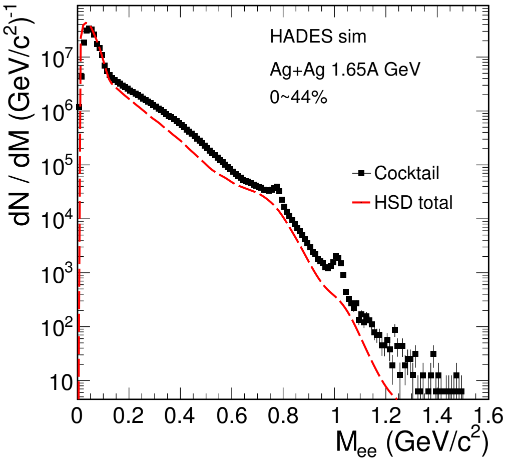

Figure 4.2: Comparison of the invariant mass spectrum of the e^+e^- cocktail including an in-medium ρ from coarse-grained transport model calculations (black squares) to the one from the HSD transport model (dashed red curve).

- **Microscopic properties of the fireball**. We will perform a precise measurement of the excess yield radiation at masses $0.2 \leq M_{ee}/(\mathrm{GeV}/c^2) \leq 0.7$. The results will be compared to the coarse-grained transport approach combined with state-of-the-art theoretical thermal electromagnetic rates [43, 44] and classical transport model calculations [42, 45, 150]. In Fig. 4.2 the cocktail including an in-medium ρ from coarse-grained transport model calculations (described in section 3.3.1) is compared to the HSD calculation for Ag+Ag at 1.65 A GeV. The error bars on the cocktail were computed as the statistical uncertainty of the signal after combinatorial background subtraction in the case that the statistics will be sufficient to produce 10^5 e^+e^- pairs from in-medium ρ. Clearly, this statistics would allow to discriminate between the two models with high significance.

- **Measurement of the fireball lifetime [33, 48, 49]**. This will be performed by extracting the excess radiation of virtual photons in the invariant mass range from 0.2 to 0.7 GeV/c^2. In order to extract the excess radiation, we first will subtract from the signal e^+e^- spectrum the cocktail of contributions from long-lived sources that will be obtained in the following way: (i) π^0 and η meson multiplicities will be measured with the help of the electromagnetic calorimeter (*cf.* s. 3.6); (ii) the ω and ϕ yields will be fixed such as to get, after subtraction, a smooth underlying continuum; the ρ contribution will not be subtracted.

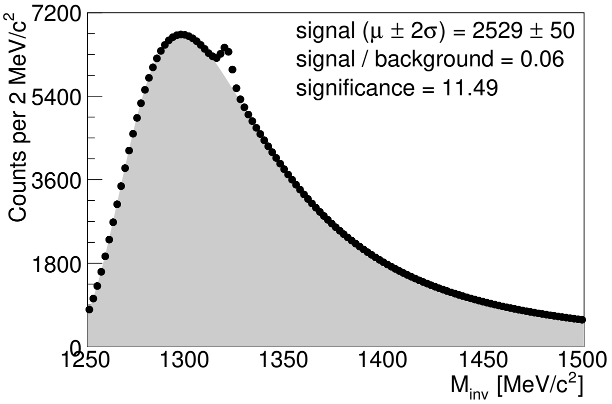

Figure 4.3: Full scale simulation of the invariant-mass distribution of Λ+π^- candidates after using Ξ^- decay topology cuts for background suppression.

- **Measurement of the fireball temperature [33, 43]**. We will extract the average fireball temperature from fits to the dielectron mass in the low- and intermediate mass range assuming a Planck-like black-body radiation.

- **Origin of the electromagnetic emission source [151, 152, 153]**. We will analyze the dilepton azimuthal anisotropy or elliptic flow (v_2) which provides a promising observable to diagnose the collective expansion dynamics.

- **Understand the ϕ meson in-medium propagation**. Will be performed by ϕ meson identification in the dielectron and K^+K^- channels. This will be of great importance to understand how strangeness behaves in baryon-rich matter.

- **Identify the mechanism responsible for the unexpectedly large Ξ^- yield**. Will be performed by a high statistic measurement of the $\Lambda\pi^-$ invariant-mass distribution. Figure 4.3 shows a high significance Ξ^- signal on top of the combinatorial background. The wide rapidity coverage of 0.3 to 1.2, in combination with the expected $2.5 \cdot 10^3$ reconstructed Ξ^-, allows for the first time a multi-differential analysis in rapidity and transverse momentum. This will be a unique measurement at this collision energy.

- **Properties (*e.g.* equation-of-state) of the dense hadronic medium [154, 155]**. Will be performed by the investigation of net-proton number, as well as net-charge fluctuations up to the 5^{th}-order cumulant at least and probably even up to 6^{th} order. This will be the first data set world-wide giving access to the cumulant ratios κ_5/κ_2 and κ_6/κ_2, expected to be particularly sensitive to features of the QCD phase diagram, with sufficient statistical precision (*cf.* s. 1.1). An important prerequisite for the interpretation of the fluctuation and flow measurements is a good understanding of the size and shape of the involved reaction volume. This point will be addressed with the help of a Glauber MC model (*cf.* s. 3.3.5).

4.2.3 Experimental setup

We will use the HADES setup with all sub-detectors, *i.e.* the upgraded RICH (*cf.* s 2.2.2), MDC, ToF, RPC, the new Electromagnetic Calorimeter (*cf.* s. 2.2.1) and a forward wall detector. A scCVD diamond based start detector will be placed in front of the HADES target.

In order to reduce the background of external photon conversion pairs, the target has to be segmented such that the decay photons can escape laterally without interacting with the target material. Already in the Ar+KCl experiment we had used a 4-fold segmentation of the KCl target. The segmentation was even more important in the high-Z target of our Au+Au run. A 1.5% nuclear interaction length silver (^{107}Ag) target (*i.e.* with thickness 0.6 mm) needs to be 15-fold segmented in order to keep the average conversion probability below 1% which is comparable with the contribution from the RICH radiator. With 40 μm thick segments (with diameter of 2.2 mm) separated by 3 mm gaps, the total length of the target will be about 45 mm, hence well within the geometric constraints of the apparatus.

The maximum beam energy of SIS18 of 2 A GeV is possible only for $Z/A = 0.5$ ions. For Au+Au a maximum energy of 1.5 A GeV is only possible with fully stripped ions available in the so-called recycling mode, a mode which requires cooling in the ESR, a further stripping of the extracted beam, re-injection into SIS18, and further acceleration up to the end energy. However, after stripping in the transfer line to the SIS18, the ions have a Gaussian-like charge-state distributions and one can select higher charge states to increase the beam energy in the SIS18 at the expense of intensity losses. For example, for Ag ions the charge state of maximum yield at injection energy is 43+, but by selecting a charge state of 46+ one can still obtain 10^8 ions/spill (spill length of 10 s) and a beam energy of 1.65 A GeV which suits the HADES demands. To ensure smooth running conditions, a good micro spill structure is of great importance. We plan to use two trigger settings in parallel, which will allow us to take minimum-bias (scaled-down) and semi-central (40% of total cross section) collisions.

4.2.4 Justification of the beam time

The demanding and comprehensive studies of all topics of high current interest listed above requires a high-statistics data set. In order to reach a break-through in our understanding of the origin of excess e^+e^- radiation, the thermal spectrum from the hadronic phase should be isolated for masses up to $1.2 - 1.5$ GeV/c^2. This would be the first measurement related to the a_1 to address chiral symmetry restoration in a high-density environment. Table 4.2 shows count-rate estimates for the π^0, η, ω and ϕ mesons and the "excess source" ($M_{ee} = 0.3 - 0.7\,\text{GeV}/c^2$ and $M_{ee} > 1\,\text{GeV}/c^2$) in the 44% most central Ag+Ag collisions. Multiplicities of π^0 and η mesons have been taken from the UrQMD model and the "excess" yield has been extracted from the coarse-grained transport model calculations for Ar+KCl by applying the measured beam and system size dependences.

M_{ee} range	<0.15 GeV/c^2	0.15-0.45 GeV/c^2	0.3-0.7 GeV/c^2	>1 GeV/c^2
Rate [84 shifts]	$2.89 \cdot 10^6$	$7.1 \cdot 10^5$	$2.1 \cdot 10^5$	107
Mesons	$\pi^0 \to \gamma e^+e^-$	$\eta \to \gamma e^+e^-$	$\omega \to e^+e^-$	$\phi \to e^+e^-$
Rate [84 shifts]	$1.5 \cdot 10^6$	$7.32 \cdot 10^5$	179	62

Table 4.2: Expected e^+e^- pair yields for 84 shifts due to π^0, η, ω and ϕ meson decays (lower row) and due to corresponding continuum radiation (upper row).

With an expected statistics of 5×10^9 triggered Ag+Ag events, a unique multi-differential measurement of the production probability of a double strange Ξ^- hyperon will become possible. It is important to emphasise that the investigations of Ξ^- production are of similar interest concerning the nuclear equation-of-state as for example the production of the triple-strange Ω^- hyperon suggested to be studied with the CBM experiment at the future SIS100 accelerator at FAIR.

The count rates of the hadrons carrying strangeness for Ag+Ag are estimated based on the number of reconstructed counts in Ar+KCl collisions at 1.76 A GeV and summarized in the Table 4.3. For the rate estimate we assumed, that the slight difference in kinetic beam energy is compensated by the stronger than linear increase with the mean number of participants observed for strange particles.

Mesons	K^+	K^-	K_s^0	Λ	ϕ	Ξ^-
Rate [84 shifts]	$7.6 \cdot 10^6$	$1.8 \cdot 10^5$	$6.36 \cdot 10^5$	$6.36 \cdot 10^5$	$2.4 \cdot 10^3$	$2.5 \cdot 10^3$

Table 4.3: Estimated count rates for various hadrons carrying strangeness recorded per 84 shifts of Ag beam on target (selecting 44% of most central Ag+Ag collisions).

To estimate the amount of beam on target, we have assumed a beam intensity of 1.5×10^6 ions per second and a 1.5% interaction target. Based on our experience from the 2012 Au+Au run and assuming that the LVL1 trigger (based on charged-hits multiplicity in ToF and RPC) selects only 44% of the total cross section, this gives a 10 kHz accepted LVL1 trigger rate and 10×10^6 events per hour on disc (this includes a dead time of 50% and a duty factor of 60%).

Furthermore, we require four additional engineering shifts: two shifts for tuning of the beam, and two shifts for running HADES without magnetic field (crucial for the precise detector alignment). Our total request therefore amounts to **88** shifts.

List of Figures

List of Tables

Bibliography

[1] J. W. Holt, N. Kaiser and W. Weise, Prog. Part. Nucl. Phys. **73** (2013) 35. 1

[2] T. Galatyuk [HADES Collaboration], PoS INPC **2016** (2017) 354. 1, 2, 71

[3] B. J. Schaefer, J. M. Pawlowski and J. Wambach, Phys. Rev. D **76** (2007) 074023. 1, 2, 71

[4] A. Andronic *et al.*, Nucl. Phys. A **837** (2010) 65. 2, 66, 71

[5] J. Stachel *et al.*, J.Phys.Conf.Ser. **509** (2014) 012019. 2, 66, 71

[6] F. Becattini *et al.*, Phys. Lett. B **764** (2017) 241. 2, 66, 71

[7] J. Cleymans, H. Oeschler, K. Redlich and S. Wheaton, Phys. Rev. C **73** (2006) 034905. 2, 8, 66, 71

[8] L. Adamczyk *et al.* [STAR Collaboration], arXiv:1701.07065 [nucl-ex]. 2, 66, 71

[9] G. Agakishiev *et al.* [HADES Collaboration], Eur. Phys. J. A **52** (2016) no.6, 178. 2, 8, 66, 71

[10] X. Lopez *et al.* [FOPI Collaboration], Phys. Rev. C **76** (2007) 052203. 2, 66, 71

[11] O. Kaczmarek *et al.*, Phys. Rev. D **83** (2011) 014504. 2, 66, 71

[12] S. Borsanyi *et al.* [Wuppertal-Budapest Collaboration], JHEP **1009** (2010) 073. 2, 66, 71

[13] H. J. Specht *et al.* [NA60 Collaboration], AIP Conf. Proc. **1322** (2010) 1. 2, 3, 66, 71

[14] R. Rapp and J. Wambach, Adv. Nucl. Phys. **25**, 1 (2000). 2, 3, 66

[15] G. Agakishiev *et al.* [HADES Collaboration], Phys. Rev. C **84** (2011) 014902. 3, 4, 40, 66

[16] G. Agakishiev *et al.* [HADES Collaboration], Phys. Lett. B **690** (2010) 118. 3, 4, 10, 11, 66

[17] J. Adamczewski-Musch *et al.* [HADES Collaboration], arXiv:1703.08575 [nucl-ex]. 3, 10, 11

[18] J. Adamczewski-Musch *et al.* [HADES Collaboration], Phys. Rev. C **95** (2017) no.6, 065205. 3, 10, 32

[19] G. Agakishiev *et al.* [HADES Collaboration], Eur. Phys. J. A **50** (2014) 82. 3, 4, 11, 12, 45, 46, 66, 72

[20] G. Agakishiev *et al.* [HADES Collaboration], Phys. Lett. B **715** (2012) 304. 3, 4, 38, 62, 66

[21] G. Agakishiev *et al.* [HADES Collaboration], Phys. Lett. B **731** (2014) 265. 3, 50

[22] G. Agakishiev *et al.* [HADES Collaboration], Phys. Rev. C **87** (2013) 025201. 3, 36, 37

[23] G. Agakishiev *et al.* [HADES Collaboration], Phys. Lett. B **742** (2015) 242. 3

[24] G. Agakishiev *et al.* [HADES Collaboration], Phys. Rev. C **90** (2014) 054906. 3

[25] G. Agakishiev *et al.* [HADES Collaboration], Phys. Rev. C **80** (2009) 025209. 3

[26] J. Adamczewski-Musch *et al.* [HADES Collaboration], arXiv:1703.08418 [nucl-ex]. 3, 6, 71

[27] G. Agakishiev *et al.* [HADES Collaboration], Phys. Rev. Lett. **103** (2009) 132301. 3, 6, 42, 66

[28] G. Agakishiev *et al.* [HADES Collaboration], Phys. Rev. Lett. **114** 21 (2015) 212301. 3, 6, 42, 66

[29] D. Adamova *et al.*, Phys. Lett. B **666** (2008) 425. 3

[30] A. Adare *et al.* [PHENIX Collaboration], Phys. Rev. C **93** (2016) no.1, 014904. 3

[31] L. Adamczyk *et al.* [STAR Collaboration], Phys. Rev. C **92** (2015) no.2, 024912. 3

[32] L. Adamczyk *et al.* [STAR Collaboration], Phys. Lett. B **750** (2015) 64. 3

[33] R. Rapp and H. van Hees, Phys. Lett. B **753** (2016) 586. 3, 5, 67, 68

[34] M. Herrmann, B. L. Friman and W. Norenberg, Nucl. Phys. A **560** (1993) 411. 3, 66

[35] G. Chanfray and P. Schuck, Nucl. Phys. A **555** (1993) 329. 3, 66

[36] R. Rapp, G. Chanfray and J. Wambach, Phys. Rev. Lett. **76** (1996) 368. 3, 66

[37] W. Peters, M. Post, H. Lenske, S. Leupold and U. Mosel, Nucl. Phys. A **632** (1998) 109. 3, 66

[38] M. Post, S. Leupold and U. Mosel, Nucl. Phys. A **741** (2004) 81. 4, 66

[39] R. Rapp, AIP Conf. Proc. **1322** (2010) 55. 4

[40] G. Agakishiev *et al.* [HADES Collaboration], Eur. Phys. J. A **48** (2012) 64. 4, 11, 12, 66, 72

[41] R. Arnaldi *et al.* [NA60 Collaboration], Phys. Rev. Lett. **96** (2006) 162302. 4

[42] J. Weil, H. van Hees and U. Mosel, Eur. Phys. J. A **48** (2012) 111. Erratum: [Eur. Phys. J. A **48** (2012) 150]. 5, 67, 71

[43] T. Galatyuk, P. M. Hohler, R. Rapp, F. Seck and J. Stroth, Eur. Phys. J. A **52**, no. 5 (2016) 131. 5, 40, 66, 67, 68, 71

[44] S. Endres, H. van Hees, J. Weil and M. Bleicher, Phys. Rev. C **92**, no. 1 (2015) 014911. 5, 67, 71

[45] E. L. Bratkovskaya *et al.*, Phys. Rev. C **87** (2013) 064907. 5, 41, 67, 71

[46] P. Tlusty *et al.* [HADES Collaboration], arXiv:0906.2309 [nucl-ex] 5

[47] R. Averbeck *et al.* [TAPS Collaboration], Z. Phys. A **359** (1997) 65. 5

[48] U. W. Heinz and K. S. Lee, Phys. Lett. B **259** (1991) 162. 5, 67

[49] H. W. Barz, B. L. Friman, J. Knoll and H. Schulz, Phys. Lett. B **254** (1991) 315. 5, 67

[50] P. M. Hohler and R. Rapp, Phys. Lett. B **731** (2014) 103. 5, 67

[51] T. Hatsuda, Y. Koike and S. H. Lee, Nucl. Phys. B **394** (1993) 221. 5

[52] J. I. Kapusta and E. V. Shuryak, Phys. Rev. D **49** (1994) 4694. 5

[53] R. Rapp and J. Wambach, Eur. Phys. J. A **6** (1999) 415. 5

[54] P. M. Hohler and R. Rapp, Annals Phys. **368** (2016) 70. 5

[55] G. Agakishiev *et al.* [HADES Collaboration], Eur. Phys. J. A **47** (2011) 21. 6

[56] J. Steinheimer and M. Bleicher, J. Phys. G **43** (2016) no.1, 015104. 7

[57] P. Braun-Munzinger, K. Redlich and J. Stachel, arXiv:nucl-th/0304013 (2003). 8

[58] A. N. Tawfik, Int. J. Mod. Phys. A **29** 17 (2014) 1430021. 8

[59] M. Floris, Nucl. Phys. A **931** (2014) 103. 8

[60] S. Wheaton, J. Cleymans, Comput. Phys. Commun. **180** (2009) 84. 8

[61] X. Luo [STAR Collaboration], PoS CPOD **2014** (2015) 019 8

[62] A. Bzdak and V. Koch, Phys. Rev. C **86** (2012) 044904. 8

[63] A. Bzdak and V. Koch, Phys. Rev. C **91** (2015) 027901. 8

[64] A. Bzdak, R. Holzmann and V. Koch, Phys. Rev. C **94** (2016) no.6, 064907. 8

[65] V. Skokov, B. Friman, and K. Redlich, Phys. Rev. C **88** (2013) 034911. 8

[66] B. Ling and M.A. Stephanov, Phys. Rev. C **93** (2016) 034915. 8

[67] P. Braun-Munzinger, A. Rustamov, and J. Stachel, Nucl. Phys. A **960** (2017) 114. 8

[68] B. Kardan (for the HADES Collaboration), to appear in Nucl. Phys. A 9, 72

[69] A. M. Poskanzer and S. A. Voloshin, Phys. Rev. C **58** (1998) 1671. 9

[70] J. Y. Ollitrault, Nucl. Phys. A **638** (1998) 195. 9

[71] R. Shyam and U. Mosel, Phys. Rev. C **79** (2009) 035203. 10, 11, 72

[72] M. Bashkanov and H. Clement, Eur. Phys. J. A **50** (2014) 107. 10, 11, 72

[73] F. Iachello and Q. Wan, Phys. Rev. C **69** (2004) 055204. 10, 11, 72

[74] I. Fröhlich *et al.*, Eur. Phys. J. A **45** (2010) 401. 10

[75] R. Bijker and F. Iachello, Phys. Rev. C **69** (2004) 068201. 10

[76] G. Ramalho, M. T. Pena, J. Weil, H. van Hees and U. Mosel, Phys. Rev. D **93**, no. 3 (2016) 033004. 10, 11, 12, 72

[77] G. Agakishiev *et al.* [HADES Collaboration], Phys. Rev. C **85** (2012) 054005. 11

[78] J. Weil, U. Mosel and V. Metag, Phys. Lett. B **723** (2013) 120. 11

[79] D. Lonardoni, A. Lovato, S. Gandolfi and F. Pederiva, Phys. Rev. Lett. **114** (2015) no.9, 092301. 14

[80] J. Haidenbauer *et al.*, Nucl. Phys. A **915** (2013) 24. 14

[81] J. Adamczewski-Musch *et al.* [HADES Collaboration], Phys. Rev. C **94**, no. 2 (2016) 025201. 14

[82] T. Ablyazimov *et al.* [CBM Collaboration], Eur. Phys. J. A **53**, no. 3 (2017) 60. 16, 73

[83] J-PARC-HI proposal http://silver.j-parc.jp/sako/white-paper-v1.21.pdf 16, 73

[84] A. Dainese *et al.*, Frascati Phys. Ser. **62** (2016). 16, 73

[85] A. Rost *et al.* [TRB and HADES and CBM Collaborations], JINST **12**, no. 02 (2017) C02047. 20

[86] J. Pietraszko *et al.* [HADES Collaboration], Nucl. Instrum. Meth. A **763** (2014) 1. 25

[87] M. Idzik, G. Korcyl, D. Przyborowski, P. Salabura, J. Smyrski and P. Strzempek, doi:10.1109/RTC.2016.7543165 26

[88] C. Ugur, W. Koening, J. Michel, M. Palka and M. Traxler, JINST **8** (2013) C01035. 26

[89] E. Speranza, M. Zetenyi and B. Friman, Phys. Lett. B **764** (2017) 282. 33, 34, 74

[90] W. Przygoda *et al.* [HADES Collaboration], EPJ Web of Conferences 130, 01021 (2016) https://doi.org/10.1051/epjconf/201613001021. 33

[91] F. Scozzi *et al.* [HADES Collaboration], EPJ Web of Conferences 137, 05023 (2017) https://doi.org/10.1051/epjconf/201713705023. 33

[92] M. I. Krivoruchenko, B. V. Martemyanov, A. Faessler and C. Fuchs, Annals Phys. **296** (2002) 299. 33, 45

[93] I. G. Aznauryan and V. D. Burkert, Prog. Part. Nucl. Phys. **67** (2012) 1. 33

[94] A. Thiel *et al.* [CBELSA/TAPS Collaboration], Phys. Rev. Lett. **114** (2015) no.9, 091803. 35

[95] D. Ronchen *et al.*, Eur. Phys. J. A **49** (2013) 44. 36

[96] N. Kaiser, P. B. Siegel and W. Weise, Nucl. Phys. A **594** (1995) 325. 36

[97] E. Oset and A. Ramos, Nucl. Phys. A **635** (1998) 99. 36

[98] B. Borasoy, U.-G. Meissner and R. Nissler, Phys. Rev. C **74** (2006) 055201. 36

[99] D. Cabrera, L. Tolos, J. Aichelin and E. Bratkovskaya, Phys. Rev. C **90** (2014) no.5, 055207. 36

[100] D. W. Thomas, A. Engler, H. E. Fisk and R. W. Kraemer, Nucl. Phys. B **56** (1973) 15. 36

[101] R. J. Hemingway, Nucl. Phys. B **253** (1985) 742. 36

[102] I. Zychor *et al.*, Phys. Lett. B **660** (2008) 167. 36

[103] K. Moriya *et al.* [CLAS Collaboration], Phys. Rev. C **87** (2013) no.3, 035206. 36

[104] T. Yamazaki and Y. Akaishi, Phys. Rev. C **76** (2007) 045201. 38

[105] A. Dote, T. Hyodo and W. Weise, Phys. Rev. C **79** (2009) 014003. 38

[106] S. Wycech and A. M. Green, Phys. Rev. C **79** (2009) 014001. 38

[107] N. Barnea, A. Gal and E. Z. Liverts, Phys. Lett. B **712** (2012) 132. 38

[108] N. V. Shevchenko, A. Gal and J. Mares, Phys. Rev. Lett. **98** (2007) 082301. 38

[109] Y. Ikeda and T. Sato, Phys. Rev. C **79** (2009) 035201. 38

[110] E. Oset, D. Jido, T. Sekihara, A. Martinez Torres, K. P. Khemchandani, M. Bayar and J. Yamagata-Sekihara, Nucl. Phys. A **881** (2012) 127. 38

[111] T. Nagae, Nucl. Phys. A **954** (2016) 94. 38

[112] T. Weidmann, E. L. Bratkovskaya, W. Cassing and U. Mosel, Phys. Rev. C **59** (1999) 919 38

[113] M. Effenberger, E. L. Bratkovskaya, W. Cassing and U. Mosel, Phys. Rev. C **60** (1999) 027601. 38, 62

[114] M. Lorenz *et al.* [HADES Collaboration], as presented on the CPOD conference 2016. 44

[115] B. Friman, F. Karsch, K. Redlich, and V. Skokov, Eur. Phys. J. C **71** (2011) 1694. 44

[116] E. Kaxiras, E. J. Moniz and M. Soyeur, Phys. Rev. D **32** (1985) 695. 47, 48

[117] S. Dobbs, A. Tomaradze, T. Xiao and K. K. Seth, AIP Conf. Proc. **1735** (2016) 080003. 48

[118] R. A. Williams, C. R. Ji and S. R. Cotanch, Phys. Rev. C **48** (1993) 1318. 48

[119] T. Kunz phd and "First measurement of $\Sigma^0$0 production in proton induced reactions on a nuclear target at E = 3.5 GeV" to be published 48

[120] J. Adamczewski-Musch *et al.* [HADES Collaboration], Phys. Rev. C **95** (2017) no.1, 015207. 48

[121] R. Shneor *et al.*, Phys. Rev. Lett. **99** (2007) 072501. 51

[122] R. Subedi *et al.*, Science **320** (2008) 1476. 51

[123] A. Tang *et al.*, Phys. Rev. Lett. **90** (2003) 042301. 51, 52, 53, 75

[124] E. Piasetzky, M. Sargsian, L. Frankfurt, M. I. Strikman and J. W. Watson, Phys. Rev. Lett. **97** (2006) 162504. 51, 52, 53, 75

[125] O. Hen *et al.* (CLAS Collaboration), Science **346** (2014) 614. 51

[126] I. Korover, N. Muangma, O. Hen *et al.*, Phys.Rev.Lett. **113** (2014) 022501. 51, 53, 75

[127] L. L. Frankfurt and M. I. Strikman, Phys. Rep. **76** (1981) 215. 51

[128] L. L. Frankfurt and M. I. Strikman, Phys. Rep. **160** (1988) 235. 51

[129] J. Arrington, D. W. Higinbotham, G. Rosner, and M. Sargsian, Prog. Part. Nucl. Phys. **67** (2012) 898. 51

[130] O. Hen, G. A. Miller, E. Piasetzky and L. B. Weinstein, arXiv:1611.09748 [nucl-ex], submitted to Reviews of Modern Physics (2016). 51

[131] O. Hen, D. W. Higinbotham, G. Miller, E. Piasetzky, and L. B. Weinstein, Int. J. Mod. Phys. E **22**, 133017 (2013).

[132] C. Ciofi degli Atti, Phys. Rep. **590** (2015) 1–85. 51

[133] C. Ciofi degli Atti, Phys. Rep. **590** (2015) 1–85.

[134] R. Schiavilla, R. B. Wiringa, S. C. Pieper, and J. Carlson, Phys. Rev. Lett. **98** (2007) 132501. 51

[135] R. B. Wiringa, R. Schiavilla, S. C. Pieper and J. Carlson, Phys. Rev. C **78** (2008) 021001. 51

[136] R. B. Wiringa, R. Schiavilla, S. Steven, C. Pieper, and J. Carlson, Phys. Rev. C **89** (2014) 024305. 51

[137] M. Alvioli, C. Ciofi degli Atti, and H. Morita, Phys. Rev. Lett. **100** (2008) 162503. 51, 53, 75

[138] M. M. Sargsian *et al.*, Phys. Rep. C **71** (2005) 044615. 51

51

[139] The R^3B collaboration, Technical Report for the Design, Construction and Commissioning of NeuLAND: The High-Resolution Neutron Time-of-Flight Spectrometer for R^3B, Available at *http : //www.fair − center.de/fileadmin/fair/experiments/NUSTAR/Pdf/TDRs/NeuLAND − TDR − Web.pdf* 52

[140] The full proposal for the HADES/GSI SRC measurements *https : //www.hen − lab.com/srchades*. 52, 54

[141] R. Weiss, R. Cruz-Torres, N. Barnea, E. Piasetzky and O. Hen, arXiv:1612.00923 [nucl-th]. 53, 75

[142] M. F. M. Lutz, B. Friman and M. Soyeur, Nucl. Phys. A **713** (2003) 97. 61

[143] A. I. Titov and B. Kampfer, Eur. Phys. J. A **12** (2001) 217. 61

[144] K. H. Hicks and H. Sako, J-PARC Proposal E45, Japan, 2012; www.phy.ohiou.edu/~hicks/NSF/2013/JPARC-P45.pdf. 62

[145] W. J. Briscoe, M. Döring, H. Haberzettl, D. M. Manley, M. Naruki, I. I. Strakovsky and E. S. Swanson, Eur. Phys. J. A **51** (2015) no.10, 129. 62

[146] J. Diaz *et al.*, Nucl. Instrum. Meth. A **478** (2002) 511. 63

[147] F. Scozzi [HADES Collaboration], EPJ Web Conf. **137** (2017) 05023. 60

[148] S. A. Bass *et al.*, Prog. Part. Nucl. Phys. **41** (1998) 255. 66

[149] C. Fuchs, Prog. Part. Nucl. Phys. **56** (2006) 1. 66

[150] J. Weil, J. Staudenmaier and H. Petersen, J. Phys. Conf. Ser. **742** (2016) no.1, 012034. 67

[151] R. Chatterjee, D. K. Srivastava, U. W. Heinz and C. Gale, *Phys. Rev. C 75* (2007) 054909. 68

[152] J. Deng, Q. Wang, N. Xu and P. Zhuang, *Phys. Lett. B 701* (2011) 581. 68

[153] P. Mohanty, V. Roy, S. Ghosh, S. K. Das, B. Mohanty, S. Sarkar, J. e. Alam and A. K. Chaudhuri, *Phys. Rev. C 85* (2012) 031903. 68

[154] K. Morita, B. Friman and K. Redlich, Phys. Lett. B **741** (2015) 178. 68

[155] G. A. Almasi, B. Friman and K. Redlich, arXiv:1703.05947 [hep-ph]. 68

Appendix A

The HADES Collaboration

J. Adamczewski-Musch[4], O. Arnold[10,9], C. Behnke[8], A. Belounnas[16], A. Belyaev[7], J. Biernat[3], A. Blanco[2], C. Blume[8], M. Böhmer[10], P. Bordalo[2], G. Cantarella[8], L. Chlad[17], I. Ciepal[b], C. Deveaux[11], D. Dittert[5], J. Dreyer[6], L. Fabbietti[10,9], O. Fateev[7], P. Filip[1], P. Fonte[2,a], C. Franco[2], J. Friese[10], I. Fröhlich[8], T. Galatyuk[5,4], J. A. Garzón[18], A. Gillitzer[12], M. Golubeva[13], R. Greifenhagen[6], F. Guber[13], M. Gumberidze[5,c], S. Harabasz[5,3], T. Heinz[4], T. Hennino[16], M. Himmelreich[8], S. Hlavac[1], C. Höhne[11], R. Holzmann[4], A. Ierusalimov[7], V. Ivanov[7], A. Ivashkin[13], B. Kämpfer[6,d], M. Kajetanowicz[3], K-H. Kampert[19], T. Karavicheva[13], B. Kardan[8], V. Khomyakov[14], I. Koenig[4], W. Koenig[4], G. Korcyl[3], G. Kornakov[5], F. Kornas[5], R. Kotte[6], A. Kugler[17], T. Kunz[10], A. Kurepin[13], P. Kurilkin[7], V Kushpil[17], V. Ladygin[7], R. Lalik[10,9], A. Lebedev[14], S. Linev[4], M. Liu[11], L. Lopes[2], M. Lorenz[8,h], G. Lykasov[7], T. Mahmoud[11], A. Malakhov[7], J. Markert[4], S. Maurus[10], V. Metag[11], J. Michel[8], D.M. Mihaylov[10,9], V. Mikhaylov[17], S. Morozov[13,e], C. Müntz[8], L. Naumann[6], K. Nowakowski[3], Y. Parpottas[15,f], V. Patel[19], C. Pauly[19], V. Pechenov[4], O. Pechenova[8], A. Pereira[2], V. Petousis[15], O. Petukhov[13,e], D. Pfeifer[19], J. Pietraszko[4], W. Przygoda[3], S. Ramos[2], B. Ramstein[16], A. Reshetin[13], L. Ritman[12], P. Rodriguez-Ramos[17], A. Rost[5], A. Sadovsky[13], P. Salabura[3], T. Scheib[8], H. Schuldes[8], E. Schwab[4], F. Scozzi[5,16], F. Seck[5], P. Sellheim[8], I. Selyuzhenkov[e,4], L. Silva[2], J. Smyrski[3], M. Sobiella[6], S. Spataro[g], H. Ströbele[8], J. Stroth[8,4], P. Strzempek[3], O. Svoboda[17], M. Szala[8], A. Tarnenko[e], P. Tlusty[17], M. Traxler[4], A. Troyan[7], H. Tsertos[15], V. Wagner[17], C. Wendisch[4], M.G. Wiebusch[8], P. Wintz[12], J. Wirth[10,9], A. Zhilin[14], A. Zinchenko[7], P. Zumbruch[4], M. Zuschke[8]

HADES collaboration

[1] *Institute of Physics, Slovak Academy of Sciences, 84228 Bratislava, Slovakia*
[2] *LIP-Laboratório de Instrumentação e Física Experimental de Partículas , 3004-516 Coimbra, Portugal*
[3] *Smoluchowski Institute of Physics, Jagiellonian University of Cracow, 30-059 Kraków, Poland*
[4] *GSI Helmholtzzentrum für Schwerionenforschung GmbH, 64291 Darmstadt, Germany*
[5] *Technische Universität Darmstadt, 64289 Darmstadt, Germany*
[6] *Institut für Strahlenphysik, Helmholtz-Zentrum Dresden-Rossendorf, 01314 Dresden, Germany*
[7] *Joint Institute of Nuclear Research, 141980 Dubna, Russia*
[8] *Institut für Kernphysik, Goethe-Universität, 60438 Frankfurt, Germany*
[9] *Excellence Cluster 'Origin and Structure of the Universe' , 85748 Garching, Germany*
[10] *Physik Department E62, Technische Universität München, 85748 Garching, Germany*
[11] *II.Physikalisches Institut, Justus Liebig Universität Giessen, 35392 Giessen, Germany*
[12] *Forschungszentrum Juelich, 52428 Juelich, Germany*
[13] *Institute for Nuclear Research, Russian Academy of Science, 117312 Moscow, Russia*
[14] *Institute of Theoretical and Experimental Physics, 117218 Moscow, Russia*
[15] *Department of Physics, University of Cyprus, 1678 Nicosia, Cyprus*
[16] *Institut de Physique Nucléaire, CNRS-IN2P3, Univ. Paris-Sud, Université Paris-Saclay, F-91406 Orsay Cedex, France*
[17] *Nuclear Physics Institute, The Czech Academy of Sciences, 25068 Rez, Czech Republic*
[18] *LabCAF. F. Física, Univ. de Santiago de Compostela, 15706 Santiago de Compostela, Spain*
[19] *Bergische Universität Wuppertal, 42119 Wuppertal, Germany*

[a] *also at ISEC Coimbra, Coimbra, Portugal*
[b] *also at Instytut Fizyki Jądrowej, 30059 Kraków, Poland*
[c] *also at ExtreMe Matter Institute EMMI, 64291 Darmstadt, Germany*
[d] *also at Technische Universität Dresden, 01062 Dresden, Germany*
[e] *also at Moscow Engineering Physics Institute (State University), 115409 Moscow, Russia*
[f] *also at Frederick University, 1036 Nicosia, Cyprus*
[g] *also at Dipartimento di Fisica and INFN, Università di Torino, 10125 Torino, Italy*
[h] *also at Utrecht University, 3584 CC Utrecht, The Netherlands*